

**DEVICE-FREE LOCALIZATION WITH RECEIVED
SIGNAL STRENGTH MEASUREMENTS IN
WIRELESS NETWORKS**

by

Anthony Joseph Wilson

A dissertation submitted to the faculty of
The University of Utah
in partial fulfillment of the requirements for the degree of

Doctor of Philosophy

Department of Electrical and Computer Engineering

The University of Utah

August 2010

Copyright © Anthony Joseph Wilson 2010

All Rights Reserved

The University of Utah Graduate School

STATEMENT OF DISSERTATION APPROVAL

The dissertation of Anthony Joseph Wilson
has been approved by the following supervisory committee members:

<u>Neal Patwari</u>	, Chair	<u>07/12/10</u> Date Approved
<u>Behrouz Farhang-Boroujeny</u>	, Member	<u>07/12/10</u> Date Approved
<u>Cynthia Furse</u>	, Member	<u>07/12/10</u> Date Approved
<u>Sarang Joshi</u>	, Member	<u>07/12/10</u> Date Approved
<u>Osama Haddadin</u>	, Member	<u>07/12/10</u> Date Approved

and by Gianluca Lazzi, Chair of
the Department of Electical and Computer Engineering

and by Charles A. Wight, Dean of The Graduate School.

ABSTRACT

Device-free localization (DFL) is the practice of locating people or objects when no tag or device is attached to the entity being tracked. DFL technologies are useful in applications where the targets being tracked and detected are not expected to cooperate with the system. This may be the case because the entities being tracked are evading surveillance, because they are unable, or because they do not want to be inconvenienced. This dissertation discusses some novel and cost-effective methods for locating people with received signal strength (RSS) measurements in wireless networks.

The first contribution of this work presents a linear model for using received signal strength (RSS) measurements to obtain images of moving objects, a process called radio tomographic imaging (RTI). Noise models are investigated based on real measurements of a deployed RTI system. Mean-squared error (MSE) bounds on image accuracy are derived, which are used to calculate the accuracy of an RTI system for a given node geometry. The ill-posedness of RTI is discussed, and Tikhonov regularization is used to derive an image estimator.

We then present variance-based RTI, which takes advantage of the motion-induced variance of received signal strength measurements. Using a multipath channel model, we show that the signal strength on a wireless link is largely dependent on the power contained in multipath components that travel through space containing moving objects. A statistical model relating variance to spatial locations of movement is presented and used as a framework for the estimation of a motion image.

The final contribution of this dissertation introduces measurement-based statistical models that can be used to estimate the locations of people using signal strength measurements in wireless networks. We demonstrate, using extensive experimental data, that changes in signal strength measurements due to human motion can be modeled by the skew-Laplace distribution. The parameters of

the distribution are dependent on the position of person and on the amount of fading that a particular link experiences. Using the skew-Laplace likelihood model, we apply a particle filter to experimentally estimate the location of moving and stationary people through walls.

CONTENTS

ABSTRACT	iii
LIST OF FIGURES	viii
LIST OF TABLES	xi
ACKNOWLEDGMENTS	xii
CHAPTERS	
1. INTRODUCTION	1
1.1 Copyright Notice	1
1.2 Overview of Device-Free Localizaiton	1
1.3 Sensor technologies	2
1.3.1 Optical Cameras	3
1.3.2 Thermal Cameras	3
1.3.3 Infrared	4
1.3.4 Acoustic, Vibration, and Ultrasound	4
1.3.5 Radio Frequency	5
1.4 Radio Frequency DFL Technologies	6
1.4.1 Ultra-Wideband (UWB)	6
1.4.2 Narrowband	7
1.4.3 Received Signal Strength (RSS)	8
1.5 Contribution of this Dissertation	9
2. RADIO TOMOGRAPHIC IMAGING WITH WIRELESS NETWORKS	14
2.1 Abstract	14
2.2 Introduction	14
2.2.1 Applications	15
2.2.2 Related Work	16
2.2.3 Overview	18
2.3 Model	18
2.3.1 Linear Formulation	18
2.3.2 Weight Model	20
2.3.3 Noise	21
2.4 Error Bound	23
2.4.1 Derivation	23
2.4.2 Spatial Covariance Model	25
2.4.3 Example Error Bounds	25
2.4.4 Effect of Node Density	25
2.5 Image Reconstruction	26

2.5.1	Ill-posed Inverse Problem	26
2.5.2	Tikhonov Regularization	28
2.6	Experimental Results	29
2.6.1	Physical Description of Experiment	29
2.6.2	Effect of Human Obstruction	30
2.6.3	Cylindrical Human Model	31
2.6.4	Example Images	32
2.6.5	Effect of Parameters on Image Accuracy	32
2.7	Conclusion	33
3.	REGULARIZATION METHODS FOR RADIO TOMOGRAPHIC IMAGING	48
3.1	Abstract	48
3.2	Introduction	48
3.3	Related Work	49
3.4	Linear Formulation	51
3.5	Regularization	53
3.5.1	Tikhonov	55
3.5.2	Truncated Singular Value Decomposition (TSVD)	55
3.5.3	Total Variation	56
3.6	Results	57
3.6.1	Tikhonov	58
3.6.2	Truncated Singular Value Decomposition (TSVD)	59
3.6.3	Total Variation	59
3.7	Conclusion	60
4.	THROUGH-WALL MOTION TRACKING USING VARIANCE-BASED RADIO TOMOGRAPHY NETWORKS	70
4.1	Abstract	70
4.2	Introduction	70
4.3	Related Research	72
4.4	Variance-Based Radio Tomographic Imaging	74
4.4.1	Measurement Model	74
4.4.2	Variance and Total Affected Power	75
4.4.3	Total Affected Power and Motion	77
4.4.4	Elliptical Weight Model	78
4.4.5	Process Sampling, Buffering, and Variance Estimation	79
4.4.6	Regularization and Image Estimation	80
4.5	Kalman Filter Tracking	81
4.6	Experiment	82
4.6.1	Description and Layout	82
4.6.2	Image Results	83
4.6.3	Path Tracking	84
4.6.4	Spot Movement	85
4.6.5	Effect of Imaging Parameters on Tracking Accuracy	85
4.7	Future Research	86
4.8	Conclusion	87

5. A STATISTICAL INVERSION METHOD AND MODEL FOR DEVICE-FREE LOCALIZATION IN RF SENSOR NETWORKS	102
5.1 Abstract	102
5.2 Introduction	102
5.3 Statistical Modeling	104
5.3.1 Overview	104
5.3.2 Measurement Collection	105
5.3.3 Fading Information	107
5.3.4 Quantification of Fade Level	108
5.3.5 Measurement and Modeling Results	108
5.4 Particle Filtering	110
5.4.1 Overview	110
5.4.2 Particle Filter Algorithm	111
5.5 Experimental Results	112
5.5.1 Description and Layout	112
5.5.2 Stationary Targets	112
5.5.3 Moving Targets	113
5.6 Related Work	114
5.7 Conclusion	116
6. CONCLUSION	134
6.1 Key Findings	134
6.2 Comparison of Tracking Methods	137
6.3 Future Work	138
REFERENCES	142

LIST OF FIGURES

2.1	An illustration of an RTI network. Each node broadcasts to the others, creating many projections that can be used to reconstruct an image of objects inside the network area.	35
2.2	An illustration of a single link in an RTI network that travels in a direct LOS path. The signal is shadowed by objects as it crosses the area of the network in a particular path. The darkened voxels represent the image areas that have a nonzero weighting for this particular link. . . .	36
2.3	Temporal fading on link (3, 20) during nonobstructing motion, showing (a) time plot and (b) histogram.	37
2.4	Quantile-quantile plots comparing measured RSS data with Gaussian and Mixture distributions.	38
2.5	MSE bound surface plots for a square network.	39
2.6	MSE bound surface plots for a front-back network.	40
2.7	MSE bound surface plots for random node locations.	41
2.8	The lower bound on average MSE vs. node density for three RTI network geometries.	42
2.9	The network geometry and links that correspond to Fig. 2.10 are illustrated in (a). (b) is a photo of the deployed network with an experimenter standing at location (3,9).	43
2.10	A comparison of the effect of human obstruction on three links. In the unobstructed case, the network is vacant from human experimenters. In the obstructed case, a human stands at coordinate (9,9).	44
2.11	RTI results for a single human standing at coordinate (9,9). The person is modeled as a uniformly attenuating cylinder of radius $R_H = 1.3$ feet.	45
2.12	RTI results for a two humans standing at coordinates (3,15) and (18,15). Each person is modeled as a uniformly attenuating cylinder of radius $R_H = 1.3$ feet.	46
2.13	Error vs. parameter curves. In the first plot, the weighting ellipse width parameter is held constant at $\lambda = .1$ while the regularization parameter α is varied. In the second, $\alpha = 4.5$ and the width of the weighting ellipse is varied.	47
3.1	An illustration of an RTI network. Each node broadcasts to the others, creating many projections that can be used to reconstruct an image of objects inside the network area.	61

3.2	An illustration of a single link in an RTI network that travels in a direct LOS path. The signal is shadowed by objects as it crosses the area of the network in a particular path. The darkened voxels represent the image areas that have a non-zero weighting for this particular link. . .	62
3.3	The RTI geometry and human locations for the images found in Section 3.6. Twenty-eight nodes are placed in a square perimeter, with two humans standing inside the area at coordinates (3,1) and (1,3). . .	63
3.4	RTI results using H1 regularization with parameter $\alpha = 2$ using forward difference matrices.	64
3.5	RTI results using H1 regularization with parameter $\alpha = 2$ using forward difference matrices.	65
3.6	RTI results using truncated singular value regularization. Here, any singular value below the threshold $\tau = 5.6$ is truncated.	66
3.7	RTI results using truncated singular value regularization. Here, any singular value below the threshold $\tau = 5.6$ is truncated.	67
3.8	RTI results using total variation regularization with parameter $\alpha = .35$ and $\beta = .08$	68
3.9	RTI results using total variation regularization with parameter $\alpha = .35$ and $\beta = .08$	69
4.1	The variance of RSS vs. normalized TAP, $T_{AP}(\mathbf{x})/\bar{V}^2$, for $\sigma_v^2/\bar{V}^2 = 0.01$.	89
4.2	The layout of a 34-node variance-based RTI through-wall tracking experiment.	90
4.3	RSS measurements for two links in a through-wall wireless network. Comparison of these signals illustrates the advantage of using variance over mean for through-wall imaging of human motion.	91
4.4	Shadowing-based RTI results for through-wall imaging. The experimenter is moving at coordinate (14.6,21.3).	92
4.5	Variance-based RTI results for through-wall imaging. The experimenter is moving at coordinate (14.6,21.3).	93
4.6	The location of human movement moving along a known rectangular path is estimated using constant $v_n^2 = 5$. Here, the mobility v_m is set empirically to track objects moving at a few feet per second.	94
4.7	The location of human movement moving along a known rectangular path is estimated using constant $v_n^2 = 5$. Here, the mobility v_m is set empirically to track objects moving at a few feet per second.	95
4.8	The location of human movement moving along a known rectangular path is estimated using constant $v_n^2 = 5$. Here, the mobility v_m is set too low, causing the tracking filter to lag excessively.	96
4.9	The location of human movement moving along a known rectangular path is estimated using constant $v_n^2 = 5$. Here, the mobility v_m is set too low, causing the tracking filter to lag excessively.	97

4.10	The ten-second average locations of human movement over 20 known positions is estimated using VRTI and Kalman filter tracking with parameters $v_m^2 = .01$ and $v_n^2 = 5$. The average error for this experiment $\zeta = 1.46$ feet.	98
4.11	Effect of ellipse width λ on average tracking error ϵ . Other parameters are equal to those shown in Table 4.1.	99
4.12	Effect of regularization parameter α on average tracking error ϵ . Other parameters are equal to those shown in Table 4.1.	100
4.13	Effect of buffer size N_B on average tracking error ϵ . Other parameters are equal to those shown in Table 4.1.	101
5.1	A flowchart describing the statistical inversion process for device-free localization in wireless networks.	119
5.2	An illustration showing the role of likelihood and posterior distributions for statistical inversion.	120
5.3	The layout of a 34-node through-wall wireless network deployment. . .	121
5.4	An example of how the RSS statistics for two links of equivalent distance and geometry are drastically affected by the fade level. Here, a human crosses through the LOS at $t = 52$. Link 1 is in an "antifade" while Link 2 is in a deep fade.	122
5.5	RSS measurement distributions for on/off LOS target positions. The histograms are for links experiencing deep fades less than -15dBm. . . .	123
5.6	RSS measurement distributions for on/off LOS target positions. The histograms are for links experiencing antifades greater than 10dBm. . .	124
5.7	Quantile-Quantile plots for deep fades.	125
5.8	Quantile-Quantile plots for antifades.	126
5.9	Mode parameter fitting over a range of fade levels in dBm.	127
5.10	Decay parameters when the target is located on the LOS path.	128
5.11	Decay parameters when the target is off the LOS path.	129
5.12	The convergence of the particle filter after 5 iterations The filter has determined that the target is located along a particular LOS path. . . .	130
5.13	The convergence of the particle filter after 10 iterations The filter has completely converged around the location of the target.	131
5.14	Estimated positions of a stationary target at different positions. The estimated position was taken after 50 iterations of a particle filter with 200 particles. The average error for this experiment was .83 meters. . .	132
5.15	Estimated positions of a human walking along a known path. Here, the particle filter uses 200 particles and tracks with an average error of 1.02 meters.	133

LIST OF TABLES

1.1 Chapter 2 and 3 symbols, in the order in which they appear.	11
1.2 Chapter 4 symbols, in the order in which they appear.	12
1.3 Chapter 5 symbols, in the order in which they appear.	13
2.1 Gaussian-Mixture Noise Model Parameters Estimated From Measure- ments	34
2.2 Reconstruction parameters used to generate MSE bound surfaces. . . .	34
2.3 Image reconstruction parameters	35
3.1 Calibration and model parameters	61
4.1 VRTI image reconstruction parameters	88
5.1 Linear parameter fitting for the skew-Laplace likelihood model	118

ACKNOWLEDGMENTS

I would first like to acknowledge and thank my advisor Neal Patwari. Neal has been an absolutely terrific advisor, and this work would not have been possible without him. He had the guts and vision to do the original radio tomography experiment, before any previous results existed. Neal has the rare combination of strength and humility that are not found in most people. Neal, thanks so much for this opportunity. Working with you on this research has been a joy from day one. I consider myself extremely lucky and blessed to have landed in the SPAN lab with you at the helm.

I appreciate the friendship and support of other graduate students in the SPAN lab at the University of Utah: Dustin Maas, Jessica Croft, Piyush Agrawal, and Yang Zhao. Each of their unique skills and personalities was a great help to me during my research. Our many discussions, often at the expense of their time, led me to better ideas and corrected problems.

I want to express my love and appreciation for my family and friends. My parents, Ted and Kathy Wilson, have given me so many opportunities that have allowed me to accomplish this educational goal. Ben, Jenny, Missy, and Jessica, my brother and sisters, have all been key supporters for me. I thank the Holmstrom family for their love, and for seeding in me an excitement for science and technology.

Finally, and most importantly, to my beautiful wife Shellie and sons Owen and Adam, I cannot thank you enough for your support and love during my studies. You have made many sacrifices to enable this accomplishment, and I love you for it. Shellie, your support was more critical than any technical knowledge or discovery in accomplishing this goal.

CHAPTER 1

INTRODUCTION

1.1 Copyright Notice

Some material contained within this dissertation has been previously published and is used with permission.

- Copyright 2010 IEEE, Reprinted, with permission, from IEEE Transactions on Mobile Computing, “Radio Tomographic Imaging With Wireless Networks”, J. Wilson and N. Patwari.
- Copyright 2010 IEEE, Reprinted, with permission, from IEEE Transactions on Mobile Computing, “See Through Walls: Motion Tracking Using Variance-Based Radio Tomography Networks”, J. Wilson and N. Patwari.

1.2 Overview of Device-Free Localization

Knowing the location of people is extremely valuable. Global positioning systems (GPS), radio frequency identification (RFID) and real-time location systems (RTLS) have proven their value for locating targets with an attached device. Device-free localization (DFL) is the practice of locating people or objects when no tag or device is attached to the entity being located. This dissertation discusses some new and cost-effective methods for locating people through received signal strength (RSS) measurements in wireless networks.

The term “device-free localization” is important in distinguishing DFL systems from “passive” tagging systems. In passive RFID, for example, the entities being tracked or detected carry a device that back-scatters a signal using an electromagnetic resonance structure. Although the tag is not actively powered by a voltage source, it cannot be considered device-free. The terms “tagless” and “tag-free” are often used synonymously with “device-free.”

DFL technologies are useful in applications where the targets being tracked and detected are not expected to cooperate with the system. This may be the case either because the entities being tracked are evading surveillance, because they are unable, or because they do not want to be inconvenienced by carrying a device. Examples of such applications are listed below.

- Security and alarm systems
- Military, police, and SWAT operations
- Fire and disaster rescue
- Shopper and retail behavior analysis
- Elderly and handicap assistance
- Home and building automation

The practicality of each of these applications is sensitive to financial costs. For example, military DFL systems may be extremely expensive and yet still practical for deployment. On the other hand, handicap assistance and building automation solutions must be achievable when constrained by much lower financial limits. Developing cost-effective tracking solutions for these and other applications is therefore an important field of research, and the methods discussed in this work are intended to provide cost-efficient DFL solutions.

1.3 Sensor technologies

A number of possible sensor technologies could be used for the purposes of DFL, depending on the needs and constraints of the application. Some applications may require a detailed view of the actions of the targeted entities, while others may only require a coarse estimate of location. This section describes the most common sensors used in DFL systems today, along with their advantages and disadvantages. Some successful DFL systems deploy a combination of the technologies described here [1].

1.3.1 Optical Cameras

The most common form of DFL sensor is the optical camera [2]. Cameras have the often desirable feature that details of the actions of an individual, or identification of the individual, can be determined. This can be very powerful in security systems, since the characteristics of the intruder can be monitored directly or reviewed at a later time. DFL systems are primarily concerned with the location of an individual, so video analytic software is used to infer the position of a target using data from one or more cameras.

Cameras suffer from a few key limitations. First, they cannot penetrate opaque materials and structures. If an object blocks the line-of-sight (LOS) path, the ability of the camera to monitor an area is severely hampered. This may be accidental or intentionally carried out by a perpetrator. Second, cameras require very large bandwidths to transfer data to a security processing station. Even low-resolution cameras require data rates that may be unreasonable for remote monitoring of sites. Third, cameras have a limited angle of view, so many devices may be required to cover a large area, or an area with many opaque obstructions. Video stitching systems are computationally expensive and difficult to maintain, since changes in the environment usually require adjustment of the positioning of the device. Finally, the ability to determine characteristics and actions of an individual may prevent its use in privacy-sensitive applications. For example, using cameras to track the location of a senior in a disability assistance system would be undesirable for most people. Tracking shoppers in retail stores may also fall into this category.

1.3.2 Thermal Cameras

Thermal cameras are a variant of the optical camera that are extremely powerful for many applications, especially police and military operations [3]. Thermal cameras utilize a directional heat sensor in similar form to those for optical sensing. The advantage here is that a thermal sensor does not need an external source of light to maintain vision of a subject. Thus, a thermal camera can track the location of an individual in the dark or through non-insulating obstructions like fabric. This can enable applications like concealed weapon and explosive detection [4].

Many of the limitations of the optical camera apply to the thermal version.

Limited view angles, insulating obstructions, and high bandwidths hamper a thermal sensor's effectiveness in obstructed areas. Furthermore, thermal cameras are in general much more expensive than their optical counterparts.

1.3.3 Infrared

Infrared cameras are essentially equivalent to optical cameras, except that they sense optical frequencies below that of what a human can see. This is useful for night-vision, as a scene can be illuminated by an infrared source while not being noticed with the naked eye.

Passive infrared (PIR) systems, on the other hand, rely on infrared frequencies that occur naturally from the area of surveillance. Most home security motion detection systems are based around PIR sensors, and are triggered by abrupt changes to the infrared image. Sunlight and other environmental factors can therefore easily trigger such a detector.

Once again, most of the same limitations of the optical camera apply to infrared cameras and sensors. Opaque obstructions, limited view angles, financial costs, and bandwidth issues may limit infrared camera effectiveness in some DFL applications.

1.3.4 Acoustic, Vibration, and Ultrasound

Microphones measure changes in air pressure in typical human audible frequencies (20Hz-22KHz). Acoustic DFL systems function by placing many microphones around an area. As a person or target moves throughout the vicinity, sound caused by the targets is captured by the microphones and processed to infer location. This can be done in a coarse manner, by detecting sounds within a particular radius of each microphone, or in a more sophisticated manner, by analyzing the strength and time of arrival of signals. This idea has been used in real-time sniper detection systems used by military organizations [5].

Vibration systems can allow a system to infer target location in a similar manner to that of acoustic microphone systems. Each sensor may have a particular radius of detection that can be used to determine a coarse location estimate, or a processing of multiple sensors can provide a continuous tracking solution [1]. Vibration sensors may also determine some characteristics of the target being tracked, such as

distinguishing between a human and a vehicle based on the amplitude or spectral components of vibration signals.

For some applications, using microphones and vibration sensors to infer target position is problematic. An intruder walking very quietly in a building may be able to evade a security system based on microphones, since some amount of ambient noise is always present. As another example, tracking someone in a grocery store with a microphone DFL system would also be difficult, as announcements or music over the store’s speaker system would cause a significant amount of interference. Vibration sensors may also fail for similar reasons.

Like acoustic sensors, ultrasound also takes advantage of air-pressure sensing, but it does so at frequencies that are inaudible to the human ear [6, 7]. Ultrasound can be used for DFL purposes by emitting an ultrasonic pulse, and then sensing the time of arrival, strength, and angle of arrival of the reflections in the environment. When a person enters an area, their body reflects these ultrasonic pulses and the system can estimate a position. Ultrasound may provide an attractive form of DFL in some scenarios, but obstructions like walls attenuate the signals significantly.

1.3.5 Radio Frequency

Another form of DFL utilizes radio frequency sensors [8]. In these systems, a target’s position can be inferred by measuring the reflection, absorption, scattering, and/or diffraction of an electromagnetic wave by the target’s mass. Radio frequency DFL systems (RF-DFL) have various forms, including ultra-wideband, narrowband, and RSS-based. Section 1.4 is a brief introduction to these different forms.

There is an advantage to sensing radio frequency (RF) energy to infer a target’s location as opposed to the alternatives previously discussed. Radio frequency waves can penetrate nonmetal walls, smoke [9], and other opaque obstructions. Thus RF-based DFL technologies do not require floodlights to work at night, and can locate people in a smoke-filled building, or from the exterior. The following section discusses RSS-DFL technologies, as this is the focus of the work presented in this dissertation.

1.4 Radio Frequency DFL Technologies

A significant quantity of research has shown results that locate people in buildings using RF sensor measurements [8, 10–21]. Results have been presented which count the number of people moving [12], estimate a person’s location [17, 18, 21, 22], and image the movements in an area of interest [15–17, 19], all in real-world multipath environments.

Previous work reports an accuracy of less than 1m of average error [11, 17, 18] or less than 2m median error over a 1500 m² area [21]; these results are at least as good as reported location error when locating radio tagged objects [23, 24]. The comparable accuracy is interesting given that these technologies are device-free.

1.4.1 Ultra-Wideband (UWB)

Ultra-wideband receivers measure the amplitudes, time delays, and phases of the multipath signals which exist in the radio channel. Measured at multiple probing times t , UWB measurements and the changes between them can be used to infer both the properties of the static propagation environment, and the changes in the environment which might indicate a moving person or object. UWB transceivers are certainly more cost-prohibitive than narrowband transceivers, but the ability to distinguish time delay is a key benefit.

Transmitting and receiving an UWB pulse (or for that matter, high bandwidth signal) allows one to measure the channel impulse response (CIR). Assume at time t , $N(t)$ multipath components arrive at the RX, with the i th component having complex amplitude gain of $\alpha_i(t)$ and time delay $\tau_i(t)$. As a complex value, $\alpha_i(t)$ can be written as $|\alpha_i(t)| \exp[j\angle\alpha_i(t)]$. The CIR is [25],

$$h(t, \tau) = \sum_{i=1}^N \alpha_i(t) \delta(\tau - \tau_i(t)) \quad (1.1)$$

where $\delta(\cdot)$ is the Dirac impulse function.

The knowledge of time delay provides important information about position. Comparing the delay $\tau_i(t)$ to the line-of-sight time delay (assuming it is known) indicates the excess delay, which gives some knowledge of the spatial incidence of the i th multipath. For example, if the path was assumed to result from a single change in direction, then that object that caused the bounce is located somewhere

on an ellipse of a certain size, with the TX and RX as foci [26]. When time delay is measured on multiple links, the intersection between ellipses is an estimate of the object location.

1.4.2 Narrowband

Narrowband receivers cannot provide information about individual multipath, only the signal magnitude and phase as a whole. However, narrowband transceivers are produced in high quantity for commercial applications, thus their low cost is a key part of enabling large scale RF sensor networks.

Narrowband wireless devices simply measure the sum of the contributions of all multipath. We consider a continuous-wave (CW) signal, which results in a received complex baseband voltage, \tilde{V} , of

$$\tilde{V} = V_T \sum_{i=1}^N \alpha_i(t) = \sum_{i=1}^N V_i(t) \quad (1.2)$$

where V_T is the complex baseband voltage at the TX, and $V_i(t) = V_T \alpha_i(t)$ is the complex baseband voltage of component i at the RX [25].

There is information about position contained in \tilde{V} . First, the information in the magnitude of \tilde{V} will be discussed below. Secondly, \tilde{V} , when compared to the \tilde{V} measured at other RX locations or at multiple antennas, provides information about the azimuth or elevation angles-of-arrival of the multipath signals [27], and can be used in multiple wave field reconstruction techniques.

Typical distributed wireless sensors have difficulty with accurate timing synchronization [28], and for coherent phase measurements, phase synchronization is required. Phase synchronization means that the carrier used by two different transceivers must have the same phase. Since the carrier phase changes from 0 to 2π each carrier cycle, timing synchronization errors must be much less than $1/f_c$, where f_c is the carrier frequency. For example, at 900 MHz, timing errors must be much smaller than one nanosecond. A future challenge in DFL is to either provide practical means for phase-coherent measurements of \tilde{V} at disparate sensors, such as interferometric methods [29], or to achieve some of the benefits of phase-coherent measurements using non-coherent measurements.

1.4.3 Received Signal Strength (RSS)

In this section, we consider measurements of RSS for the purposes of DFL. Compared to the narrowband measurements presented above, RSS is a magnitude-only measurement. Measurements of RSS are ubiquitous in nearly all wireless devices. The received power is the squared magnitude of the complex baseband voltage \tilde{V} . What we typically call the “received signal strength” (RSS) is a measurement of the received power in decibel terms. For a narrowband receiver, this power is

$$R_{dB} = 20 \log_{10} |\tilde{V}| = P_T + 20 \log_{10} \left| \sum_{i=1}^N \alpha_i(t) \right| \quad (1.3)$$

where $P_T = 20 \log_{10} |V_T|$.

One source of information in R_{dB} is its magnitude. For links with a strong LOS component, when that strong component is blocked, R_{dB} tends to decrease. This is called shadowing, and a sharp decrease in R_{dB} can be used to infer that a person or object is located along the LOS path [15].

Further, multipath fading is a source of location information. Depending on the phases of each $V_i(t)$, the sum in (1.2) may be destructive (with opposite phases) or constructive (with similar phases). Measurements of fading are one source of information about the location or number of moving people in the environment. Fading can be quantified, for example, with the variance of R_{dB} [12, 17], by the absolute value of differences [11, 30], or even the link quality indicator (LQI) [12].

The variance of R_{dB} has been shown to be approximately linearly related to the total power in multipath components affected by the movement in the environment [31].

Although individual RSS measurements are less informative about person location than UWB measurements, an RSS-only approach claims a few key strengths. The low cost of RSS-only narrowband radios allows for many nodes to be deployed in many cost-sensitive applications. Since measurements are made between pairs of RF sensors, the number of measurements increases as $\mathcal{O}(N^2)$, and the overall capability of the RF sensor network can be very significant. Since the sensing is performed in a distributed manner, the network can be thrown or launched around an area, a key advantage over large and centralized radar devices.

1.5 Contribution of this Dissertation

The work presented in this dissertation is focused on DFL systems using only RSS measurements in wireless networks. The following publications have resulted from this work.

- J. Wilson and N. Patwari, “Radio Tomographic Imaging in Wireless Networks”, IEEE Transactions on Mobile Computing, 2010 [15]
- J. Wilson and N. Patwari, “See Through Walls: Motion-Tracking Using Variance-Based Radio Tomography Networks”, IEEE Transactions on Mobile Computing, 2010 [17]
- J. Wilson and N. Patwari, “Regularization Methods for Radio Tomographic Imaging”, Proceedings of the Virginia Tech Wireless Symposium, 2009 [16]
- N. Patwari and J. Wilson, “RF Sensor Networks for Device-Free Localization and Tracking”, Proceedings of the IEEE. (Accepted) May, 2010
- N. Patwari and J. Wilson, “People-Sensing Spatial Characteristics of RF Sensor Networks”, arXiv:0911.1972 [cs.NI], Nov., 2009

The technologies discussed in this dissertation have led to the following awards:

- ACM Mobicom, “Best Demonstration”, San Francisco, California, 2008
- Winner of Opportunity Quest, The University of Utah Business Innovation Competition, 2009
- Finalist in the Utah Entrepreneurial Challenge, 2010

The research in this dissertation has been featured in international media, including:

- The Economist, “Looking Beyond: Through-the-Wall Vision”, Oct, 2009
- Discover Magazine, “Beyond X-Ray Vision”, May, 2010
- Der Spiegel, “Radio Waves: U.S. Scientists Peer Through Walls”, Oct, 2009
- Front page of NSF.gov, Nov, 2009

- KSL and Fox News in Salt Lake City, UT, Oct, 2009
- Online: Der Spiegel, UK Telegraph, MIT Technology Review, ScienceNow, Popular Science, Wired, Ars Technica, Slashdot, Lifehacker, and others.

Chapter 2 introduces a new technology called “radio tomographic imaging” (RTI). RTI images changes in attenuation by taking into account the drop in signal strength when a person is located on the LOS of a wireless link. Noise models for RTI are investigated, error bounds are derived, and experimental results are presented. Symbol definitions for this chapter are displayed in Table 1.1.

Chapter 3 discusses a few common forms of regularization for ill-posed inverse problems. These regularization methods are applied to RTI data, and the experimental results are presented. Some forms of regularization, such as Tikhonov, are appealing due to the computational simplicity. Others, such as total variation, provide sharper contrast at the cost of computational resources. Symbol definitions for this chapter are displayed in Table 1.1.

Chapter 4 presents a new form of RTI called variance-based radio tomographic imaging (VRTI). In rich multipath environments, the shadowing models developed in RTI are inaccurate. Signal strength changes no longer are the result of shadowing, but of multipath fading. To address this limitation, measurements of RSS variance are used to image motion within an area. Experimental results show that this technique can be used to track the location of a moving person behind walls. Symbol definitions for this chapter are displayed in Table 1.2.

Chapter 5 presents a statistical inversion approach to DFL in wireless networks. Instead of modeling the problem as a traditional least-squares formulation with regularization, likelihood distributions are modeled and used to statistically invert the problem. Results demonstrate the ability of the statistical inversion method to locate both moving and stationary targets behind walls. Symbol definitions for this chapter are displayed in Table 1.3.

Finally, chapter 6 concludes this dissertation. The key research findings are summarized, and opportunities for future research are discussed.

Table 1.1. Chapter 2 and 3 symbols, in the order in which they appear.

Symbol	Meaning
N, K, M	The number of pixels, nodes, and links in an RTI network
$y_i(t)$	The signal strength measured on link i at time t in dBm
P_i	The transmitted power on link i
$S_i(t)$	Shadowing loss on link i at time t in dB
$F_i(t)$	Fading loss on link i at time t in dB
L_i	Static loss on link i at time t in dB
$\nu_i(t)$	Measurement noise on link i at time t in dB
Δy_i	Change in RSS in dBm on link i
n_i	Measurement and modeling noise on link i
$\Delta \mathbf{y}$	Vector of change in RSS for each link
$\Delta \mathbf{x}$	Vector of change in attenuation for each pixel
W	Weighting or transfer matrix for the RTI model
d_{ij}	Distance from node i to node j
\mathbf{x}, \mathbf{y}	Aliases for $\Delta \mathbf{x}$ and $\Delta \mathbf{y}$
$\hat{\mathbf{x}}$	Estimate of \mathbf{x}
\mathbf{R}_ϵ	Error correlation matrix of \mathbf{x}
$\mathbf{J}_D, \mathbf{J}_P$	Fischer and prior information matrix
\mathbf{C}_X	Covariance matrix of \mathbf{x}
d_{kl}	Distance from pixel k to pixel l
Δ_p	Pixel width (m)
λ	Width of weighting ellipse
δ_c	Pixel correlation constant
σ_x^2	Pixel variance
γ	MSE Image error bound parameter
U, Σ, V	Singular value decomposition matrices
α	Regularization parameter
$\mathbf{D}_X, \mathbf{D}_Y$	Tikhonov difference matrices
R_H	Human radius
β	Total variation smoothness parameter

NSF Acknowledgement

This material is based upon work supported by the National Science Foundation under Grant No. ECCS-0748206. Any opinions, findings, and conclusions or recommendations expressed in this material are those of the authors and do not necessarily reflect the views of the National Science Foundation.

Table 1.2. Chapter 4 symbols, in the order in which they appear.

Symbol	Meaning
N	Number of pixels in an image
M	Number of links in a network
$x(j)$	A binary variable indicating if motion occurs in pixel j
\tilde{V}	Complex baseband voltage measured at the receiver
ν	Additive noise measured at the receiver
V_i	Magnitude of i th multipath component
Φ_i	Phase of i th multipath component
R_{dB}	Received signal power in dB
w_j	Variance caused by motion in pixel j
\mathbf{W}	Weighting matrix for each pixel and link
\mathbf{s}	Variance vector measured on each link of the network
\mathbf{n}	Noise vector for each link of the network
T_{AP}	Total affected power
$\mathcal{A}(\mathbf{x})$	Indices of affected multipath components
\tilde{V}	Specular voltage measured at the receiver
Φ	Specular phase measured at the receiver
K	K factor of a Rician random variable
σ^2	Affected power and noise variance
σ_v^2	Variance of noise ν
\mathcal{S}_i	Subset of space for propagation of link i
\mathbf{z}_j	Location of the center of pixel j
d_l	Length of link l from node to node
$d_{lj}(1), d_{lj}(2)$	Distance of pixel j to each node of link l
\mathbf{x}_{Tik}	Tikhonov regularized estimation of \mathbf{x}
\mathbf{Q}	Tikhonov matrix
v_m	Kalman state process standard deviation
v_n	Kalman measurement noise standard deviation
Δ_p	Pixel width (ft)
λ	Width parameter of weighting ellipse (ft)
α	Regularization parameter
ψ	Variance weighting scale $(dB)^2$
N_B	Length of RSS buffer
ϵ, ζ	Average tracking error for natural and spot movement

Table 1.3. Chapter 5 symbols, in the order in which they appear.

Symbol	Meaning
F	Fade level of a link
P_m	Mean received signal strength of a link
X	State space
Y	Measurement space
P_T	Transmitted power
$P(d)$	Ensemble mean power at distance d
Π_0	Reference power
Δ_0	Reference distance
a	Negative decay of skew-Laplace distribution
b	Positive decay of skew-Laplace distribution
ψ	Mode of skew-Laplace distribution
\mathbf{x}_k	True location of targets at time k
$\tilde{\mathbf{x}}_k^i$	Particle proposal i at time k
w_k^i	Weighting of particle i at time k
\mathbf{y}_k	Change in signal strength at time k

CHAPTER 2

RADIO TOMOGRAPHIC IMAGING WITH WIRELESS NETWORKS

2.1 Abstract

Radio Tomographic Imaging (RTI) is an emerging technology for imaging the attenuation caused by physical objects in wireless networks. This paper presents a linear model for using received signal strength (RSS) measurements to obtain images of moving objects. Noise models are investigated based on real measurements of a deployed RTI system. Mean-squared error (MSE) bounds on image accuracy are derived, which are used to calculate the accuracy of an RTI system for a given node geometry. The ill-posedness of RTI is discussed, and Tikhonov regularization is used to derive an image estimator. Experimental results of an RTI experiment with 28 nodes deployed around a 441 square foot area are presented.

2.2 Introduction

When an object moves into the area of a wireless network, links which pass through that object will experience shadowing losses. This paper explores in detail the use of shadowing losses on links between many pairs of nodes in a wireless network to image the attenuation of objects within the network area. We refer to this problem as *radio tomographic imaging*¹ (RTI), as depicted Fig. 2.1.

RTI may be useful in emergencies, rescue operations, and security breaches, since the objects being imaged need not carry an electronic device. Using the images to track humans moving through a building, for example, provides a basis for new applications in security systems and “smart” buildings.

¹This chapter first appeared in J. Wilson and N. Patwari, “Radio Tomographic Imaging with Wireless Networks”, IEEE Transactions on Mobile Computing, 2010, and is reprinted with permission.

The reduction in costs for radio frequency integrated circuits (RFICs) and advances in peer-to-peer data networking have made realistic the use of hundreds or thousands of simple radio devices in a single RTI deployment. Since the relative cost of such devices is low, large RTI networks are possible in applications that may be otherwise impractical.

Radio tomography draws from the concepts of two well-known and widely used types of imaging systems. First, radar systems transmit RF probes and receive echoes caused by the objects in an environment [32]. A delay between transmission and reception indicates a distance to a scatterer. Phased array radars also compute an angle of bearing. Such systems image an object in space based on reflection and scattering. Secondly, computed tomography (CT) methods in medical and geophysical imaging systems use signal measurements along many different paths through a medium. The measurements along the paths are used to compute an estimate of the spatial field of the transmission parameters throughout the medium [33]. RTI is also a transmission-based imaging method which measures signal strengths on many different paths through a medium, but similar to radar systems, it does so at radio frequencies. It also faces two significant challenges:

- The system discussed in this paper measures only signal strength. No information about the phase or the time-domain of a signal is available.
- The use of RF, as opposed to much higher frequency EM waves (*e.g.*, x-rays), introduces significant non-line-of-sight (NLOS) propagation in the transmission measurements. Signals in standard commercial wireless bands do not travel in just the line-of-sight (LOS) path, and instead propagate in many paths from a transmitter to a receiver.

2.2.1 Applications

Despite the difficulties of using RF, there is a major advantage: RF signals can travel through obstructions such as walls, trees, and smoke, while optical or infrared imaging systems cannot. RF imaging will also work in the dark, where video cameras will fail. Even for applications where video cameras *could* work, privacy concerns may prevent their deployment. An RTI system provides current

images of the location of people and their movements, but cannot be used to identify a person.

One main future application of RTI is to reduce injury for correctional and law enforcement officers; many are injured each year because they lack the ability to detect and track offenders through building walls [34]. By showing the locations of people within a building during hostage situations, building fires, or other emergencies, RTI can help law enforcement and emergency responders to know where they should focus their attention.

Another application is in automatic monitoring and control in “smart” homes and buildings. Some building control systems detect motion in a room and use it to control lighting, heating, air conditioning, and even noise cancellation [35]. RTI systems can further determine how many people are in a room and where they are located, providing more precise control.

RTI has application in security and monitoring systems for indoor and outdoor areas. For example, most existing security systems are trip-wire based or camera-based. Trip-wire systems detect when people cross a boundary, but do not track them when they are within the area. Cameras are ineffective in the dark and have limited view angles. An RTI system could serve both as a trip-wire, alerting when intruders enter into an area, and a tracking system to follow their movements.

2.2.2 Related Work

RF-based imaging has been dominated in the commercial realm by ultra-wideband (UWB) based through-the-wall (TTW) imaging devices from companies like Time Domain [36], Cambridge Consultants [37], and Camero Tech [38]. These companies have developed products using a phased array of radars that transmit UWB pulses and then measure echoes to estimate a range and bearing. These devices are accurate close to the device, but inherently suffer from accuracy and noise issues at long range due to mono-static radar scattering losses and large bandwidths. Some initial attempts [39] allow 2-4 of these high-complexity devices to collaborate to improve coverage.

In comparison, in this paper we discuss using dozens to hundreds of low-capability collaborating nodes, which measure transmission rather than scattering and reflec-

tion. Further, UWB uses an extremely wide RF bandwidth, which may limit its application to emergency and military applications. RTI is capable of using radios with relatively small bandwidths.

To emphasize the small required bandwidth compared to UWB, some relevant research is being called “ultra-narrowband” (UNB) radar [40–42]. These systems propose using narrowband transmitters and receivers deployed around an area to image the environment within that area. Measurements are phase-synchronous at the multiple nodes around the area. Such techniques have been applied to detect and locate objects buried under ground using what is effectively a synthetic aperture array of ground-penetrating radars [43]. Experiments have been reported which measure a static environment while moving one transmitter or one receiver [42], and measure a static object on a rotating table in an anechoic chamber in order to simulate an array of transmitters and receivers at many different angles [40, 42, 43].

Multiple-input-multiple-output (MIMO) radar is another emerging field that takes advantage of multiple transmitters and receivers to locate objects within a spatial area [44]. In this framework, signals are transmitted into the area of interest, objects scatter the signal, and the reflections are measured at each receiver. The scattering objects create a channel matrix which is comparable to the channel matrix in MIMO communication theory. RTI differs from MIMO radar in the same way that it differs from traditional radar. Instead of measuring reflections, RTI uses the shadowing caused by objects as a basis for image reconstruction.

Recent research has also used measurements of signal strength on 802.11 WiFi links to detect and locate a person’s location. Experiments in [13] demonstrate the capability of a detector based on signal strength measurements determine the location of a person who is not carrying an electronic device. In this case, the system is trained by a person standing at known positions, and RSS measurements are recorded at each location. When the system is in use, RSS measurements are compared with the known training data, and the best position is selected from a list.

Our approach is not based on point-wise detection. Instead, we use tomographic methods to estimate an image of the change in the attenuation as a function of space, and use the image estimate for the purposes of indicating the position of a moving

object.

2.2.3 Overview

Section 2.3 presents a linear model relating RSS measurements to the change in attenuation occurring in a network area, and investigates statistics for noise in dynamic multipath environments. Section 2.4 describes an error bound on image estimation for a given node geometry. This is useful to determine which areas of a network can be accurately imaged for a given set of node locations. Section 2.5 discusses the ill-posedness of RTI, and derives a regularized solution for obtaining an attenuation image. Section 2.6 describes the setup of an actual RTI experiment, the resultant images, and a discussion of the effect of parameters on the accuracy of the images.

2.3 Model

2.3.1 Linear Formulation

When wireless nodes communicate, the radio signals pass through the physical area of the network. Objects within the area absorb, reflect, diffract, or scatter some of the transmitted power. The goal of an RTI system is to determine an image vector of dimension \mathbb{R}^N that describes the amount of radio power attenuation occurring due to physical objects within N voxels of a network region. Since voxel locations are known, RTI allows one to know where attenuation in a network is occurring, and therefore, where objects are located.

If K is the number of nodes in the RTI network, then the total number of unique two-way links is $M = \frac{K^2-K}{2}$. Any pair of nodes is counted as a link, whether or not communication actually occurs between them. The signal strength $y_i(t)$ of a particular link i at time t is dependent on:

- P_i : Transmitted power in dB.
- $S_i(t)$: Shadowing loss in dB due to objects that attenuate the signal.
- $F_i(t)$: Fading loss in dB that occurs from constructive and destructive interference of narrow-band signals in multipath environments.

- L_i : Static losses in dB due to distance, antenna patterns, device inconsistencies, etc.
- $\nu_i(t)$: Measurement noise.

Mathematically, the received signal strength is described as

$$y_i(t) = P_i - L_i - S_i(t) - F_i(t) - \nu_i(t) \quad (2.1)$$

The shadowing loss $S_i(t)$ can be approximated as a sum of attenuation that occurs in each voxel. Since the contribution of each voxel to the attenuation of a link is different for each link, a weighting is applied. Mathematically, this is described for a single link as

$$S_i(t) = \sum_{j=1}^N w_{ij} x_j(t). \quad (2.2)$$

where $x_j(t)$ is the attenuation occurring in voxel j at time t , and w_{ij} is the weighting of pixel j for link i . If a link does not “cross” a particular voxel, that voxel is removed by using a weight of zero. For example, Fig. 2.2 is an illustration of how a direct LOS link might be weighted in a nonscattering environment.

Imaging only the *changing* attenuation greatly simplifies the problem, since all static losses can be removed over time. The change in RSS Δy_i from time t_a to t_b is

$$\begin{aligned} \Delta y_i &\equiv y_i(t_b) - y_i(t_a) \\ &= S_i(t_b) - S_i(t_a) + F_i(t_b) - F_i(t_a) \\ &\quad + \nu_i(t_b) - \nu_i(t_a), \end{aligned} \quad (2.3)$$

which can be written as

$$\Delta y_i = \sum_{j=1}^N w_{ij} \Delta x_j + n_i, \quad (2.4)$$

where the noise is the grouping of fading and measurement noise

$$n_i = F_i(t_b) - F_i(t_a) + \nu_i(t_b) - \nu_i(t_a) \quad (2.5)$$

and

$$\Delta x_j = x_j(t_b) - x_j(t_a) \quad (2.6)$$

is the difference in attenuation at pixel j from time t_a to t_b .

If all links in the network are considered simultaneously, the system of RSS equations can be described in matrix form as

$$\Delta \mathbf{y} = \mathbf{W} \Delta \mathbf{x} + \mathbf{n} \quad (2.7)$$

where

$$\begin{aligned} \Delta \mathbf{y} &= [\Delta y_1, \Delta y_2, \dots, \Delta y_M]^T \\ \Delta \mathbf{x} &= [\Delta x_1, \Delta x_2, \dots, \Delta x_N]^T \\ \mathbf{n} &= [n_1, n_2, \dots, n_M]^T \\ [\mathbf{W}]_{i,j} &= w_{ij} \end{aligned} \quad (2.8)$$

In summary, $\Delta \mathbf{y}$ is the vector of length M all link difference RSS measurements, \mathbf{n} is a noise vector, and $\Delta \mathbf{x}$ is the attenuation image to be estimated. \mathbf{W} is the weighting matrix of dimension $M \times N$, with each column representing a single voxel, and each row describing the weighting of each voxel for that particular link. Each variable is measured in decibels (dB).

To simplify the notation used throughout the rest of this paper, \mathbf{x} and \mathbf{y} are used in place of $\Delta \mathbf{x}$ and $\Delta \mathbf{y}$, respectively.

2.3.2 Weight Model

If knowledge of an environment were available, one could estimate the weights $\{w_{ij}\}_j$ for link i which reflected the spatial extent of multiple paths between transmitter and receiver. Perhaps calibration measurements could aid in estimation of the linear transformation \mathbf{W} . However, with no site-specific information, we require a statistical model that describes the linear effect of the attenuation field on the path loss for each link.

An ellipsoid with foci at each node location can be used as a method for determining the weighting for each link in the network [45]. If a particular voxel falls outside the ellipsoid, the weighting for that voxel is set to zero. If a particular voxel is within the LOS path determined by the ellipsoid, its weight is set to be inversely proportional to the square root of the link distance. Intuitively, longer links will provide less information about the attenuation in voxels that they cross. When link distances are very long, the signals reflect and diffract around the obstructions. A

link with a distance of only a few feet will experience more change in RSS when an obstruction occurs than a link with a length of hundreds of feet.

Past studies have shown that the variance of link shadowing does not change with distance. In accordance with these studies, dividing by the square root of the link distance ensures that the voxel weighting takes this into account [46]. The weighting is described mathematically as

$$w_{ij} = \frac{1}{\sqrt{d}} \begin{cases} 1 & \text{if } d_{ij}(1) + d_{ij}(2) < d + \lambda \\ 0 & \text{otherwise} \end{cases} \quad (2.9)$$

where d is the distance between the two nodes, $d_{ij}(1)$ and $d_{ij}(2)$ are the distances from the center of voxel j to the two node locations for link i , and λ is a tunable parameter describing the width of the ellipse.

The width parameter λ is typically set very low in RTI, such that it is essentially the same as using the LOS model as depicted in Fig. 2.2. The use of an ellipsoid is primarily used to simplify the process of determining which voxels fall along the LOS path.

2.3.3 Noise

To complete the model of (2.7), the statistics of the noise vector \mathbf{n} in (2.7) must be examined. Here, noise is caused by time-varying measurement miscalibration of the receiver, by the contribution of thermal noise to the measured receiver signal strength, and time-variations in the multipath channel not caused by changes to the attenuation experienced by the line-of-sight path. If these contributions are constant with time, then the calibration (when moving attenuator existed in the field) would have been able to establish it as the baseline. Time variation in RSS measurement when no moving attenuator is blocking the line-of-sight path is “noise” for an RTI system.

Past studies have considered the time-variation of RSS in fixed radio links. In particular, the work and measurements of Bultitude [47] were used to design indoor fixed wireless communications systems which periodically experienced fading due to motion in the area of the link. Bultitude found that RSS experienced intervals of significant fading which were caused by human motion in and around the area. Most of the time, the measured RSS vary slowly around a nearly constant mean, what we call a *nonfading interval*. When in a fading interval, RSS varies up to 10 dB

higher and 20 dB below the nonfading interval mean, with a distribution that can be characterized as a Rician distribution [47]. Other measurements find temporal fading statistics more closely match a log-normal distribution [48]. The fading / nonfading interval process can be modeled as a two-state Markov chain [49], which alternates between a low-variance and high-variance distribution. Over all time, measurements show a two-part mixture distribution for the RSS on a fixed link.

In linear terms, we could model this data as a mixture of two Rician distributions as in [47]; we could also model it as a mixture of log-normal terms as suggested by results in [48]. We note that the logarithm of a Rician random variable is often similar in distribution to the log-normal, perhaps a cause of disagreement between measurement studies. We choose to use the log-normal mixture model for simplicity; in the (dB) scale, this is a two-part Gaussian mixture model:

$$f_{n_i}(u) = \sum_{k \in \{1,2\}} \frac{p_k}{\sqrt{2\pi\sigma_k^2}} \exp \left[-\frac{u^2}{2\sigma_k^2} \right], \quad (2.10)$$

where p_k is the probability of part k , $p_2 = 1 - p_1$, σ_k^2 is the variance of part k , and $f_{n_i}(u)$ is the probability density function of the noise random variable n_i . Without loss of generality, we let $\sigma_2 > \sigma_1$ so that part 2 is the higher variance component of the mixture.

Past radio link measurements have not distinguished between motion which shadows the line-of-sight path (the signal in RTI), and motion which does not shadow the line-of-sight path (the noise) [13, 47–49]. To investigate the statistics of RTI noise, we present experimental tests which measure the time-varying statistics of links during motion which does not obstruct a link.

To collect experimental samples of noise, we set up 28 nodes in an indoor office area empty of people. While the nodes are transmitting and measuring RSS on each pairwise link, people move around the outside of the perimeter of the deployment area. In no case did the motion of a person obstruct the LOS path of any link. From each link, about 66,000 measurements were taken. For example, consider the data on a typical link, the link (3, 20). The temporal fading plot in Figure 2.3(a) shows similar results to [47], with alternating periods of heavy fading and low fading. During low fading, data are confined within a range of 2-3 dB around -84 dBm. During high fading, variations at ± 10 dB from the mean occur. The histogram

shown in Fig. 2.3(b) correspondingly shows a mixture of one high-variance and one low-variance distribution.

We also summarize the measured data on all $\binom{28}{2}$ links. The mean was removed from each link's data, and the data was merged. Fig. 2.4(a) is a quantile-quantile plot comparing the removed-mean RSS measurements with a Gaussian distribution $\mathcal{N}(0, \sigma_d^2)$, where σ_d^2 is the empirical variance of the measurements. The PDF is approximated by a Gaussian within ± 2.5 quantiles.

As described, the data seems to follow a mixture distribution. From measured data, we estimate the mixture parameters with an expectation-maximization (EM) algorithm [50], and the results are shown in Table 2.1. Fig. 2.4(b) is a quantile-quantile plot comparing the removed-mean RSS measurements with a mixture model with the stated parameters.

2.4 Error Bound

2.4.1 Derivation

This section presents a lower bound on estimation error for the linear model (2.7) under the noise model discussed in Section 2.3.3. The estimation error vector is defined as $\epsilon = \hat{\mathbf{x}} - \mathbf{x}$, and the error *correlation matrix* is

$$\mathbf{R}_\epsilon = E[\epsilon \epsilon^T]. \quad (2.11)$$

A well-known result in estimation theory known as the *MSE*, *Bayesian* or *Van Trees* bound states that the error correlation matrix is bounded by

$$\mathbf{R}_\epsilon \geq (\mathbf{J}_D + \mathbf{J}_P)^{-1} = \mathbf{J}^{-1} \quad (2.12)$$

where the inequality indicates that the matrix $\mathbf{R}_\epsilon - \mathbf{J}^{-1}$ is positive semi-definite [51]. The matrix

$$\mathbf{J}_D = E[\{\nabla_x[\ln P(\mathbf{y}|\mathbf{x})]\} \{\nabla_x[\ln P(\mathbf{y}|\mathbf{x})]\}^T] \quad (2.13)$$

is known as the *Fisher information matrix* and represents the information obtained from the data measurements. The matrix

$$\mathbf{J}_P = E[\{\nabla_x[\ln P(\mathbf{x})]\} \{\nabla_x[\ln P(\mathbf{x})]\}^T] \quad (2.14)$$

represents the information obtained from a priori knowledge about the random parameters.

We assume that the noise components $\mathbf{n} = [n_1, \dots, n_M]^T$ are independent and identically distributed as two-component zero-mean Gaussian mixture random variables as in (2.10). The noise is independent because we assume nodes are placed at distances larger than the coherence distance of the indoor fading channel.

From (2.13), we can derive that \mathbf{J}_D is given by [52, Eqn 10],

$$\begin{aligned} \mathbf{J}_D &= \gamma \mathbf{W}^T \mathbf{W} \\ \text{where } \gamma &= \int_{-\infty}^{\infty} \frac{[f'_{n_i}(u)]^2}{f_{n_i}(u)} du \end{aligned} \quad (2.15)$$

and $f'_{n_i}(u)$ is the derivative of $f_{n_i}(u)$ with respect to u . When $p_2 = 0$, that is, the distribution of n_i is purely Gaussian, γ reverts to $1/\sigma_1^2$, one over the variance of the distribution. For two-component Gaussian mixtures, we compute γ in (2.15) from numerical integration. For example, for the Gaussian-mixture model parameters calculated from the measurement experiment, as given in Table 2.1, we find $\gamma = 0.548$.

To calculate \mathbf{J}_P , the prior image distribution $P(\mathbf{x})$ must be known or assumed. One possibility is to assume that \mathbf{x} is a zero-mean Gaussian random field with covariance matrix \mathbf{C}_x . Then

$$P(\mathbf{x}) = \frac{1}{\sqrt{(2\pi)^N |\mathbf{C}_x|}} e^{-\frac{1}{2}(\mathbf{x}^T \mathbf{C}_x^{-1} \mathbf{x})} \quad (2.16)$$

Plugging (2.16) into (2.14) results in

$$\mathbf{J}_P = \mathbf{C}_x^{-1}. \quad (2.17)$$

These derivations of \mathbf{J}_D and \mathbf{J}_P lead to the linear MSE bound for RTI

$$\mathbf{R}_\epsilon \geq (\gamma \mathbf{W}^T \mathbf{W} + \mathbf{C}_x^{-1})^{-1}. \quad (2.18)$$

An important result of the bound in (2.18) comes from the following property [51]

$$E[(\mathbf{x} - \hat{\mathbf{x}})_i^2] \geq (\gamma \mathbf{W}^T \mathbf{W} + \mathbf{C}_x^{-1})_{ii}^{-1} = \mathbf{J}_{ii}^{-1} \quad (2.19)$$

where $E[(\mathbf{x} - \hat{\mathbf{x}})_i^2]$ represents the mean-squared-error for pixel i . In other words, the diagonal elements of \mathbf{J}^{-1} are the lower bounds on the mean-squared-error for the corresponding pixels.

2.4.2 Spatial Covariance Model

Previous work has shown that an exponential function is useful in approximating the spatial covariance of an attenuation field [53], [46]. The exponential covariance is a close approximation to the covariance that results from modeling the spatial attenuation as a Poisson process, a common assumption for random placement of objects in space. Applying this model, the a priori covariance matrix \mathbf{C}_x is generated by

$$[\mathbf{C}_x]_{kl} = \sigma_x^2 e^{-d_{kl}/\delta_c}, \quad (2.20)$$

where d_{kl} is the distance from pixel k to pixel l , δ_c is a “space constant” correlation parameter, and σ_x^2 is the variance at each pixel.

The exponential spatial covariance model is appealing due to its simplicity and low number of parameters. Other models based on different distributions of attenuating objects could also be utilized.

2.4.3 Example Error Bounds

The bound in (2.19) provides a theoretical basis for determining the accuracy of an image over the network area. The node locations affect which pixels are accurately estimated, and which are not. To visualize how the node locations affect the accuracy of the image estimation, three examples are provided in Figs. 2.5, 2.6 and 2.7. Table 2.2 shows the parameters of the normalized ellipse weighting model that were used to generate these bounds.

As seen in the surfaces of Figs. 2.5, 2.6 and 2.7, voxels that are crossed by many links have a higher accuracy than voxels that are rarely or never crossed. The voxels in the corners of the square deployment, the sides of the front-back deployment, and the low-density areas in the random deployment, are crossed only by a few links. In some voxels, no links cross at all, and the bound surface is limited only by the covariance of the prior statistics. The known covariance of the image has the effect of smoothing the bound surface, since knowledge of the attenuation of a voxel is statistically related to its neighbors.

2.4.4 Effect of Node Density

The node density plays a key role in the accuracy of an RTI result. Imaging can be expected to be more accurate in areas where nodes are placed closely together

than in areas where nodes are spaced at large distances. When many links pass through a particular area, more RSS information can be used to reconstruct the attenuation occurring in that area. This has the effect of averaging out noise and other corruptions in the measurements. Furthermore, when links are close together, the RSS information is more concentrated on the voxels that are crossed. This is due to the weighting function that is inversely proportional to the square root of the link distance.

To illustrate the effect of node density on the MSE bound, Fig. 2.8 shows the lower bound on the average MSE over all voxels for the three deployment geometries as the density is increased. For each point on the curves, the bound surface is calculated, then averaged over all voxels. The parameters are equal to those used previously in Table 2.2. Each geometry contains the same number of nodes for each point on the curve, and is deployed around the same area. In the square geometry, nodes are placed uniformly around a square area. In the front-back geometry, the same number of nodes are placed along two sides of the square, resulting in the same number of nodes per square foot. In the random geometry, the same number of nodes are randomly placed throughout the square.

In all three cases shown in Fig. 2.8, the lower bound on average MSE for each deployment decreases rapidly with increasing node density. The square geometry outperforms the others, due to the fact that the entire area of the square is surrounded by nodes. There are very few voxels that are not crossed by at least a few links, and many short links exist that cross the corners of the square. The random geometry performs the worst out of the three when density is low, largely due to the fact that in a random deployment, many voxels will not be crossed by any links. As density increases, the random deployment out-performs the front-back geometry because nodes are closer together, and the density is such that very few areas contain voxels that are not crossed by at least some links.

2.5 Image Reconstruction

2.5.1 Ill-posed Inverse Problem

Linear models for many physical problems, including RTI, take the form of

$$\mathbf{y} = \mathbf{W}\mathbf{x} + \mathbf{n} \quad (2.21)$$

where $\mathbf{y} \in \mathbb{R}^M$ is measured data, $\mathbf{W} \in \mathbb{R}^{M \times N}$ is a transfer matrix of the model parameters $\mathbf{x} \in \mathbb{R}^N$, and $\mathbf{n} \in \mathbb{R}^M$ is a measurement noise vector. When estimating an image from measurement data, it is common to search for a solution that is optimal in the least-squared-error sense.

$$\mathbf{x}_{LS} = \arg \min_{\mathbf{x}} \|\mathbf{W}\mathbf{x} - \mathbf{y}\|_2^2 \quad (2.22)$$

In other words, the least-squares solution minimizes the noise energy required to fit the measured data to the model. The least-square solution can be obtained by setting the gradient of (2.22) equal to zero, resulting in

$$\mathbf{x}_{LS} = (\mathbf{W}^T \mathbf{W})^{-1} \mathbf{W}^T \mathbf{y} \quad (2.23)$$

which is only valid if \mathbf{W} is full-rank. This is not the case in an RTI system.

RTI is an ill-posed inverse problem, meaning that small amounts of noise in measurement data are amplified to the extent that results are meaningless. This is due to very small singular values in the transfer matrix \mathbf{W} that cause certain spectral components to grow out of control upon inversion. To see this, \mathbf{W} is replaced by its singular value decomposition (SVD):

$$\mathbf{W} = \mathbf{U} \mathbf{\Sigma} \mathbf{V}^T \quad (2.24)$$

where \mathbf{U} and \mathbf{V} are unitary matrices, and $\mathbf{\Sigma}$ is a diagonal matrix of singular values. Plugging (2.24) into (2.23), the least squares solution can be written as

$$\mathbf{x}_{LS} = \mathbf{V} \mathbf{\Sigma}^{-1} \mathbf{U}^T \mathbf{y} = \sum_{i=1}^N \frac{1}{\sigma_i} \mathbf{u}_i^T \mathbf{y} \mathbf{v}_i \quad (2.25)$$

where \mathbf{u}_i and \mathbf{v}_i are the i th columns of \mathbf{U} and \mathbf{V} , and σ_i is the i th diagonal element of $\mathbf{\Sigma}$. It is evident that when singular values are zero or close to zero, the corresponding singular basis vectors are unbounded upon inversion.

The heuristic explanation for the ill-posedness of the RTI model lies in the fact that many pixels are estimated from relatively few nodes. There are multiple possible attenuation images that can lead to the same set of measurement data. For example, assume a particular pixel is not crossed by any link in the network. This would result in the same measurement data for every possible attenuation value of that pixel, so inversion of the problem would be impossible.

Regularization involves introducing additional information into the mathematical cost model to handle the ill-posedness. In some methods, a regularization term $J(\mathbf{x})$ is added to the minimization objective function of the original problem as

$$f_{reg} = f(\mathbf{x}) + \alpha J(\mathbf{x}), \quad (2.26)$$

where α is the weighting parameter. Small values of α lead to solutions that fit the data, while large values favor the solution that matches prior information.

Some regularization techniques follow from a Bayesian approach, where a certain prior distribution is imposed on the model parameters. Other forms of regularization modify or eliminate small singular values of the transfer matrix. An overview of regularization and image reconstruction in general can be found in [54] and [55].

2.5.2 Tikhonov Regularization

In *Tikhonov* regularization [54], an energy term is added to the least squares formulation, resulting in the objective function

$$f(x) = \frac{1}{2} \|\mathbf{W}\mathbf{x} - \mathbf{y}\|^2 + \alpha \|\mathbf{Q}\mathbf{x}\|^2, \quad (2.27)$$

where \mathbf{Q} is the *Tikhonov matrix* that enforces a solution with certain desired properties.

In this paper, we use a difference matrix approximating the derivative operator as the Tikhonov matrix \mathbf{Q} . By minimizing the energy found within the image derivative, noise spikes are suppressed and a smooth image is produced. This form of Tikhonov regularization is known as *H1 regularization*.

Since the image is two dimensional, the regularization should include the derivatives in both the vertical and horizontal directions. The matrix \mathbf{D}_X is the difference operator for the horizontal direction, and \mathbf{D}_Y is the difference operator for the vertical direction. The regularized function can be written in this case as

$$f(\mathbf{x}) = \frac{1}{2} \|\mathbf{W}\mathbf{x} - \mathbf{y}\|^2 + \alpha (\|\mathbf{D}_X \mathbf{x}\|^2 + \|\mathbf{D}_Y \mathbf{x}\|^2). \quad (2.28)$$

Taking the derivative and setting equal to zero results in the solution

$$\hat{\mathbf{x}} = (\mathbf{W}^T \mathbf{W} + \alpha (\mathbf{D}_X^T \mathbf{D}_X + \mathbf{D}_Y^T \mathbf{D}_Y))^{-1} \mathbf{W}^T \mathbf{y}. \quad (2.29)$$

One major strength of Tikhonov regularization lies in the fact that the solution is simply a linear transformation Π of the measurement data.

$$\Pi = (\mathbf{W}^T \mathbf{W} + \alpha(\mathbf{D}_X^T \mathbf{D}_X + \mathbf{D}_Y^T \mathbf{D}_Y))^{-1} \mathbf{W}^T \quad (2.30)$$

$$\hat{\mathbf{x}} = \Pi \mathbf{y} \quad (2.31)$$

Since the transformation does not depend on instantaneous measurements, it can be pre-calculated, and then applied for various measurements for fast image reconstruction. This is very appealing for realtime RTI systems that require frequent image updates [45], [56].

The total number of multiplications N_{mult} required to transform the measurements into the image is the total number of voxels N times the number of unique links M in the network

$$N_{mult} = NM = \frac{N(K^2 - K)}{2} \quad (2.32)$$

where K is the number of nodes in the network. We see that complexity increases linearly as the number of voxels increases, and quadratically as the number of nodes in the network increases.

2.6 Experimental Results

2.6.1 Physical Description of Experiment

A wireless peer-to-peer network containing 28 nodes is deployed for the purpose of testing the capability of RTI to image changed attenuation. Each node is placed three feet apart along the perimeter of a 21x21 foot square, surrounding a total area of 441 square feet. The network is deployed on a grassy area approximately 15 feet away from the Merrill Engineering Building at the University of Utah. Each radio is placed on a stand at three feet off the ground.

The area surrounded by the nodes contains two trees with a circumference of approximately three feet. The network is intentionally placed around the trees so that static objects exist in the tested RTI system. RTI should only image attenuation that has changed from the time of calibration within the deployment area. Markers are measured and placed in 35 locations within the network so that the humans' locations are known and can be utilized in the subsequent error analysis. A map and photo of the experiment are shown in Fig. 2.9.

The network is comprised of TelosB wireless nodes made by Crossbow. Each node operates in the 2.4GHz frequency band, and uses the IEEE 802.15.4 standard for communication. A base station node listens to all network traffic, then feeds the data to a laptop computer via a USB port for the processing of the images. Since the base station node is within range of all nodes, the latency of measurement retrieval to the laptop is low, on the order of a few milliseconds. If a multi-hop RTI network were to be deployed, this latency would certainly increase.

To avoid network transmission collisions, a simple token passing protocol is used. Each node is assigned an ID number and programmed with a known order of transmission. When a node transmits, each node that receives the transmission examines the sender identification number. The receiving nodes check to see if it is their turn to transmit, and if not, they wait for the next node to transmit. If the next node does not transmit, or the packet is corrupted, a timeout causes each receiver to move to the next node in the schedule so that the cycle is not halted.

At the arrival of each packet to the laptop, the RTI program running on the laptop updates a link RSS measurement vector. At each update, the base station hears from only one node in the network, so only RSS values on links involving that particular node are updated. Each link's RSS measurement is an average of the two directional links from i to j and j to i .

In this experiment, the system is calibrated by taking RSS measurements while the network is vacant from moving objects. The RSS vector is averaged over a 30 second period, which results in approximately 100 RSS samples from each link. The calibration RSS vector provides a baseline against which all other RSS measurements are differenced, as discussed in Section 2.3. Other methods of calibration could be used in situations where it is impossible to keep the network vacant from moving objects. For example, a single past measurement or a sliding window average of RSS measurement history could be used as the baseline.

2.6.2 Effect of Human Obstruction

Since RTI is based on the assumption that objects shadow individual links in a wireless network, it is helpful to examine the effect of obstructions on a single link. In Fig. 2.10, a human stands at position (9,9) and RSS measurements for

each link are collected. These measurements are compared with the calibration measurements that were taken when the network was vacant.

The top plot in Fig. 2.10 shows that a significant decrease in RSS, anywhere from 5 to 10 dB, is experienced by link (0,18) to (18,0) as it travels through the obstruction. The middle plot shows that even though the link (9,0) to (9,21) passes through the tree, it still experiences significant loss when the human is present on the LOS path. The bottom plot in the figure shows an example of a link that does not pass through the obstruction, resulting in very little difference in RSS.

In environments where links travel over long distances, or when many objects block the direct LOS path, we expect the effect of a human obstruction to be lessened. In those cases, certain links may experience losses, while others may not. Future research will investigate the effect of human obstruction on a link's RSS when a link passes through walls or other major static obstructions. This will be essential in making the technology practical for the future applications of RTI as previously discussed.

2.6.3 Cylindrical Human Model

To assess the accuracy of RTI images, one must first know or assume the “true” attenuation field that is being estimated. Since imaging the location of humans is the primary goal of RTI, a model for the size, shape, and attenuation of the human body at the frequencies of interest would be required. This information is difficult to model, since it is dependent on body types, the plane of intersection, and other variables.

For simplicity, a human is modeled as a uniformly attenuating cylinder with radius R_H . In this case, the “true” image \mathbf{x}_c for a human positioned at location c_H can be described as

$$\mathbf{x}_{cj} = \begin{cases} 1 & \text{if } \|\mathbf{x}_j - c_H\| < R_H \\ 0 & \text{otherwise} \end{cases} \quad (2.33)$$

where \mathbf{x}_{cj} is the center location of voxel j .

By scaling the image such that the maximum equals one, resulting in the normalized image $\hat{\mathbf{x}}_N$, we can define the mean-squared error of the normalized image to be

$$\epsilon = \frac{\|\mathbf{x}_c - \hat{\mathbf{x}}_N\|^2}{N} \quad (2.34)$$

where N is the number of voxels in the image.

2.6.4 Example Images

Using the model and reconstruction algorithms described in Sections 2.3 and 2.5, we present some typical image results for humans standing inside the experimental RTI network. A human stands at coordinate (9,9) and RSS data are measured for a few seconds. The data are averaged for 10 samples per link, and this measurement differenced with the calibration data taken while the network is vacant. Figures 2.11 and 2.12 display both the “true” attenuation based on the cylindrical model, and the RTI reconstruction using H1 regularization with the parameters listed in Table 2.3.

Using the cylindrical human model with a radius of $R_H = 1.3$, the squared error for the single-human image standing at (9,9) was measured to be $\epsilon = .021$. The squared error for the two-person image was measured to be $\epsilon = .036$. These error values are in general agreement with the bounds derived in Section 2.4.

There are many areas in the images of Figs. 2.11 and 2.12 where estimated attenuation is above zero, even where no obstruction exists. This is due to the fact that a human not only attenuates a wireless signal, it reflects and scatters it. The simple LOS model used in this paper does not take into account the changes in RSS values due to multipath caused by the obstructions being imaged. For example, a link may be bouncing off the human and destructively interfering with itself on a path that does not cross through the obstruction, thus leading to error in the estimated attenuation. Future research will seek to refine the weighting model used in RTI such that this modeling error is lessened.

2.6.5 Effect of Parameters on Image Accuracy

The weighting and regularization parameters play an important role in generating accurate RTI images. If the problem is regularized too strongly, the resultant images may be too smooth to provide a good indication of obstruction boundaries. If the regularization parameter is set too low, noise may corrupt the results, making it difficult to know if a bright spot is an obstruction or noise.

Another parameter effecting the accuracy of an image is the width of the weighting ellipse. If the ellipse is too wide, the detail of where attenuation is occurring

within the network may be obscured. If the ellipse is too narrow, voxels that do in fact attenuate a link's signal may not be captured by the model. This may result in a loss of information that degrades the final image quality.

In this paper, we empirically identify the parameters that provide the most accurate images using the cylindrical human model. For each parameter, images are formed from data measured while a human is standing at one of the known positions, as indicated in Fig. 2.9(a). Such an image is formed for each of the possible human positions shown in Fig. 2.9(a). The squared error is calculated for each image, and averaged over the entire set. This is performed for a varying regularization parameter, while the weighting ellipse parameter is held constant at $\lambda = .1$. Then, it is repeated for varying ellipse parameters while holding the regularization constant at $\alpha = 4.5$. The resultant error curves are shown in Fig. 2.13.

The curves shown in Fig. 2.13 show that the choice of regularization and weighting parameters is important in obtaining accurate images. Future research possibly will explore the automatic calculation and adjustment of these parameters. It should be noted that the error curves and optimal values presented are dependent upon the pixel size used in generating the images. The general shape of the curves, however, is similar for different pixel sizes. In this study, pixel size is held constant at .5 feet for all experiments.

2.7 Conclusion

Radio tomographic imaging is a new and exciting method for imaging the attenuation of physical objects with wireless networks operating at RF wavelengths. This paper discusses a basic model and image reconstruction technique that has low computational complexity. Experimental results show that RTI is capable of imaging the RF attenuation caused by humans in dense wireless networks with inexpensive and standard hardware.

Future research will be important to make RTI realistic in security, rescue, military, and other commercial applications. First, new models and experiments must be developed for through-wall imaging. In this case, the shadowing and fading caused by many objects in the environment may cause the LOS weighting model

to be inaccurate. New and possibly adaptive weighting models will need to be investigated and tested.

Wireless protocols, customized hardware, and signal design are also important for improving RTI. Protocols that are capable of delivering low-latency RSS information for large networks will be essential when deploying the technology over large areas. Antennas that direct the RF energy through an area may reduce the effects of multipath and increase the effect of human presence on signal strength. Custom signals, perhaps taking advantage of frequency diversity may improve the quality of RTI results.

Radio tomographic imaging may provide a low-cost and flexible alternative to existing technologies like ultra-wideband radar. This would enable many applications in the areas of security, search and rescue, police/military, and others.

Table 2.1. Gaussian-Mixture Noise Model Parameters Estimated From Measurements

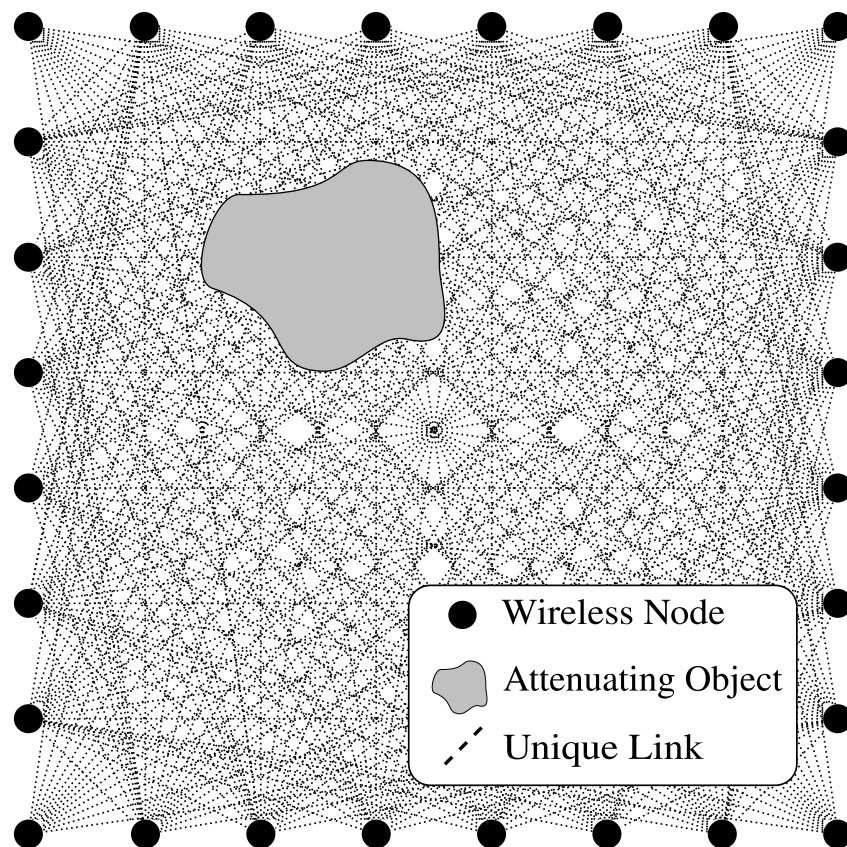
Parameter	Value
σ_1	0.971
σ_2	3.003
p_1	0.548
p_2	0.452

Table 2.2. Reconstruction parameters used to generate MSE bound surfaces.

Parameter	Value	Description
Δ_p	.1	Pixel width (m)
λ	.007	Width of weighting ellipse in (2.9) (m)
δ_c	1.3	Pixel correlation constant in (2.20) (m)
σ_x^2	.1	Pixel variance in (2.20) $(dB)^2$
γ	.5483	Bound parameter in (2.19)

Table 2.3. Image reconstruction parameters

Parameter	Value	Description
Δ_p	.5	Pixel width (feet)
λ	.01	Width of weighting ellipse (feet)
α	5	Regularization parameter
R_H	1.3	Human radius for cylindrical model (feet)

**Figure 2.1.** An illustration of an RTI network. Each node broadcasts to the others, creating many projections that can be used to reconstruct an image of objects inside the network area.

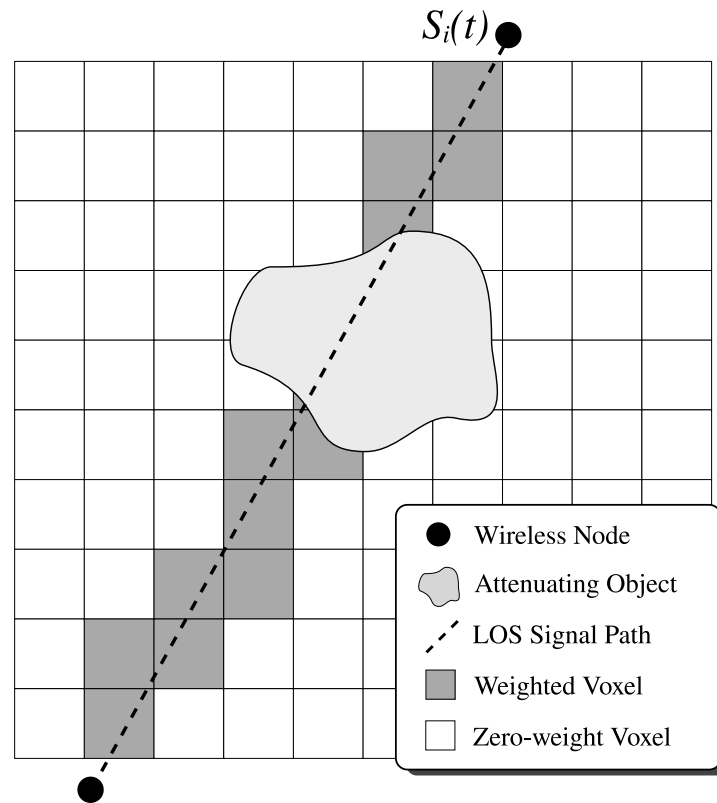
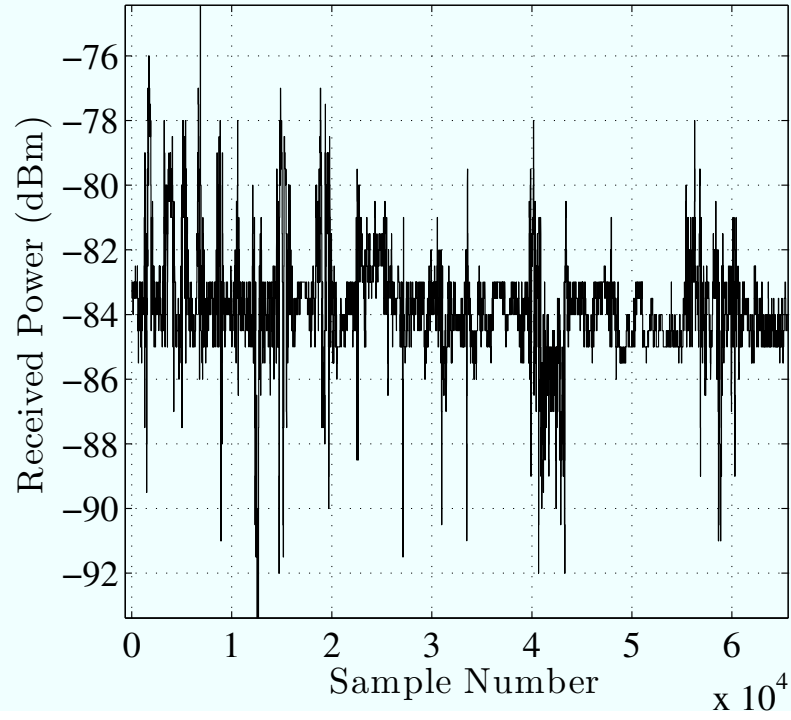
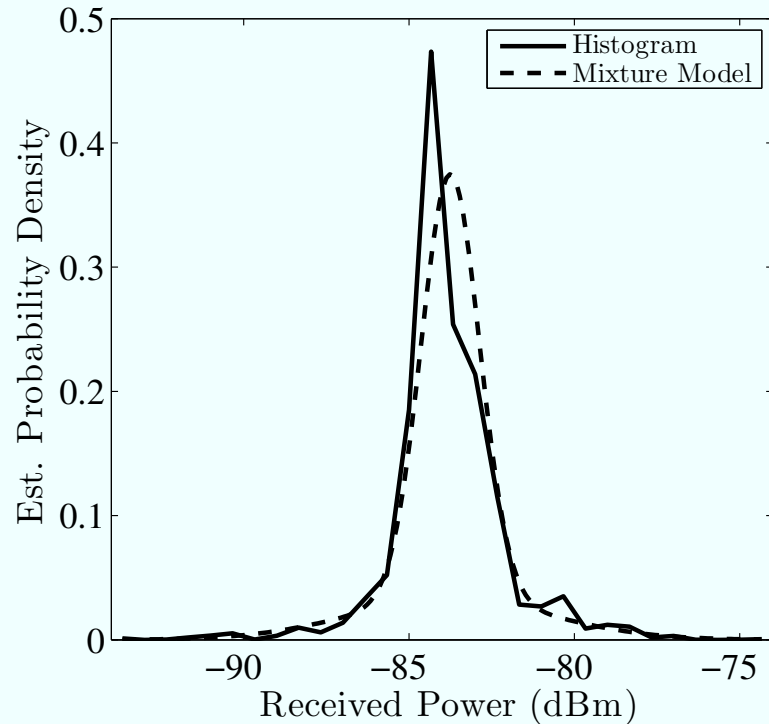


Figure 2.2. An illustration of a single link in an RTI network that travels in a direct LOS path. The signal is shadowed by objects as it crosses the area of the network in a particular path. The darkened voxels represent the image areas that have a nonzero weighting for this particular link.

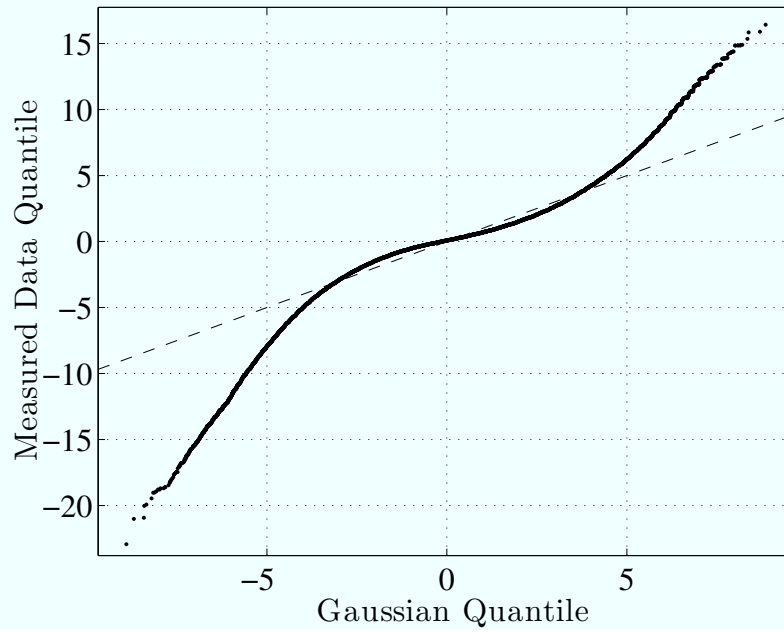


(a) Time plot

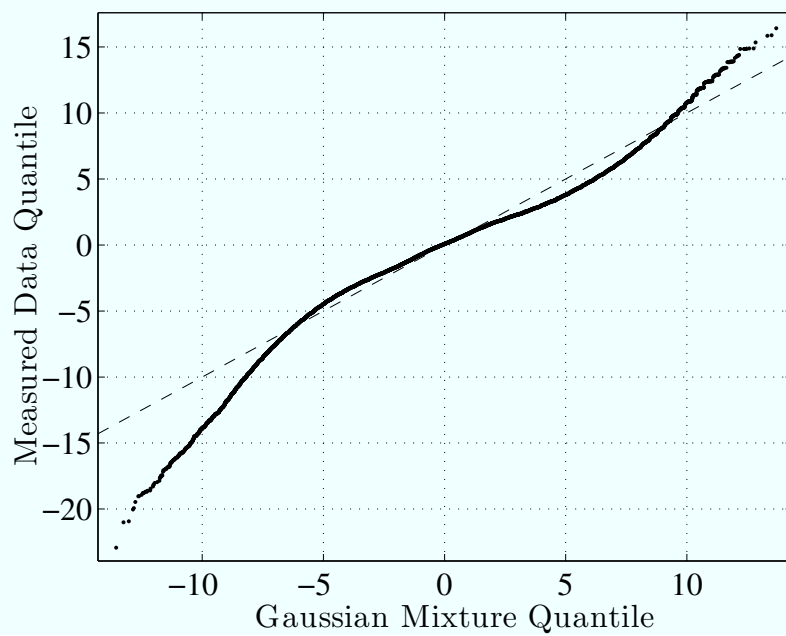


(b) Histogram

Figure 2.3. Temporal fading on link (3, 20) during nonobstructing motion, showing (a) time plot and (b) histogram.

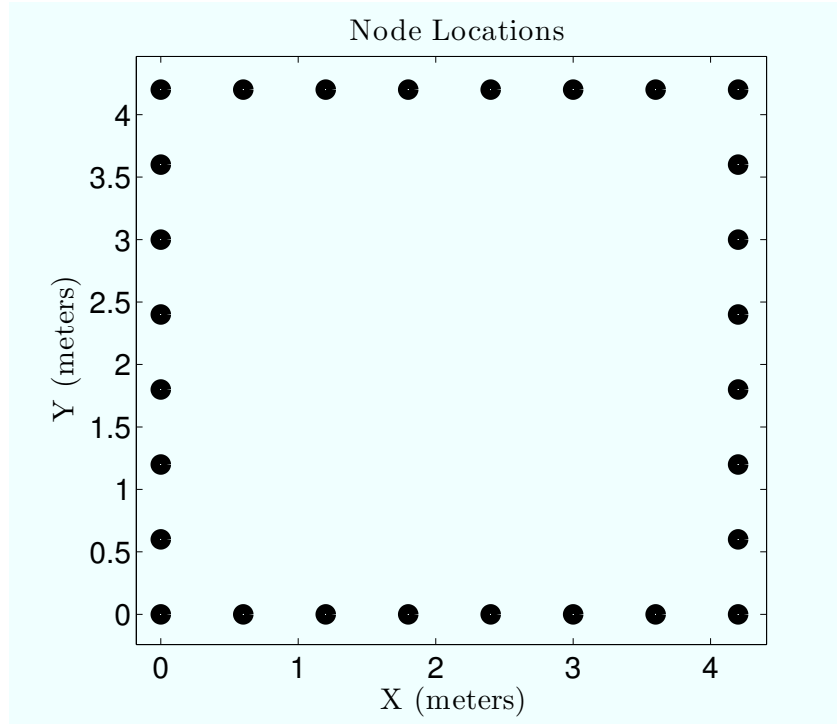


(a) Gaussian Model

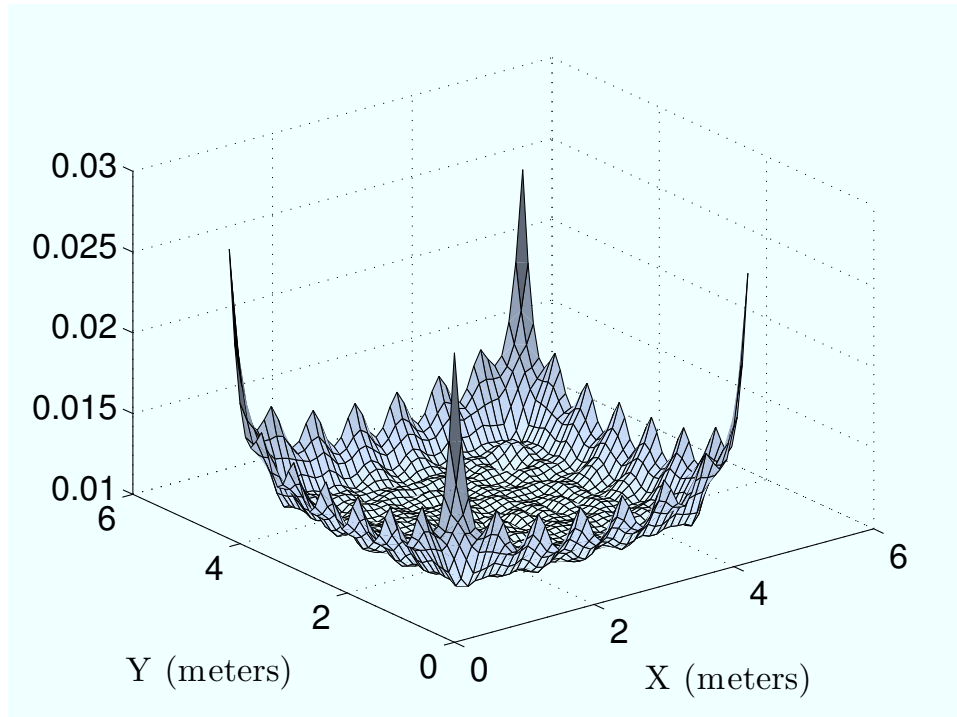


(b) Mixture Model

Figure 2.4. Quantile-quantile plots comparing measured RSS data with Gaussian and Mixture distributions.

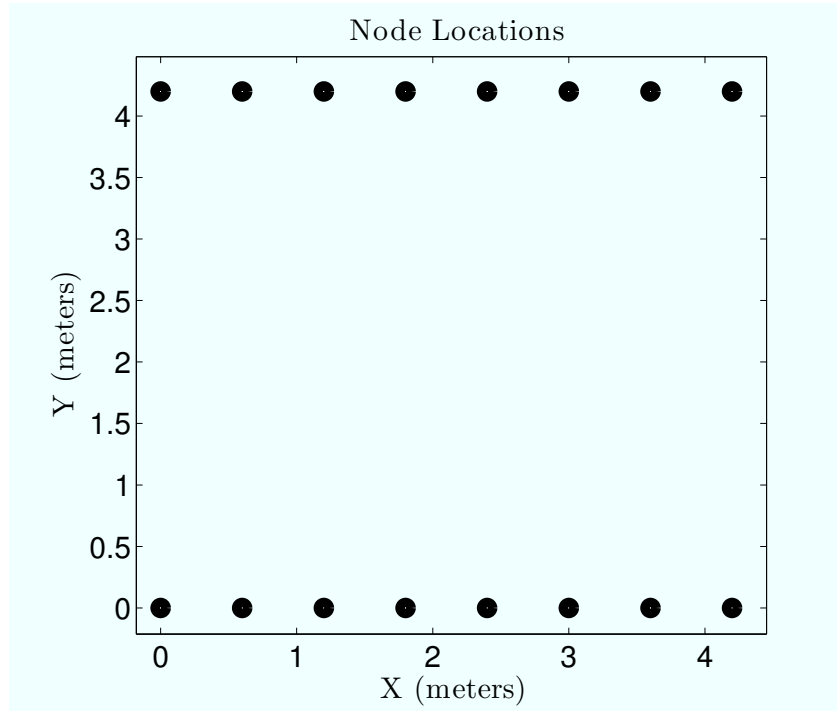


(a) 28 nodes located in a square perimeter, 8 on each side.

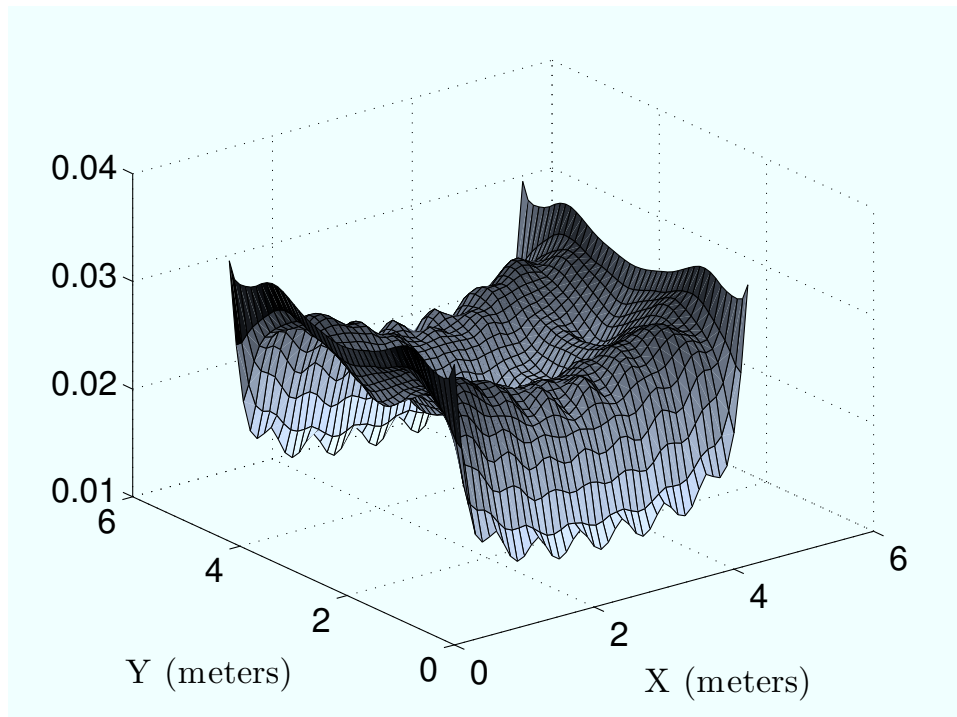


(b) The MSE bound for the node locations shown in Fig. 2.5(a).

Figure 2.5. MSE bound surface plots for a square network.

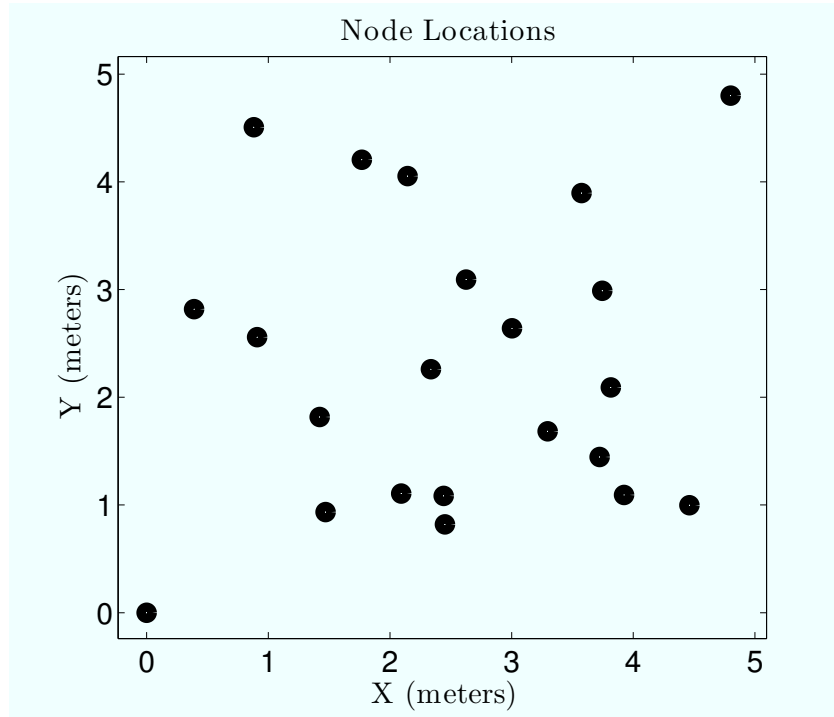


(a) 16 nodes located in a front-back setup, 8 on each side.

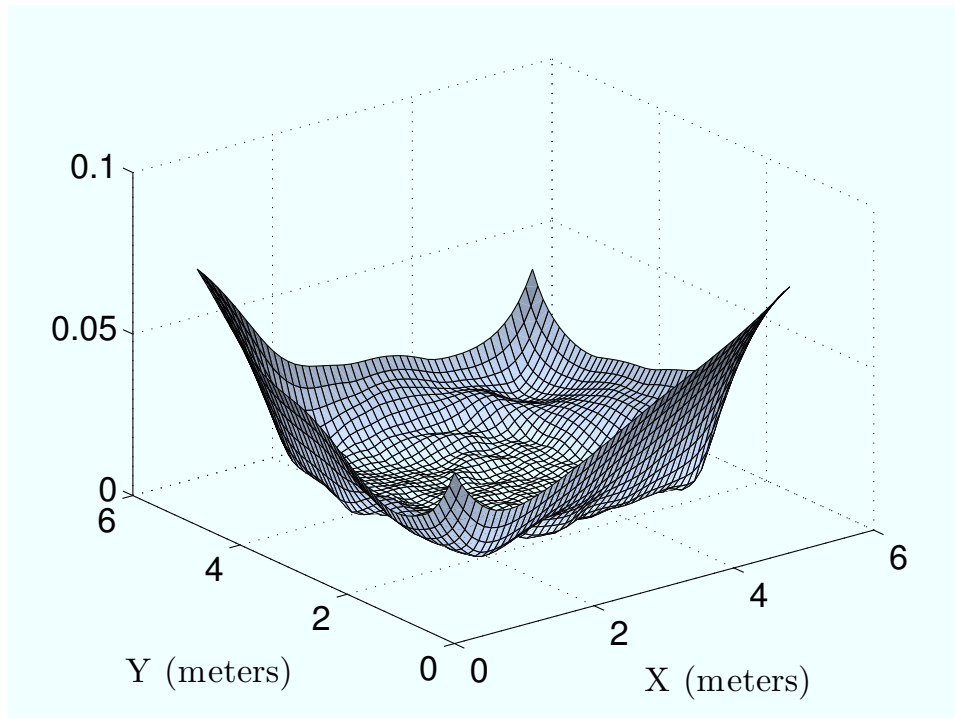


(b) The MSE bound for the node locations shown in Fig. 2.6(a).

Figure 2.6. MSE bound surface plots for a front-back network.



(a) 22 nodes located randomly in a square area.



(b) The MSE bound for the node locations shown in Fig. 2.7(a).

Figure 2.7. MSE bound surface plots for random node locations.

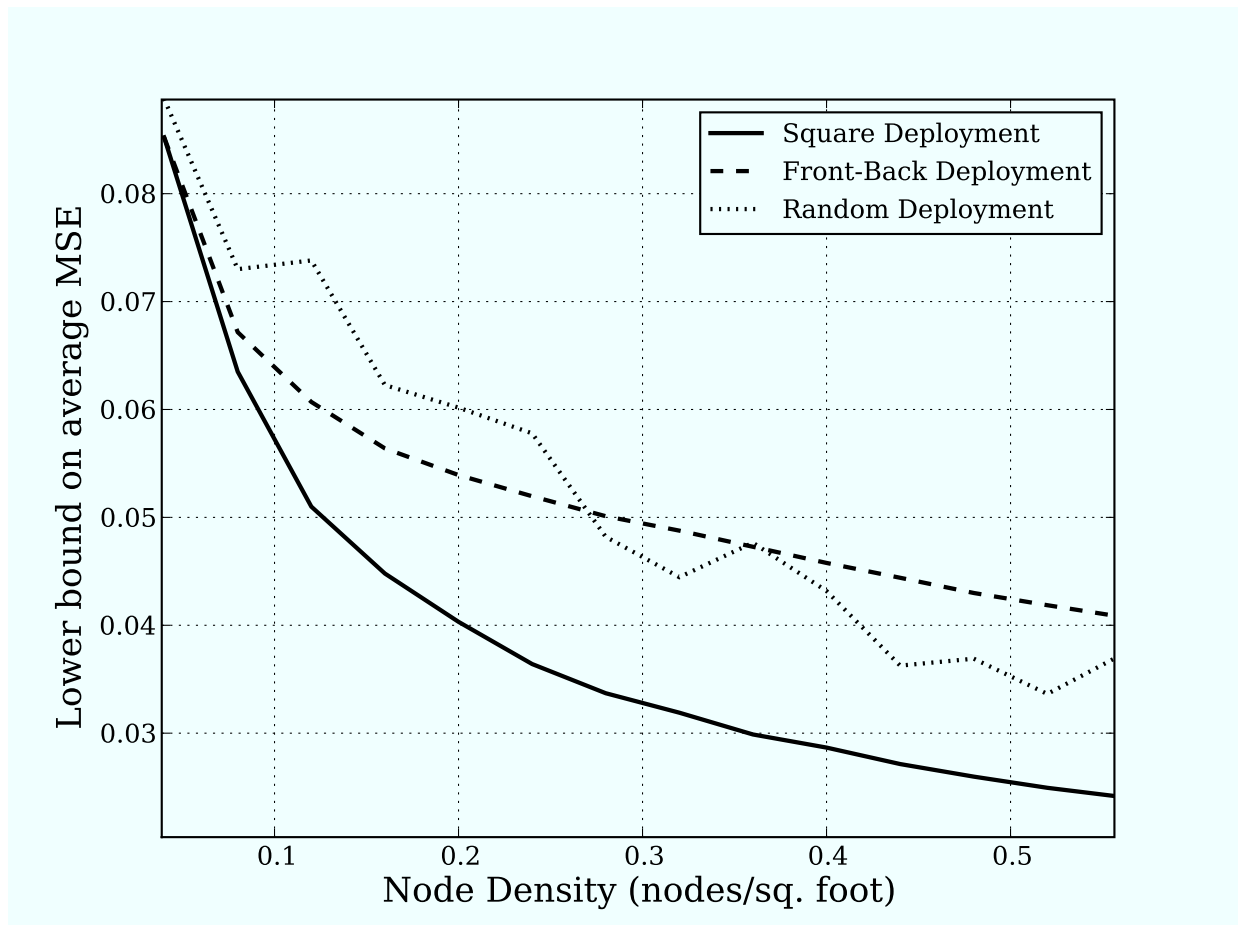
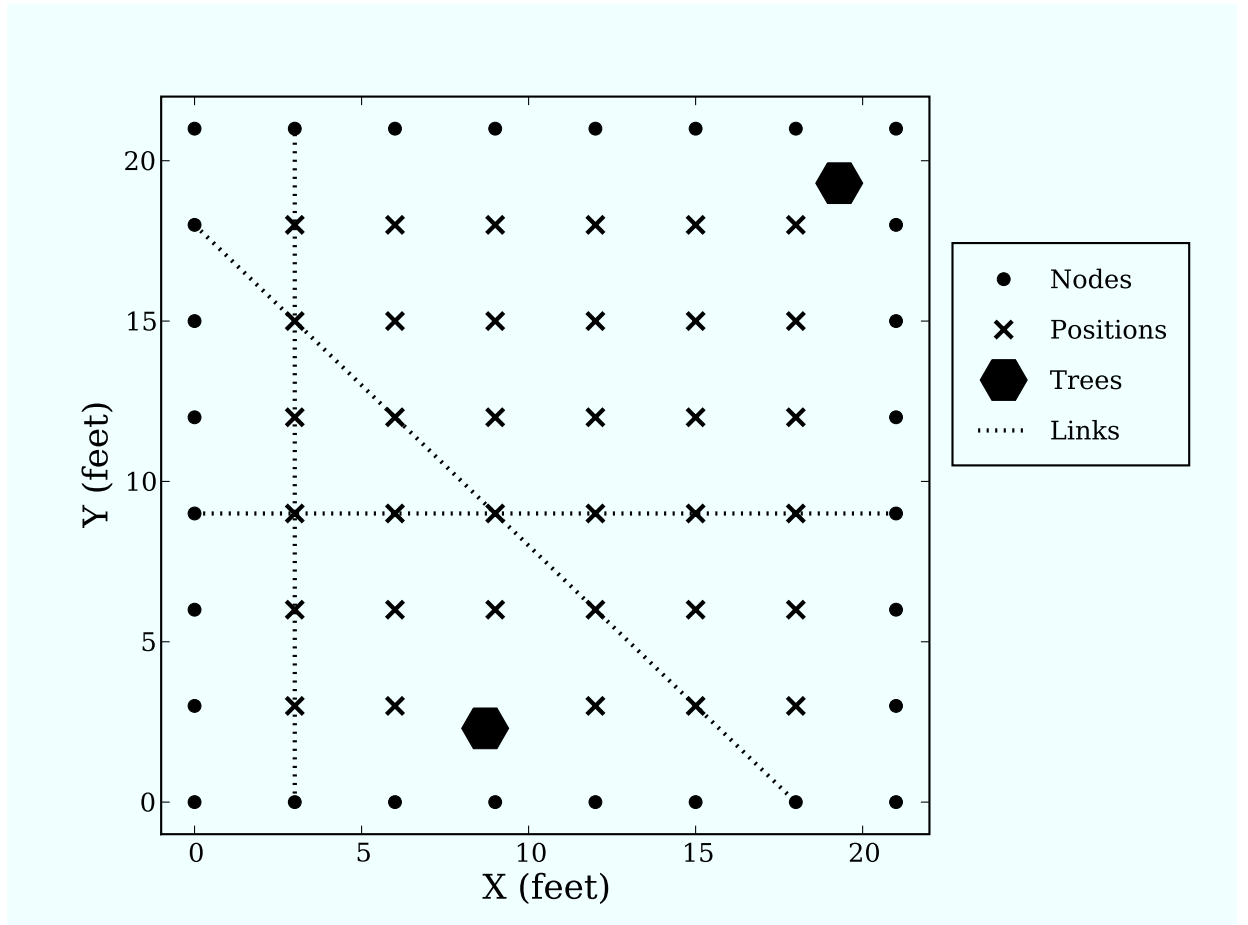
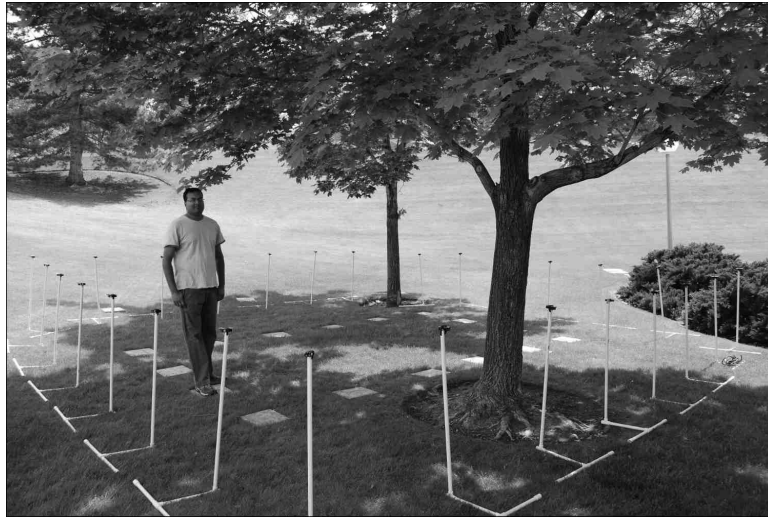


Figure 2.8. The lower bound on average MSE vs. node density for three RTI network geometries.



(a) Map



(b) Photo

Figure 2.9. The network geometry and links that correspond to Fig. 2.10 are illustrated in (a). (b) is a photo of the deployed network with an experimenter standing at location (3,9).

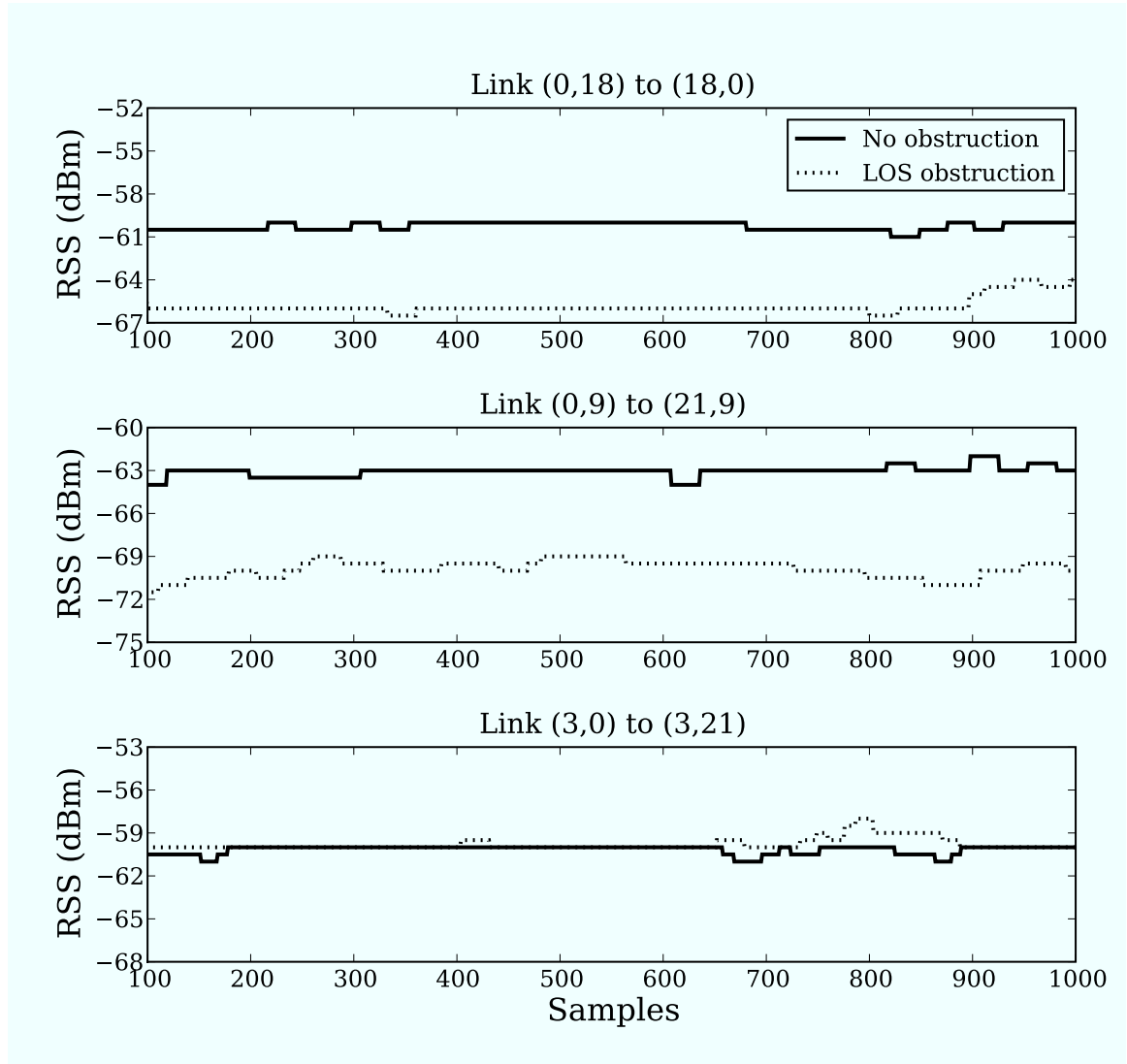
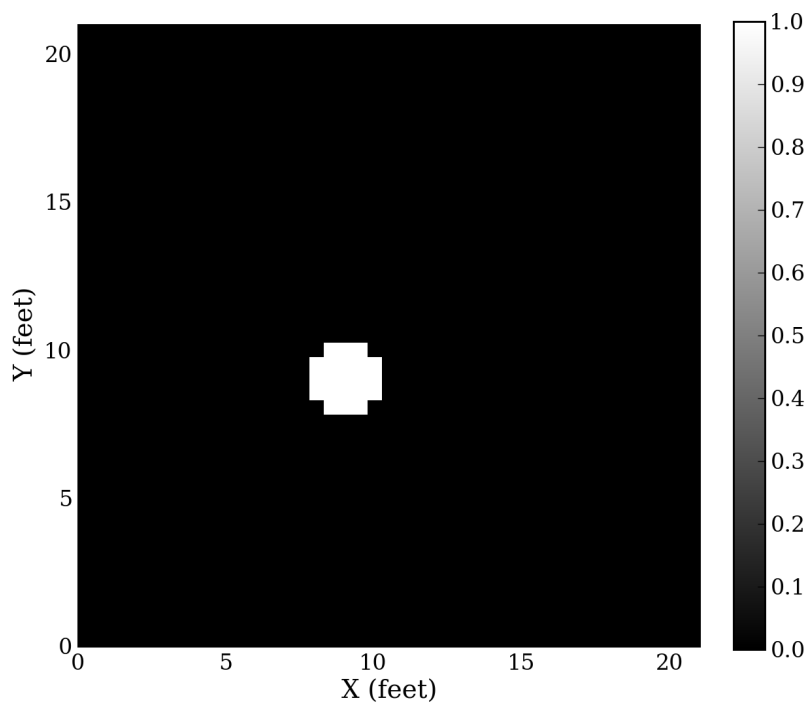
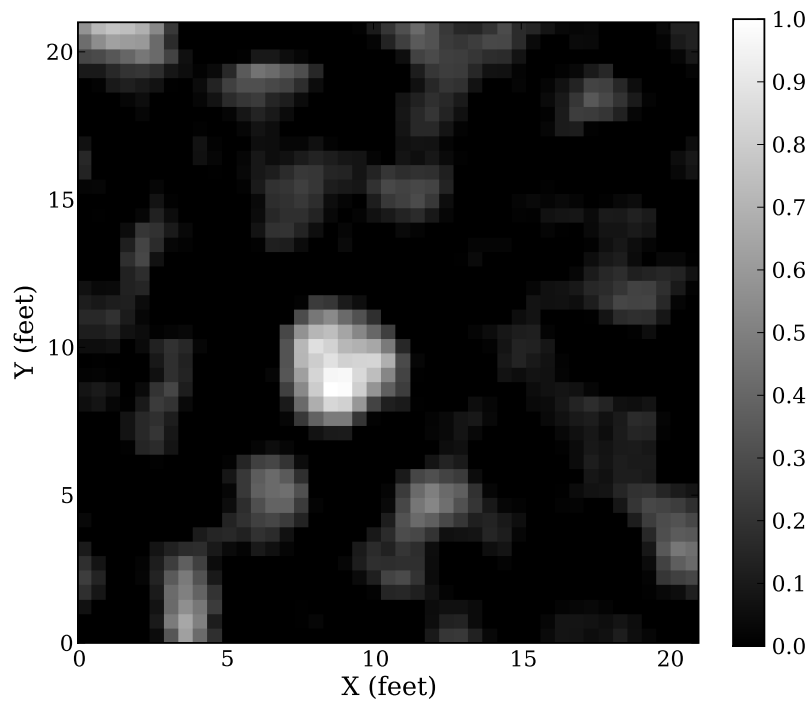


Figure 2.10. A comparison of the effect of human obstruction on three links. In the unobstructed case, the network is vacant from human experimenters. In the obstructed case, a human stands at coordinate (9,9).

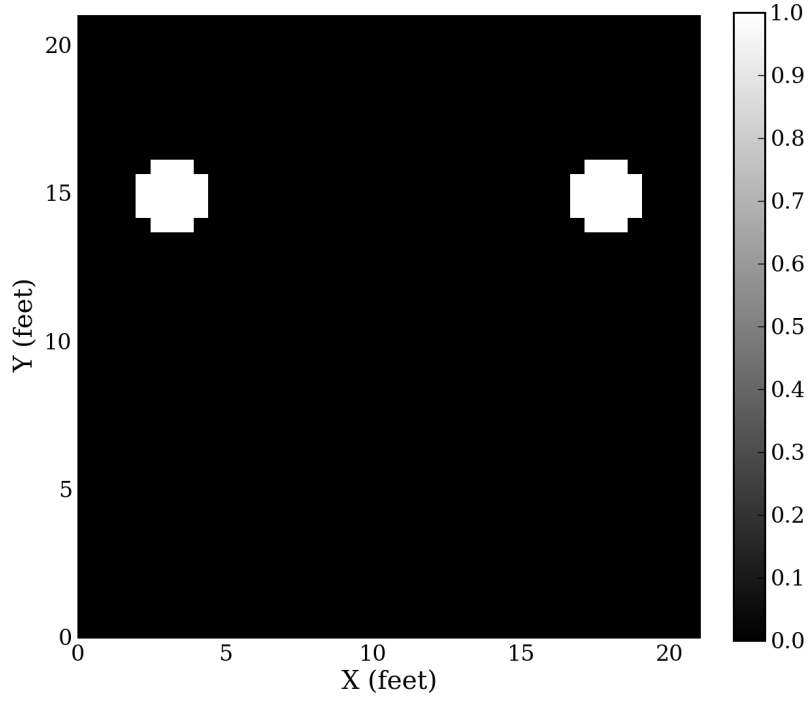


(a) Cylindrical model image

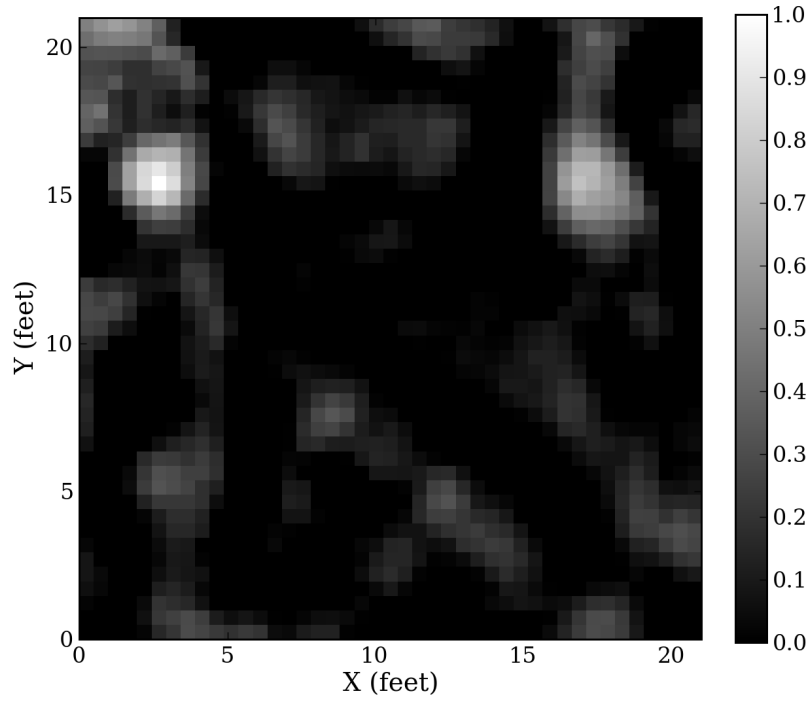


(b) RTI result

Figure 2.11. RTI results for a single human standing at coordinate (9,9). The person is modeled as a uniformly attenuating cylinder of radius $R_H = 1.3$ feet.



(a) Cylindrical model image



(b) RTI result

Figure 2.12. RTI results for a two humans standing at coordinates (3,15) and (18,15). Each person is modeled as a uniformly attenuating cylinder of radius $R_H = 1.3$ feet.

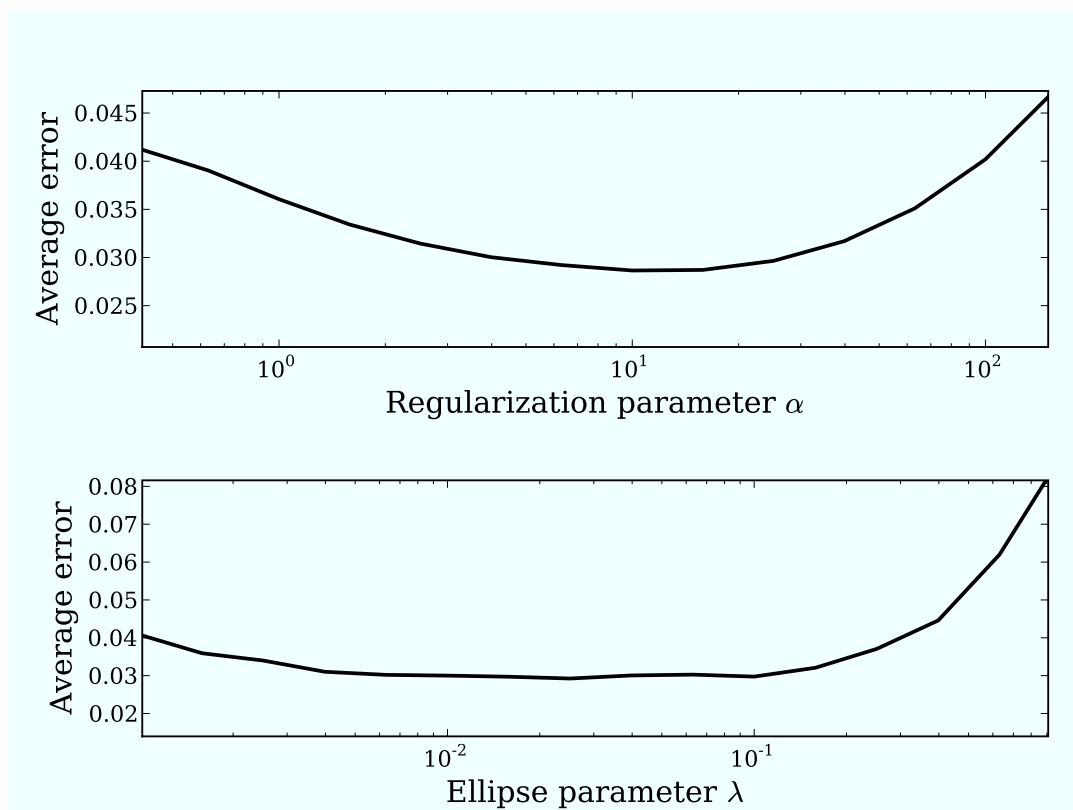


Figure 2.13. Error vs. parameter curves. In the first plot, the weighting ellipse width parameter is held constant at $\lambda = .1$ while the regularization parameter α is varied. In the second, $\alpha = 4.5$ and the width of the weighting ellipse is varied.

CHAPTER 3

REGULARIZATION METHODS FOR RADIO TOMOGRAPHIC IMAGING

3.1 Abstract

Radio Tomographic Imaging (RTI) is an emerging technology that uses received signal strength measurements to image the attenuation of objects within a wireless network area. RTI is by nature an ill-posed inverse problem, therefore, regularization techniques must be utilized to obtain accurate images. This paper discusses some common regularization techniques, including Tikhonov, truncated singular value decomposition, and total variation, and presents the results of applying them to RTI.

3.2 Introduction

Radio Tomographic Imaging (RTI) is a method for imaging the attenuation of physical objects within areas surrounded by wireless radios. RTI uses received signal strength (RSS) measurements that traverse the network area to reconstruct an image of where the signals are being attenuated (see Fig. 3.1). Previous work developed a linear model relating the attenuation field to signal strength measurements, and derived error bounds for resultant images [45], [56]. The formulation for RTI is by nature an ill-posed inverse problem, and regularization must be applied to obtain accurate images. This paper focuses on a few common regularization techniques¹, and presents the results of applying them to RTI.

RTI has applications in emergencies, rescue operations, and security breaches, since the objects being imaged need not carry an electronic device. RF signals can travel through obstructions such as walls, trees, and smoke, while optical or

¹This chapter first appeared in J. Wilson and N. Patwari, “Regularization Methods for Radio Tomographic Imaging”, Virginia Tech Wireless Symposium, 2009.

infrared imaging systems cannot. RF imaging will also work in the dark, where video cameras will fail. Even for applications where video cameras *could* work, privacy concerns may prevent their deployment. An RTI system provides current images of the location of people and their movements, but cannot be used to identify a person.

One main application of RTI is to reduce injury for correctional and law enforcement officers; many are injured each year because they lack the ability to detect and track offenders through building walls [34]. By showing the locations of people within a building during hostage situations, building fires, or other emergencies, RTI can help law enforcement and emergency responders to know where they should focus their attention.

Another application is in automatic monitoring and control in “smart” homes and buildings. Some building control systems detect motion in a room and use it to control lighting, heating, air conditioning, and even noise cancellation. RTI systems can further determine how many people are in a room and where they are located, providing more precise control.

Generally RTI has application in security and monitoring systems for indoor and outdoor areas. For example, most existing security systems are trip-wire based or camera-based. Trip-wire systems detect when a person crosses a boundary, but do not track the person when they are within the area. Cameras are ineffective in the dark and have limited view angles. An RTI system could serve both as a trip-wire, alerting when intruders enter into an area, and tracking where are at all times while they are inside, regardless of availability of lighting or obstructions.

The reduction in costs for radio frequency integrated circuits (RFICs) and advances in peer-to-peer data networking have made realistic the use of hundreds or thousands of simple radio devices in a single RTI deployment. Since the relative cost of such devices is low, large RTI networks are possible in applications that may be otherwise impractical.

3.3 Related Work

RF-based imaging has been dominated in the commercial realm by ultra-wideband (UWB) based through-the-wall (TTW) imaging devices from companies like Time

Domain, Cambridge Consultants, and Camero Tech. These companies have developed products using a phased array of radars that transmit UWB pulses and then measure echoes to estimate a range and bearing. These devices are accurate close to the device, but inherently suffer from accuracy and noise issues at long range due to monostatic radar scattering losses and large bandwidths. Some initial attempts [39] allow 2-4 of these high-complexity devices to collaborate to improve coverage.

To emphasize the small required bandwidth compared to UWB, some relevant research is being called “ultra-narrowband” (UNB) radar [40–42]. These systems propose using narrowband transmitters and receivers deployed around an area to image the environment within that area. Measurements are phase-synchronous at the multiple nodes around the area. Such techniques have been applied to detect and locate objects buried under ground using what is effectively a synthetic aperture array of ground-penetrating radars [43]. Experiments have been reported which measure a static environment while moving one transmitter or one receiver [42], and measure a static object on a rotating table in an anechoic chamber in order to simulate an array of transmitters and receivers at many different angles [40, 42, 43]. Because in this paper we use low complexity, noncoherent sensors, we can deploy many sensors and image in real time, enabling the study of tracking moving objects. We present experimental results with many devices in real-world, cluttered environments.

Multiple-input-multiple-output (MIMO) radar is another emerging field that takes advantage of multiple transmitters and receivers to locate objects within a spatial area [44]. In this framework, signals are transmitted into the area of interest, objects scatter the signal, and the reflections are measured at each receiver. The scattering objects create a channel matrix which is comparable to the channel matrix in traditional MIMO communication theory. RTI differs from MIMO radar in the same way that it differs from traditional radar. Instead of measuring reflections, RTI uses the shadowing caused by objects as a basis for image reconstruction.

Recent research has also used measurements of signal strength on 802.11 WiFi links to detect and locate a person’s location. Experiments in [13] demonstrate the capability of a detector based on the change in signal strength variance to detect and to identify which of four positions a person is located. Our approach is not

based on point-wise detection. Instead, we use tomographic methods to estimate an image of the change in the attenuation as a function of space.

3.4 Linear Formulation

When wireless nodes communicate, the radio signals pass through the physical area of the network. Objects within the area absorb, reflect, diffract, or scatter some of the transmitted power. The goal of an RTI system is to determine an image vector of dimension \mathbb{R}^N that describes the amount radio power attenuation occurring due to physical objects within N voxels of a network region. Since voxels locations are known, RTI allows one to know where attenuation in a network is occurring, and therefore, where objects are located.

If K is the number of nodes in the RTI network, then the total number of unique two-way links is $M = \frac{K^2-K}{2}$. Any pair of nodes is counted as a link, whether or not communication actually occurs between them. The signal strength $y_i(t)$ of a particular link i at time t is dependent on:

- P_i : Transmitted power in dB.
- $S_i(t)$: Shadowing loss in dB due to objects that attenuate the signal.
- $F_i(t)$: Fading loss in dB that occurs from constructive and destructive interference of narrow-band signals in multipath environments.
- L_i : Static losses in dB due to distance, antenna patterns, device inconsistencies, etc.
- $\nu_i(t)$: Measurement noise and modeling error.

Mathematically, the received signal strength is described as

$$y_i(t) = P_i - L_i - S_i(t) - F_i(t) - \nu_i(t) \quad (3.1)$$

The shadowing loss $S_i(t)$ can be approximated as a sum of attenuation that occurs in each voxel. Since the contribution of each voxel to the attenuation of

a link is different for each link, a weighting is applied. Mathematically, this is described for a single link as

$$S_i(t) = \sum_{j=1}^N w_{ij} x_j(t). \quad (3.2)$$

where $x_j(t)$ is the attenuation occurring in voxel j at time t , and w_{ij} is the weighting of pixel j for link i . If a link does not “cross” a particular voxel, that voxel is removed by using a weight of zero. For example, Fig. 3.2 is an illustration of how a direct LOS link might be weighted in a nonscattering environment. In Section 3.4, an ellipse is used as a simple mechanism to determine LOS weighting.

Imaging only the *changing* attenuation greatly simplifies the problem, since all static losses can be removed over time. The change in RSS Δy_i from time t_a to t_b is

$$\begin{aligned} \Delta y_i &\equiv y_i(t_b) - y_i(t_a) \\ &= S_i(t_b) - S_i(t_a) + F_i(t_b) - F_i(t_a) \\ &\quad + \nu_i(t_b) - \nu_i(t_a), \end{aligned} \quad (3.3)$$

which can be written as

$$\Delta y_i = \sum_{j=1}^N w_{ij} \Delta x_j + n_i, \quad (3.4)$$

where the noise is the grouping of fading and measurement noise

$$n_i = F_i(t_b) - F_i(t_a) + \nu_i(t_b) - \nu_i(t_a) \quad (3.5)$$

and

$$\Delta x_j = x_j(t_b) - x_j(t_a) \quad (3.6)$$

is the difference in attenuation at pixel j from time t_a to t_b .

If all links in the network are considered simultaneously, the system of RSS equations can be described in matrix form as

$$\Delta \mathbf{y} = \mathbf{W} \Delta \mathbf{x} + \mathbf{n} \quad (3.7)$$

where

$$\Delta \mathbf{y} = [\Delta y_1, \Delta y_2, \dots, \Delta y_M]^T$$

$$\begin{aligned}
\Delta \mathbf{x} &= [\Delta x_1, \Delta x_2, \dots, \Delta x_N]^T \\
\mathbf{n} &= [n_1, n_2, \dots, n_M]^T \\
[\mathbf{W}]_{i,j} &= w_{ij}
\end{aligned} \tag{3.8}$$

In summary, $\Delta \mathbf{y}$ is the vector of length M all link difference RSS measurements, \mathbf{n} is a noise vector, and $\Delta \mathbf{x}$ is the attenuation image to be estimated. \mathbf{W} is the weighting matrix of dimension $M \times N$, with each column representing a single voxel, and each row describing the weighting of each voxel for that particular link. Each variable is measured in decibels (dB).

To simplify the notation used throughout the rest of this paper, \mathbf{x} and \mathbf{y} are used in place of $\Delta \mathbf{x}$ and $\Delta \mathbf{y}$, respectively.

Normalized Elliptical Weight Model

If knowledge of an environment were available, one could estimate the weights $\{w_{ij}\}_j$ for link i which reflected the spatial extent of multiple paths between transmitter and receiver. Perhaps calibration measurements could aid in estimation of the linear transformation \mathbf{W} . However, with no site-specific information, we require a statistical model that describes the linear effect of the attenuation field on the path loss for each link.

An ellipse with foci at each node location can be used as a method for determining the weighting for each link in the network [45], [56]. If a particular pixel falls inside the ellipse, it is weighted, while all pixels outside the ellipse have a weight of zero. Additionally, the weight for each pixel is normalized by the link length [46]. The weighting is described mathematically as

$$w_{ij} = \frac{1}{\sqrt{d}} \begin{cases} 1 & \text{if } d_{ij}(1) + d_{ij}(2) < d + \lambda \\ 0 & \text{otherwise} \end{cases} \tag{3.9}$$

where d is the distance between the two nodes, $d_{ij}(1)$ and $d_{ij}(2)$ are the distances from the center of voxel j to the two node locations for link i , and λ is a tunable parameter describing the width of the ellipse.

3.5 Regularization

Linear models for many physical problems, including RTI, take the form of

$$\mathbf{y} = \mathbf{W}\mathbf{x} + \mathbf{n} \tag{3.10}$$

where $\mathbf{y} \in \mathbb{R}^M$ is measured data, $\mathbf{W} \in \mathbb{R}^{M \times N}$ is a transfer matrix of the model parameters $\mathbf{x} \in \mathbb{R}^N$, and $\mathbf{n} \in \mathbb{R}^M$ is a measurement noise vector. When estimating an image from measurement data, it is common to search for a solution that is optimal in the least-squared-error sense.

$$\mathbf{x}_{LS} = \arg \min_{\mathbf{x}} \|\mathbf{W}\mathbf{x} - \mathbf{y}\|_2^2 \quad (3.11)$$

In other words, the least-squares solution minimizes the noise energy required to fit the measured data to the model. The least-square solution can be obtained by setting the gradient of (3.11) equal to zero, resulting in

$$\mathbf{x}_{LS} = (\mathbf{W}^T \mathbf{W})^{-1} \mathbf{W}^T \mathbf{y} \quad (3.12)$$

which is only valid if \mathbf{W} is full-rank. This is not the case in an RTI system.

RTI is an ill-posed inverse problem, meaning that small amounts of noise in measurement data are amplified to the extent that results are meaningless. This is due to very small singular values in the transfer matrix \mathbf{W} that cause certain spectral components to grow out of control upon inversion. To see this, \mathbf{W} is replaced by its singular value decomposition (SVD):

$$\mathbf{W} = \mathbf{U} \Sigma \mathbf{V}^T \quad (3.13)$$

where \mathbf{U} and \mathbf{V} are unitary matrices, and Σ is a diagonal matrix of singular values. Plugging (3.13) into (3.12), the least squares solution can be written as

$$\mathbf{x}_{LS} = \mathbf{V} \Sigma^{-1} \mathbf{U}^T \mathbf{y} = \sum_{i=1}^N \frac{1}{\sigma_i} \mathbf{u}_i^T \mathbf{y} \mathbf{v}_i \quad (3.14)$$

where \mathbf{u}_i and \mathbf{v}_i are the i th columns of \mathbf{U} and \mathbf{V} , and σ_i is the i th diagonal element of Σ . It is evident that when singular values are close to zero, the corresponding singular basis vectors become very large.

Regularization involves introducing additional information into the mathematical model to handle these small singular values, which makes the inverse problem stable. In some methods, a regularization term $J(\mathbf{x})$ is added to the objective function of the original problem as

$$f_{reg} = f(\mathbf{x}) + \alpha J(\mathbf{x}), \quad (3.15)$$

where α is the weighting parameter. Small values of α lead to solutions that fit the data, while large values favor the solution that matches prior information.

Some regularization techniques follow from a Bayesian approach, where a certain prior distribution is imposed on the model parameters. Other forms of regularization modify or eliminate small singular values of the transfer matrix. Here, the results of some common regularization methods applied to RTI are examined and compared. An overview of regularization and image reconstruction in general can be found in [54] and [55].

3.5.1 Tikhonov

In *Tikhonov* regularization, a regularization term is included in the objective function.

$$f(x) = \frac{1}{2} \|\mathbf{W}\mathbf{x} - \mathbf{y}\|^2 + \alpha \|\mathbf{Q}\mathbf{x}\|^2 \quad (3.16)$$

where \mathbf{Q} is the *Tikhonov matrix* that enforces a solution with certain desired properties. Taking the derivative of (3.16) and setting to zero results in the Tikhonov solution:

$$\mathbf{x}_{TIK} = (\mathbf{W}^T \mathbf{W} + \alpha \mathbf{Q}^T \mathbf{Q})^{-1} \mathbf{W}^T \mathbf{y}. \quad (3.17)$$

Tikhonov regularization provides a simple framework for incorporating desired characteristics into the RTI reconstruction. If smooth images are desired, a difference matrix approximating the derivative of the image can be used in the Tikhonov matrix \mathbf{Q} . If the prior image is known to have a particular Gaussian covariance structure, the root-inverse covariance matrix $\mathbf{C}_x^{-1/2}$ can be used.

One major strength of Tikhonov regularization lies in the fact that the solution is simply a linear projection of the measurement data. Since the projection does not depend on instantaneous measurements, it can be precalculated, and then applied for various measurements for fast image reconstruction. This is very appealing for realtime RTI systems that require frequent image updates [45], [56].

$$\mathbf{P}_{TIK} = (\mathbf{W}^T \mathbf{W} + \alpha \mathbf{Q}^T \mathbf{Q})^{-1} \mathbf{W}^T \quad (3.18)$$

$$\mathbf{x}_{TIK} = \mathbf{P}_{TIK} \mathbf{y} \quad (3.19)$$

3.5.2 Truncated Singular Value Decomposition (TSVD)

Another common form of regularization called *truncated singular value decomposition* (TSVD) is achieved by removing small singular values from the transfer matrix

\mathbf{W} . In this method, only the largest k singular values are kept in the reconstruction shown in (3.14),

$$\mathbf{x}_{TSVD} = \sum_{i=1}^{k \leq N} \frac{1}{\sigma_i} \mathbf{u}_i^T \mathbf{y} \mathbf{v}_i = \mathbf{V}_k \Sigma_k^{-1} \mathbf{U}_k^T \mathbf{y} \quad (3.20)$$

where

$$\mathbf{U}_k = [\mathbf{u}_1, \mathbf{u}_2, \dots, \mathbf{u}_k] \quad (3.21)$$

$$\mathbf{V}_k = [\mathbf{v}_1, \mathbf{v}_2, \dots, \mathbf{v}_k] \quad (3.22)$$

$$\Sigma_k^{-1} = \text{diag}(\sigma_1^{-1}, \sigma_2^{-1}, \dots, \sigma_k^{-1}). \quad (3.23)$$

The TSVD technique is a reduction of the dimensionality of the true solution. It can be thought of as a projection of the solution onto a subspace spanned by the remaining singular vectors. Those singular vectors are dependent on the device itself, or in RTI, the node locations and signal propagation model. Since the projection is based on the device itself, TSVD lacks the ability for incorporation of known or desired image properties into the results.

Like Tikhonov regularization, a transform matrix can be pre-calculated and applied to data for fast image reconstruction in realtime applications.

$$\mathbf{P}_{TSVD} = \mathbf{V}_k \Sigma_k^{-1} \mathbf{U}_k^T \quad (3.24)$$

$$\mathbf{x}_{TSVD} = \mathbf{P}_{TSVD} \mathbf{y} \quad (3.25)$$

3.5.3 Total Variation

Total Variation (TV) is a form of nonlinear regularization that penalizes changes in the solution. Mathematically, total variation takes the form

$$f(\mathbf{x}) = \frac{1}{2} \|\mathbf{W}\mathbf{x} - \mathbf{y}\|^2 + \alpha TV(\mathbf{x}) \quad (3.26)$$

where

$$TV(\mathbf{x}) = \sum_i |\nabla \mathbf{x}|_i, \quad (3.27)$$

and $|\nabla \mathbf{x}|_i$ is the i th element of the gradient of \mathbf{x} . In other words, the integration of gradient magnitude is minimized.

It is not possible to calculate the gradient and Hessian of $TV(\mathbf{x})$, which is necessary for most numerical optimization algorithms to converge reliably and quickly. To address this problem, a differentiable function is used as an approximate:

$$TV(\mathbf{x}) \simeq \sum_i \sqrt{\|\nabla \mathbf{x}\|_i^2 + \beta^2}. \quad (3.28)$$

This approximation is based on

$$|a| = \sqrt{a^2} \simeq \sqrt{a^2 + \beta^2} \quad (3.29)$$

for small β , which removes the discontinuity at $a = 0$. The objective function for total variation becomes

$$f(\mathbf{x}) = \frac{1}{2} \|\mathbf{W}\mathbf{x} - \mathbf{y}\|^2 + \alpha \sum_i \sqrt{\|\nabla \mathbf{x}\|_i^2 + \beta^2}. \quad (3.30)$$

Using this approximation, the gradient and Hessian information is easily obtained and utilized in a numerical optimization procedure. The parameter β is tunable, and relates to the “sharpness” of the images generated by the TV regularization. Total variation penalizes slow changes in an image, and therefore can lead to images that maintain sharp transitions if parameters are set accordingly.

3.6 Results

This section presents images that are reconstructed using the regularization techniques described in Section 3.5. For each image, the same RTI measurement data \mathbf{y} and transfer matrix \mathbf{W} were used, and Table 3.1 lists the model and calibration parameters.

The experiment is performed in an area with furniture, walls, moving people, and other building structures to provide a rich multipath environment. The wireless network is comprised of twenty eight “Telosb” wireless nodes by Crossbow, and each node operates on the IEEE 802.15.4 specification. A token passing protocol is implemented so that node transmissions do not collide.

The nodes are set up in a square network with a length of 4.2 meters on each side, establishing a network image area of 17.6 square meters (196 square feet). Each side of the square contains eight nodes separated by approximately .6 meters (2 feet), as depicted in Fig. 3.3. The nodes are placed on stands approximately

four feet off the ground so that line-of-sight paths travel through humans at torso level.

To image the change in attenuation, RSS measurements of each link are taken at time $t = t_a$ as described in Section 3.4. During this calibration period, the network area is vacant from moving objects. The signal strength from each link is measured N_c times and is averaged over the entire calibration period. After calibration, when the RTI network is in use, all instantaneous measurements are taken as the difference from the calibration measurements. This provides the difference measurement vector $\Delta \mathbf{y}$ in (3.7), which is required to image motion within the network. In other words, any attenuation that was not part of the calibration at time $t = t_a$ is imaged.

It should be noted that only one image result is provided for each regularization method. Different regularization parameters will yield different results, but the parameters chosen in this section provided good results in terms of the ability to distinguish the location of changed attenuation. Other parameters were not able to produce significantly better image results in our experiments.

3.6.1 Tikhonov

A difference matrix approximating the derivative operator is applied as the Tikhonov matrix \mathbf{Q} . By minimizing the energy found within the image derivative, noise spikes are suppressed and a smooth image is produced.

Since the image is two dimensional, the regularization should include the derivatives in both the vertical and horizontal directions. The matrix \mathbf{D}_X is the difference operator for the horizontal direction, and \mathbf{D}_Y is the difference operator for the vertical direction. The regularized function can be written in this case as

$$f(\mathbf{x}) = \frac{1}{2} \|\mathbf{W}\mathbf{x} - \mathbf{y}\|^2 + \alpha (\|\mathbf{D}_X\mathbf{x}\|^2 + \|\mathbf{D}_Y\mathbf{x}\|^2), \quad (3.31)$$

which results in the solution

$$\mathbf{x}_{Tik} = (\mathbf{W}^T\mathbf{W} + \alpha(\mathbf{D}_X^T\mathbf{D}_X + \mathbf{D}_Y^T\mathbf{D}_Y))^{-1}\mathbf{W}^T\mathbf{y}. \quad (3.32)$$

When the derivative is used as the Tikhonov matrix, this is also known as *H1 regularization*.

As seen in Fig. 3.7 and Fig. 3.7, H1 regularization results in very smooth RTI results for $\alpha = 2$. The difference operators act as a low-pass filter, smoothing the noise and blurring any sharp changes in attenuation. The smoothness can be increased or decreased by choosing α appropriately.

3.6.2 Truncated Singular Value Decomposition (TSVD)

As described in Section 3.5, TSVD regularization removes spectral components of \mathbf{W} that correspond to low singular values. This means that all information in the spectral components that are removed are entirely lost from the solution.

The limitations of TSVD regularization when applied to RTI are evident in Fig. 3.7 and Fig. 3.7. The image is rough due to the high frequency components that are included in the reconstruction, and yet contrast remains low when the threshold is set to $\tau = 5.6$. This makes it difficult for a human or image processing algorithm to determine where objects are located. Other thresholds did not significantly improve the image.

3.6.3 Total Variation

As explained in Section 3.6.1, the gradient of a two-dimensional image is approximated by two difference matrices \mathbf{D}_X and \mathbf{D}_Y . This leads to the regularization function for total variation

$$TV(\mathbf{x}) \simeq \sum_i \sqrt{\|\mathbf{D}_Y \mathbf{x}\|_i^2 + \|\mathbf{D}_X \mathbf{x}\|_i^2 + \beta}. \quad (3.33)$$

The minimum of the total variation least-squares problem is found using a numerical optimization algorithm. In this experiment, the *BFGS* algorithm is used [57].

The total variation results shown in Fig. 3.7 and Fig. 3.7 for $\alpha = .35$ and $\beta = .08$ demonstrate the capability of TV regularization in maintaining sharpness of RTI images. The combination of sharp edge definition and low noise make total variation appealing for RTI, but the computational complexity of the numerical optimization is more than Tikhonov or TSVD regularization. This is due to the fact that the solution must be obtained using a numerical optimization algorithm instead of a simple matrix multiplication, as is the case with Tikhonov and TSVD.

3.7 Conclusion

Radio tomographic imaging is an ill-posed inverse problem. Since many different attenuation fields can lead to the same noisy measurement data, no unique solution to the least-squares formulation exists. The problem is made stable by incorporating additional information about the solution into the mathematical framework.

Tikhonov regularization is appealing for RTI systems due to the flexibility to incorporate desired image characteristics into the solution. It follows naturally from a Bayesian approach where the statistical distribution of the image is assumed or known. Since the Tikhonov solution is a linear transformation of the measurement data, it is useful for realtime RTI systems where fast reconstruction of images is needed.

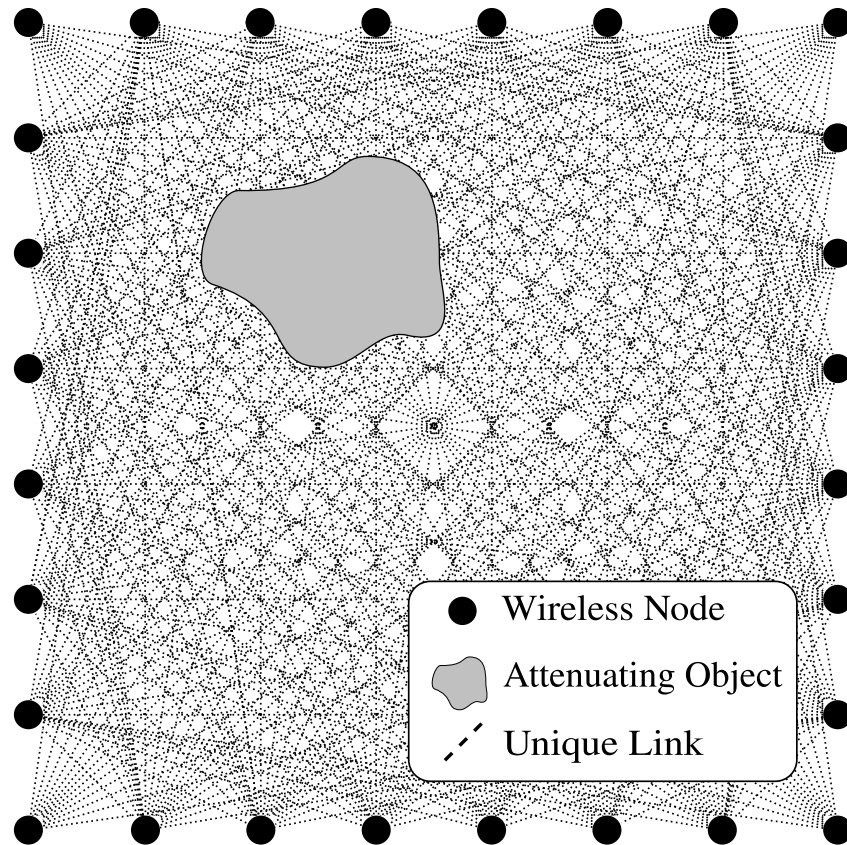
Truncated singular value decomposition is a natural form of regularization that does not require prior information about the solution. This can be viewed as both a strength and a weakness, since it is often helpful to incorporate desired image properties. Our experimental results indicate that TSVD-RTI images are noisier than the other regularization methods, and lack the contrast needed to accurately distinguish the location of moving objects.

Total Variation is useful when the preservation of sharp edges in the image is desired. Experimental results show that TV-RTI images contain a large amount of contrast without much noise, making it easier to distinguish the location of objects. It requires two regularization parameters, however, and is more computationally expensive than the other methods presented in this paper.

The results presented in this paper demonstrate that regularization plays an import role in tracking the location of moving objects with radio tomographic imaging. While this paper presents some common forms of regularization, many other regularization and image reconstruction techniques could be applied to RTI in future work.

Table 3.1. Calibration and model parameters

Parameter	Value	Description
N	28	Number of nodes
N_c	2000	Number of calibration frames
Δ_p	.17	Pixel width (m)
λ	.01	Width of weighting ellipse in (3.9) (m)

**Figure 3.1.** An illustration of an RTI network. Each node broadcasts to the others, creating many projections that can be used to reconstruct an image of objects inside the network area.

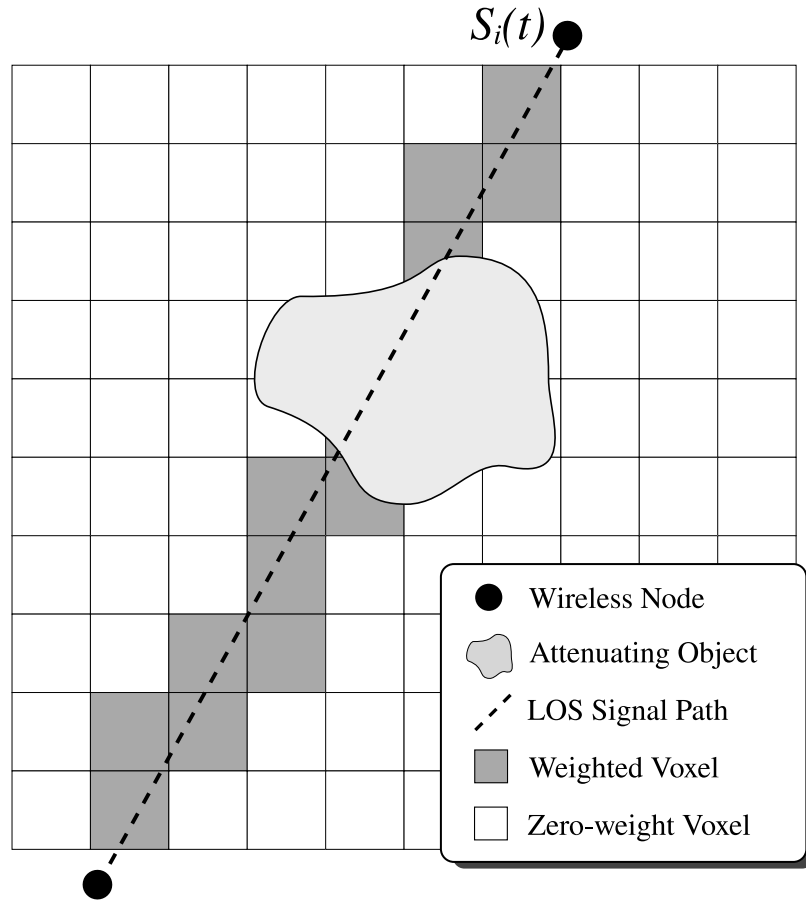


Figure 3.2. An illustration of a single link in an RTI network that travels in a direct LOS path. The signal is shadowed by objects as it crosses the area of the network in a particular path. The darkened voxels represent the image areas that have a non-zero weighting for this particular link.

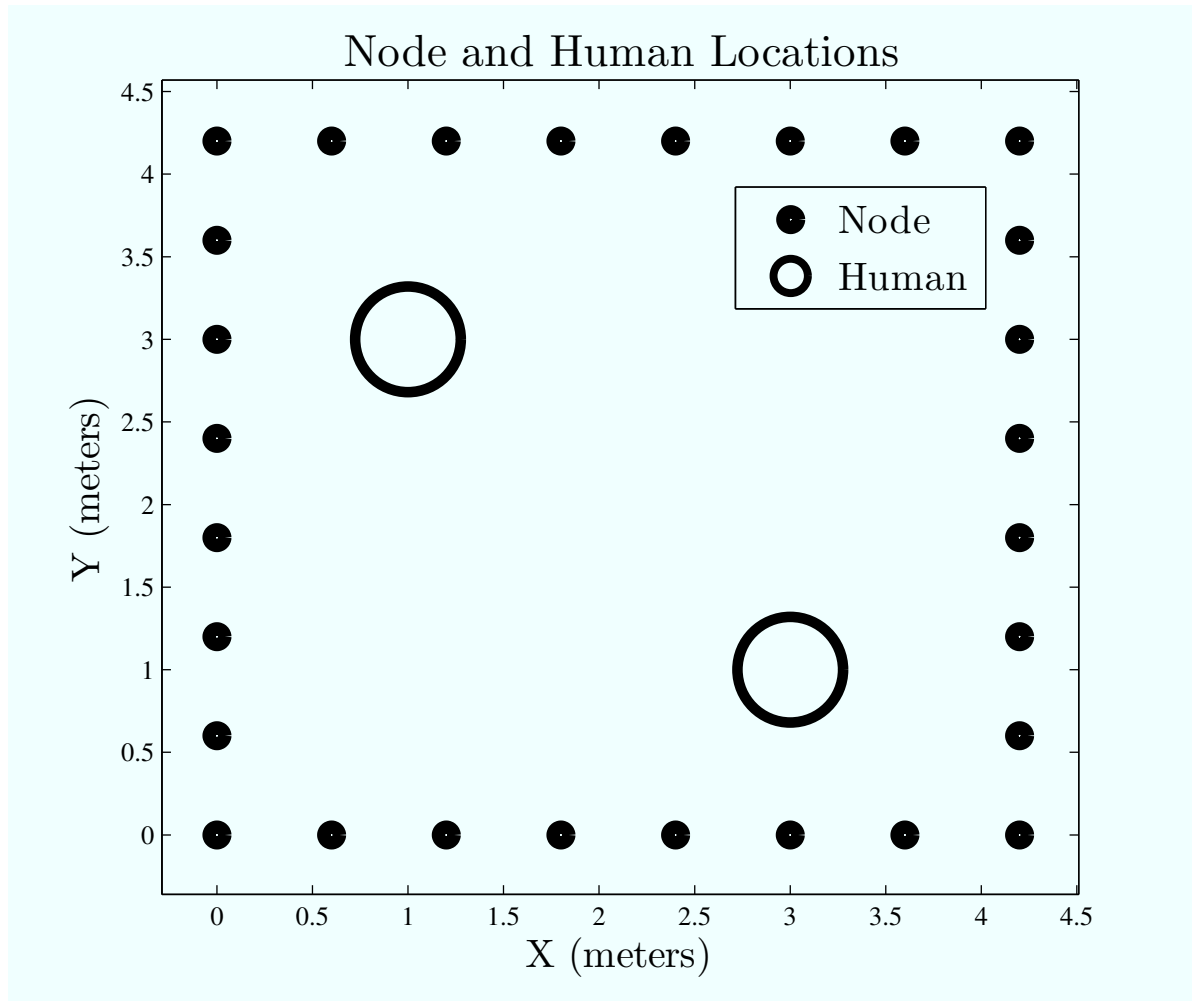


Figure 3.3. The RTI geometry and human locations for the images found in Section 3.6. Twenty-eight nodes are placed in a square perimeter, with two humans standing inside the area at coordinates (3,1) and (1,3).

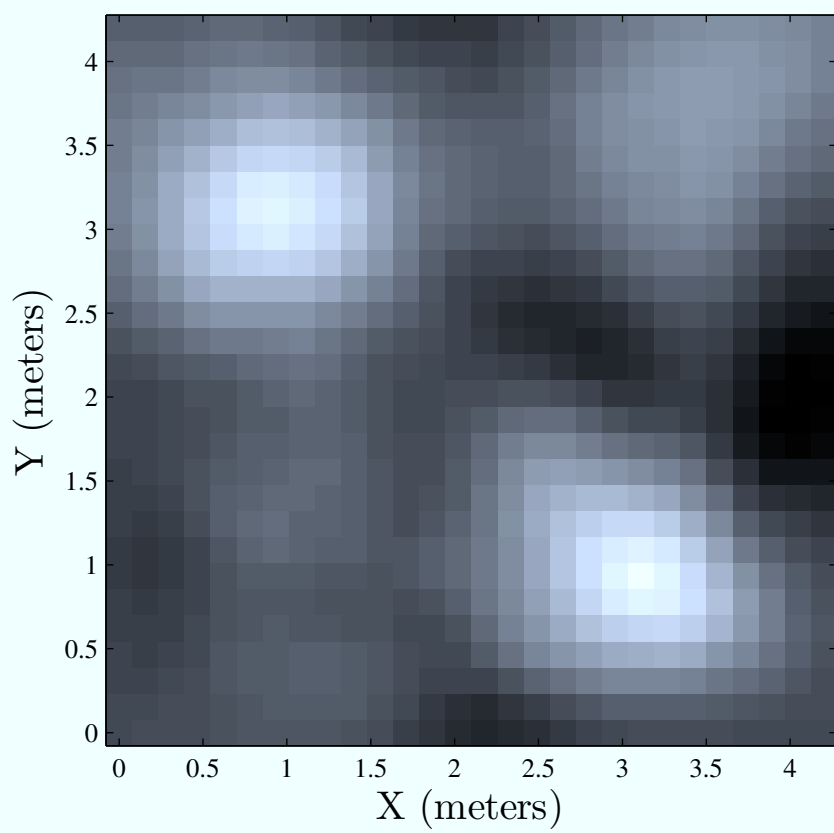


Figure 3.4. RTI results using H1 regularization with parameter $\alpha = 2$ using forward difference matrices.

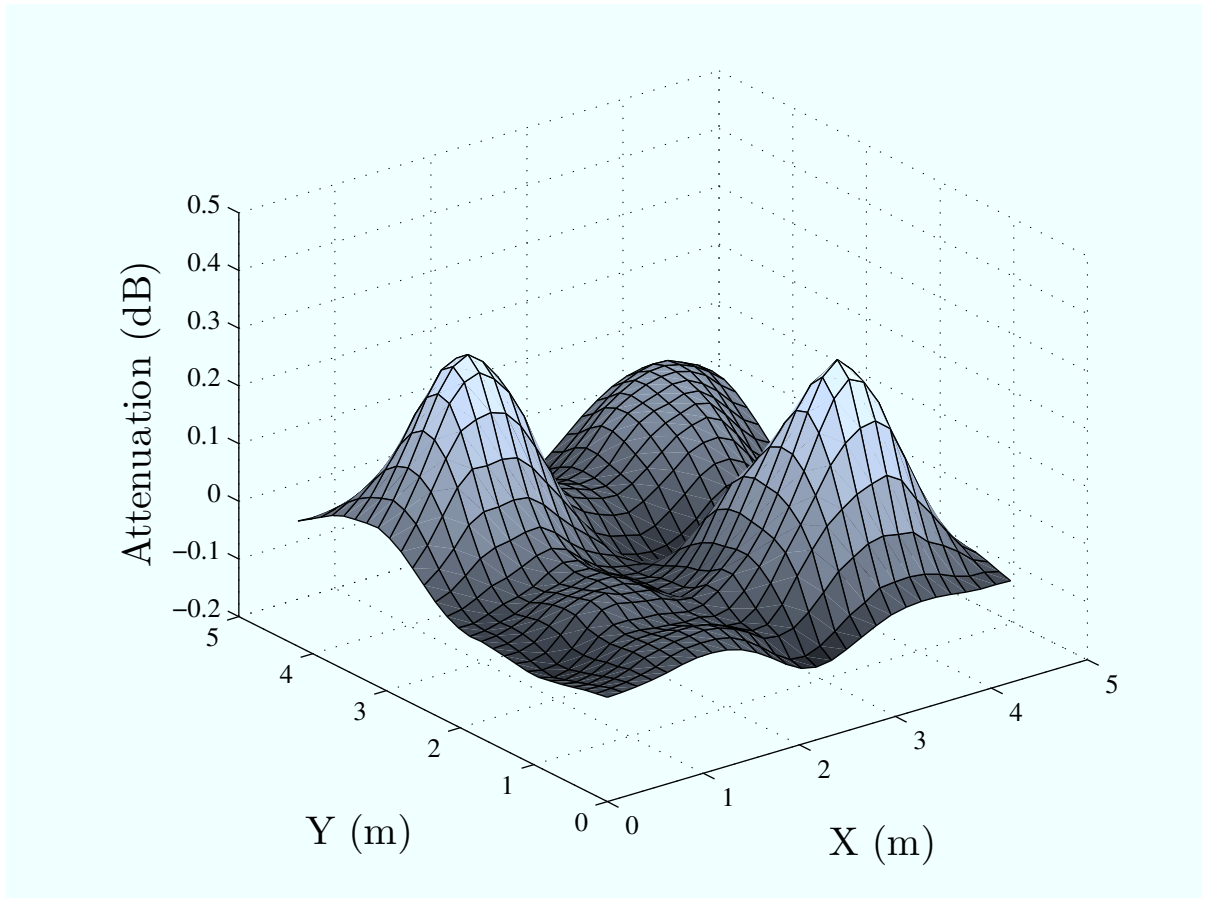


Figure 3.5. RTI results using H1 regularization with parameter $\alpha = 2$ using forward difference matrices.

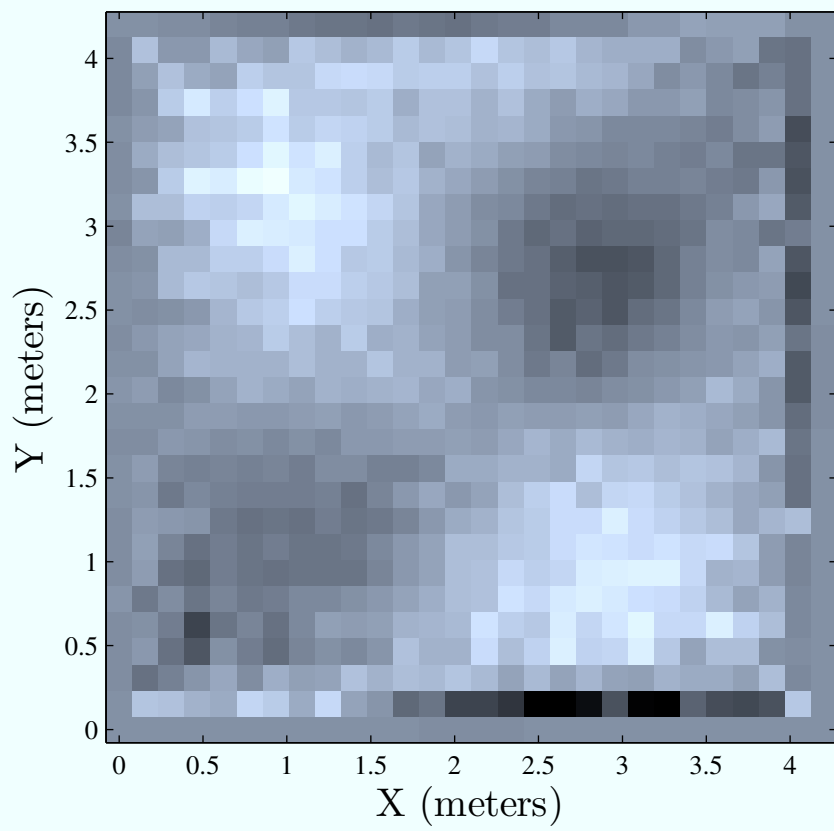


Figure 3.6. RTI results using truncated singular value regularization. Here, any singular value below the threshold $\tau = 5.6$ is truncated.

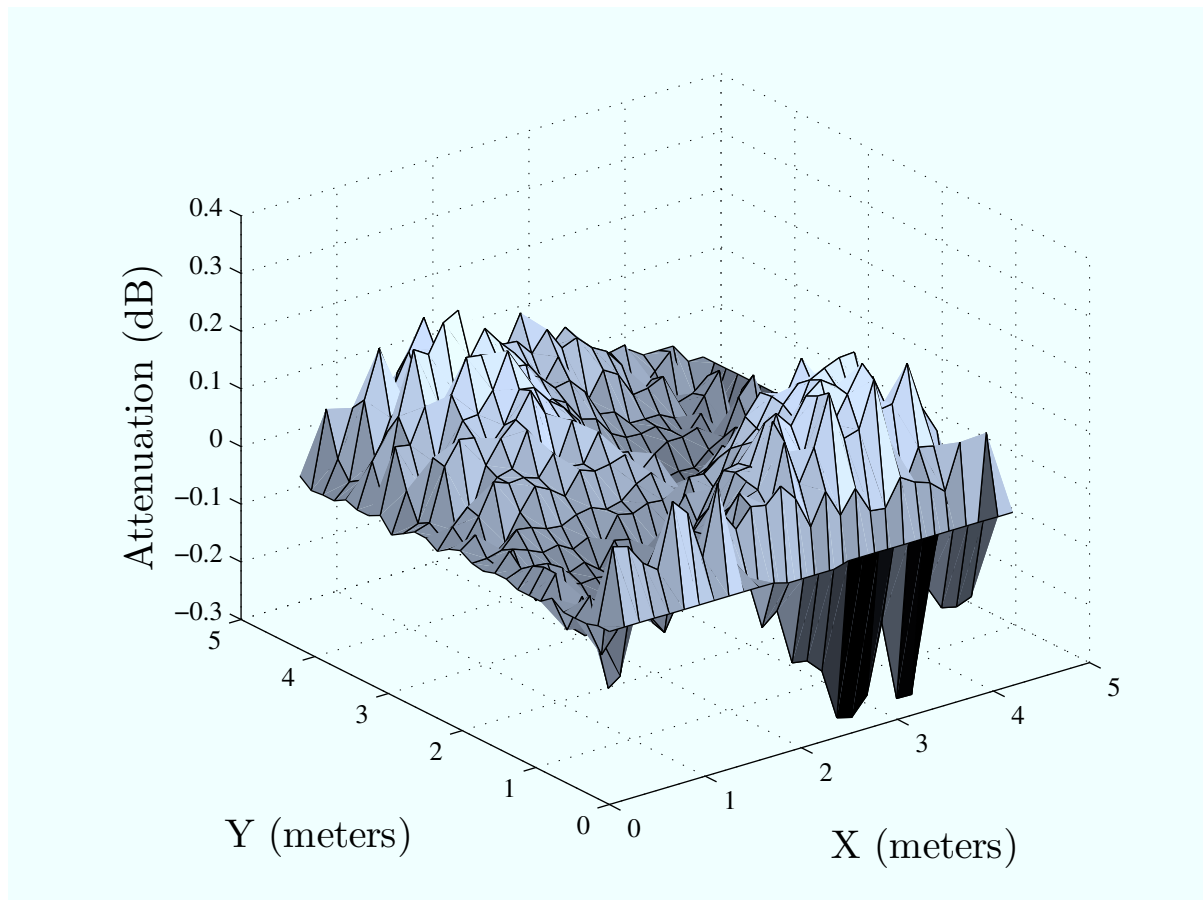


Figure 3.7. RTI results using truncated singular value regularization. Here, any singular value below the threshold $\tau = 5.6$ is truncated.

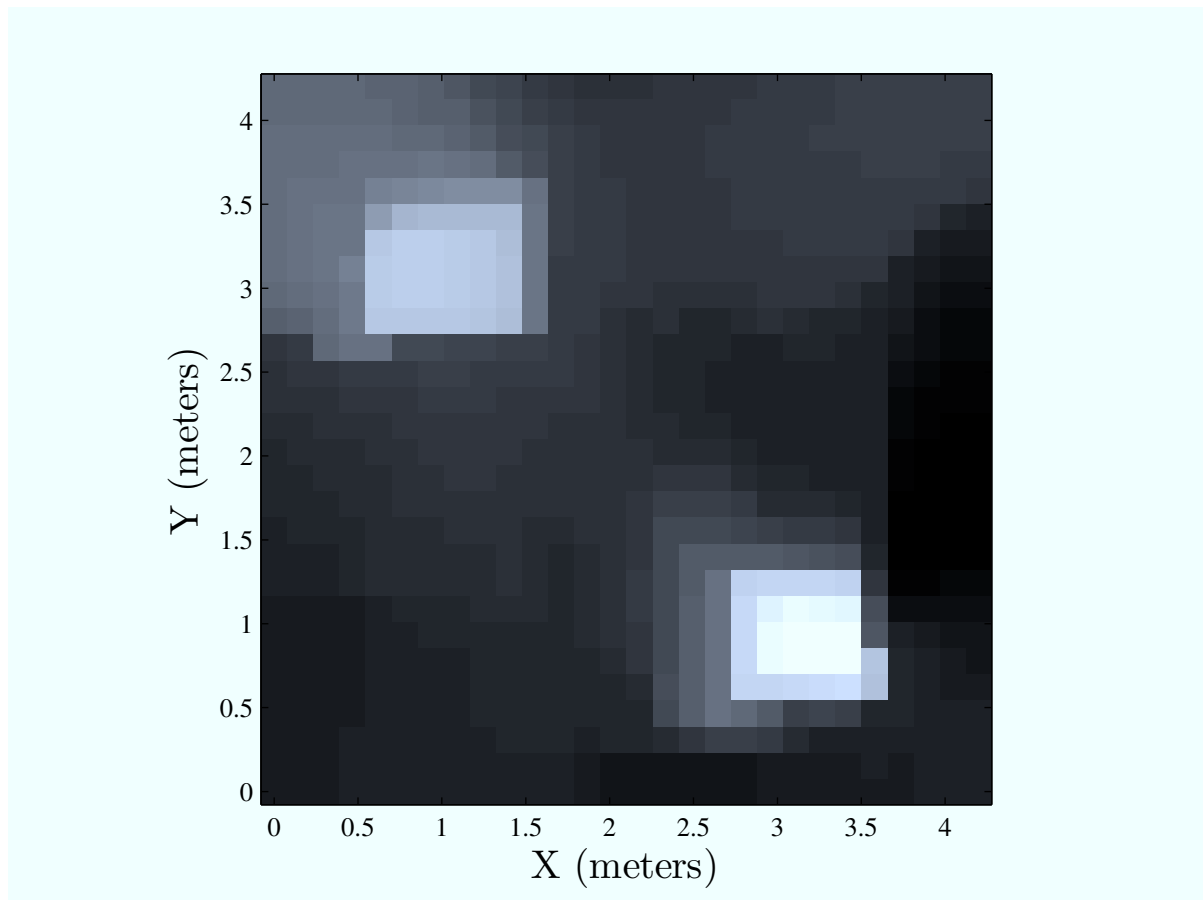


Figure 3.8. RTI results using total variation regularization with parameter $\alpha = .35$ and $\beta = .08$.

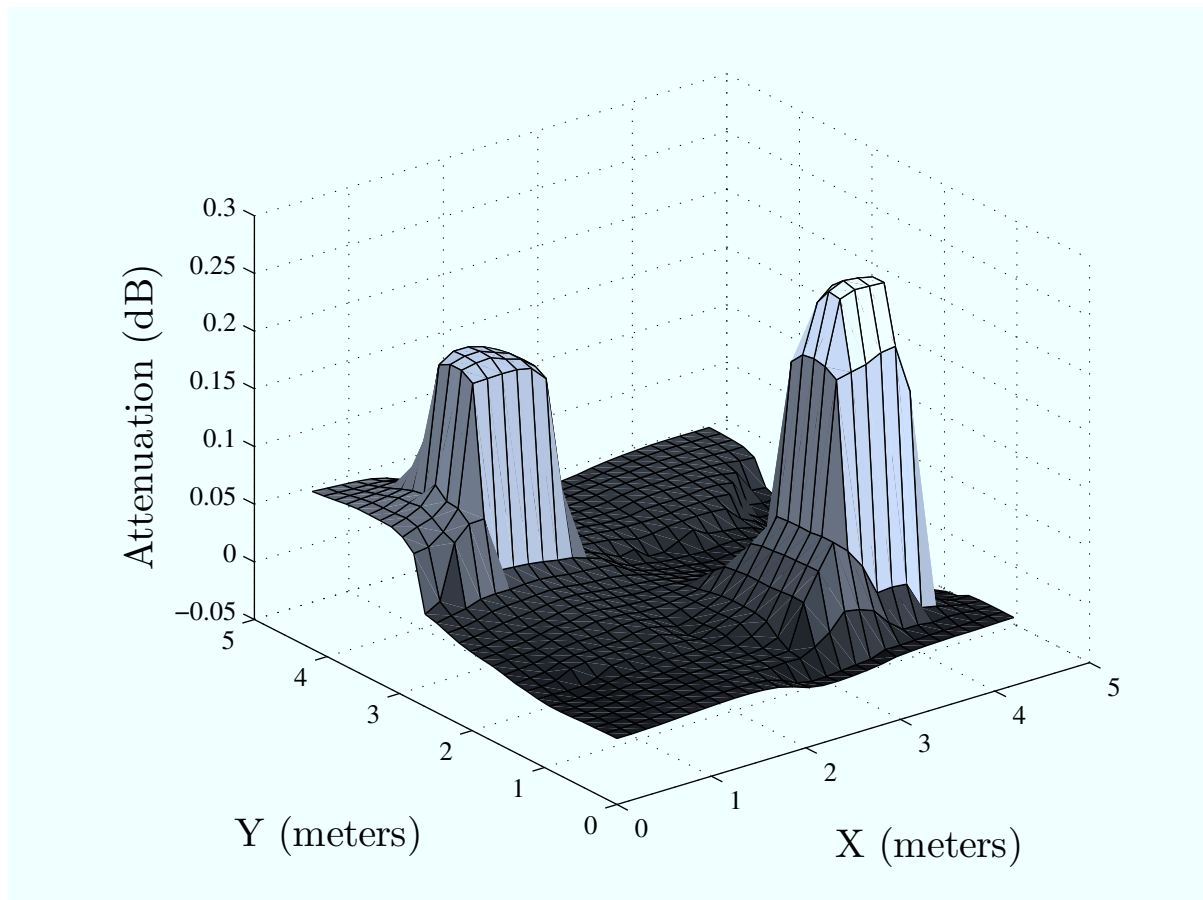


Figure 3.9. RTI results using total variation regularization with parameter $\alpha = .35$ and $\beta = .08$.

CHAPTER 4

THROUGH-WALL MOTION TRACKING USING VARIANCE-BASED RADIO TOMOGRAPHY NETWORKS

4.1 Abstract

This paper presents a new method for imaging, localizing, and tracking motion behind walls in real-time. The method takes advantage of the motion-induced variance of received signal strength measurements made in a wireless peer-to-peer network. Using a multipath channel model, we show that the signal strength on a wireless link is largely dependent on the power contained in multipath components that travel through space containing moving objects. A statistical model relating variance to spatial locations of movement is presented and used as a framework for the estimation of a motion image. From the motion image, the Kalman filter is applied to recursively track the coordinates of a moving target. Experimental results for a 34-node through-wall imaging and tracking system over a 780 square foot area are presented.

4.2 Introduction

This paper explores a method for tracking the location of a person or object behind walls, without the need for an electronic device to be attached to the target. The technology is an extension of “radio tomographic imaging” [15], which is so-called because of its analogy to medical tomographic imaging methods. We call this extension *variance-based radio tomographic imaging*¹ (*VRTI*), since it uses the signal strength variance caused by moving objects within a wireless network. The general field of locating people or objects when they do not carry a device is also

¹This chapter first appeared in J. Wilson and N. Patwari, “See Through Walls: Motion Tracking Using Variance-Based Radio Tomography Networks“, IEEE Transactions on Mobile Computing, 2010, and is reprinted with permission.

called “device-free passive localization” [13] in contrast to technologies like active radio frequency identification (RFID) which only locate objects that carry a radio transmitter.

For context-aware systems, a user’s context includes the locations of people in the nearby environment [58]. Typically, location aware systems require the participation of people who must wear tags to be located and identified [59]. We envision applications in which requiring participation is not possible. For example, emergency responders, military forces, or police arrive at a scene where entry into a building is potentially dangerous. They deploy radio sensors around (and potentially on top of) the building area, either by throwing or launching them, or dropping them while moving around the building. The nodes immediately form a network and self-localize, perhaps using information about the size and shape of the building from a database (*e.g.*, Google maps) and some known-location coordinates (*e.g.*, using GPS). Then, nodes begin to transmit, making signal strength measurements on links which cross the building or area of interest. The RSS measurements of each link are transmitted back to a base station and used to estimate the positions of moving people and objects within the building. Based on these inputs, the context aware system can aid decisions about how to focus responders’ efforts.

Radio tomography provides life-saving benefits for emergency responders, police, and military personnel arriving at potentially dangerous situations. Many correctional and law enforcement officers are injured each year because they lack the ability to detect and track offenders through building walls [34]. By showing the locations of people within a building during hostage situations, building fires, or other emergencies, radio tomography can help law enforcement and emergency responders to know where they should focus their attention.

This paper explores the use of radio tomography in highly obstructed areas for the purpose of tracking moving objects through walls. First, a review of previous work and related research is summarized in Section 4.3. In Section 4.4, we address a fundamentally different method for the use of RSS measurements which we call *variance-based radio tomography (VRTI)*. When a moving object affects the amplitude or phase of one or more multipath components over time, the phasor sum of all multipath at the receiver experiences changes, and higher RSS variance is observed.

The amount of RSS variance relates to the physical location of motion, and an image representing motion is estimated using measurements from many links in the wireless network.

We briefly review the Kalman filter and apply it in Section 4.5 to track the location of a moving object or person. In Section 4.6, experimental results demonstrate the use of RSS variance to locate a moving object on the inside of a building. This section also quantifies the accuracy of localization by comparing known movement paths with those estimated by the VRTI tracking system. We show that the VRTI system can track the location of an experimenter behind walls with approximately two feet average error for this experiment.

Finally, Section 4.7 discusses some possibilities for future research. Advances in wireless protocols, antenna design, and physical layer modeling will bring improvements to VRTI through-wall tracking.

4.3 Related Research

Previous work shows that changes in link path losses can be used to accurately estimate an image of the attenuation field, that is, a spatial plot of attenuation per unit area [15]. Experimental tests show that in an unobstructed area surrounded by a network of nodes, the estimated image displayed the positions of people in the area.

Indoor radio channel characterization research demonstrates that objects moving near wireless communication links cause variance in RSS measurements [47]. This knowledge has been applied to detect and characterize motion of network nodes and moving objects in the network environment [10]. Polarization techniques have also been used to detect motion [60]. These studies focus mostly on detection and velocity characterization of movement, but do not attempt to localize the movement as the work presented in this paper does.

Youssef, Mah, and Agrawala [13] demonstrated that variance of RSS on a number of WiFi links in an indoor WLAN can be used to (1) detect if motion is occurring within a wireless network, and (2) localize the moving object based on a manually trained lookup. In many situations, however, manual training is not possible since it can take a significant amount of time and access to the area being

tracked is restricted.

Real-time location systems (RTLS) are based on a technology that uses electronic tags for locating objects. For logistics purposes in large facilities, commercial real-time location systems are deployed by installing infrastructure in the building and attaching active radio frequency identification (RFID) tags to each object to be tracked. RTLS systems are not useful in most emergency operations, however, since they require setup inside of a building prior to system use. Further, RTLS systems cannot locate people or objects which do not have an RFID tag. In emergencies, an operation cannot rely on an adversary wearing a tag to be located. Thus, tag-based localization methods are insufficient for most emergency and security applications.

An alternate tag-free localization technology is ultra-wideband (UWB) through-wall imaging (TWI) (also called through-the-wall surveillance). In radar-based TWI, a wideband phased array steers a beam across space and measures the delay of the reflection response, estimating a bearing and distance to each target. Through-wall radar imaging has garnered significant interest in recent years [61–65], for both static imaging and motion detection. Commercial products include Cambridge Consultants’ Prism 200 [37] and Camero Tech’s Xaver800 [38], and are prohibitively expensive for most applications, on the order of US \$100,000 per unit. These products are accurate close to the device, but inherently suffer from accuracy and noise issues at long range due to monostatic radar losses. In free space at distance d , radar systems measure power proportional to $1/d^4$, in comparison to $1/d^2$ for radio transmission systems.

Radio tomography takes a fundamentally different approach from traditional TWI systems by using large networks of sensors. While initial attempts [39] have allowed 2-4 high-complexity devices to collaborate in TWI, our research investigates the use of tens or hundreds of collaborating nodes to simultaneously image a larger area than possible with a single through-wall radar. RTI’s imaging capability increases as $\mathcal{O}(N^2)$ for N sensors, thus large networks, rather than highly capable nodes, lead to improved imaging and tracking capabilities.

Multistatic radar research has also developed technologies called multiple-input multiple-output (MIMO) radar. These technologies also use distributed devices, perhaps without phase-synchronization, in order to measure radar scattering [44].

The use of many distributed antennas is a type of spatial diversity for a radar system which can then avoid nulls in the radar cross-section (RCS) of a scattering object as a function of scattering angle [66].

MIMO radar is a complementary technology to radio tomography. While MIMO radar measures scattering of the transmitted signal by the object of interest, radio tomography methods are based on measurements of transmission through a medium. Integration of the two modalities is beyond the scope of this paper, but is perhaps a promising direction for future research.

4.4 Variance-Based Radio Tomographic Imaging

In this section, we introduce and justify a model which relates motion in spatial voxels to the variance of signal strength measured on the links of a wireless network. In particular, we justify the assumption of a linear model when motion is sparse, and describe the limits on the validity of such a model.

4.4.1 Measurement Model

The goal of a VRTI system is to use a vector \mathbf{s} of RSS variance measurements on M links in a wireless network to determine an image vector \mathbf{x} that describes the presence of motion occurring within N voxels of a physical space. We first describe the image vector, then specifically define RSS, and discuss RSS variance.

The image vector \mathbf{x} is a representation of motion occurring within each spatial voxel of the network area, with j th element given by

$$x(j) = \begin{cases} 1 & \text{if motion occurs in voxel } j \\ 0 & \text{otherwise} \end{cases} \quad (4.1)$$

What we call the “received signal strength” (RSS) is actually a measure of the received power in decibels. In a multipath environment, a wireless signal travels along many paths from transmitter to receiver. Each path has associated with it an amplitude and phase, and the received signal is a summation of each incoming multipath component. The complex baseband voltage for a continuous-wave (CW) signal measured at a receiver is expressed as [67],

$$\tilde{V} = \nu + \sum_{i=1}^L V_i \exp(j\Phi_i), \quad (4.2)$$

where ν is the additive noise, V_i is the magnitude and Φ_i is the phase of the i th multipath component (wave) impinging on the receiver antenna. The received power is thus $\|\tilde{V}\|^2$, and so the RSS, denoted R_{dB} , is given as $R_{dB} = 10 \log_{10} \|\tilde{V}\|^2$.

The RSS variance vector \mathbf{s} contains for each link a measure of the variance of R_{dB} . In Section 4.4.2, we show how this variance has a linear relationship with the total power in affected multipath. Then in Section 4.4.3, we argue that this total affected power has a linear relationship with \mathbf{x} , for the case of sparse motion. In sum, we justify the following linear model. We approximate $\text{Var}[R_{dB}]$ as a linear combination of the movement occurring in each voxel, weighted by the amount of variance that motion in that particular voxel causes on the link's RSS,

$$\text{Var}[R_{dB}] = \sum_j w_j x(j) + n, \quad (4.3)$$

where n is measurement noise and modeling error, and w_j is the variance caused by movement in voxel j . For all links, we have

$$\mathbf{s} = \mathbf{W}\mathbf{x} + \mathbf{n} \quad (4.4)$$

where \mathbf{W} is an $M \times N$ matrix representing the variance weighting for each pixel and link, and \mathbf{n} is a $M \times 1$ noise vector.

4.4.2 Variance and Total Affected Power

In this section, we argue that the RSS variance, $\text{Var}[R_{dB}]$, and the total affected power have a linear relationship. First, we define affected power. We classify each multipath as either *affected* or *static*: A multipath i is described as affected if its amplitude and/or phase change randomly as a result of the current position of people and/or objects in the channel, or static if it is not. We denote $\mathcal{A}(\mathbf{x})$ to be the indices of the affected multipath given the motion described in \mathbf{x} . Then we define the total affected power, $T_{AP}(\mathbf{x})$, as

$$T_{AP}(\mathbf{x}) = \sum_{i \in \mathcal{A}(\mathbf{x})} |V_i|^2. \quad (4.5)$$

We show that T_{AP} has a linear relationship with $\text{Var}[R_{dB}]$ for a wide range of $\text{Var}[R_{dB}]$.

Rearranging the multipath in (4.2) into affected and static contributions,

$$\tilde{V} = \nu + \sum_{i \notin \mathcal{A}(\mathbf{x})} V_i \exp(j\Phi_i) + \sum_{i \in \mathcal{A}(\mathbf{x})} V_i \exp(j\Phi_i). \quad (4.6)$$

The sum of static multipath do not change, and thus we can rewrite (4.6) as

$$\tilde{V} = \bar{V} \exp(j\bar{\Phi}) + \sum_{i \in \mathcal{A}(\mathbf{x})} V_i \exp(j\Phi_i) + \nu, \quad (4.7)$$

where \bar{V} and $\bar{\Phi}$ are the magnitude and phase angle of $\sum_{i \notin \mathcal{A}(\mathbf{x})} V_i \exp(j\Phi_i)$, respectively. We consider the V_i and Φ_i for affected multipath to be random.

It is well known in the wireless communications literature [68,69] that $|\tilde{V}|$, as it is given in (4.7), is well represented as a Ricean random variable. The voltage $\bar{V}e^{j\bar{\Phi}}$ is analogous to the specular signal in a Ricean channel, while the remaining terms are the diffuse signal components. The K factor of the Ricean distribution for $|\tilde{V}|$ is defined as,

$$\begin{aligned} K &= \frac{\bar{V}^2}{2\sigma^2} = \frac{\bar{V}^2}{2[\sigma_\nu^2 + T_{AP}(\mathbf{x})]} \\ &= \frac{1}{2} \left[\frac{\sigma_\nu^2}{\bar{V}^2} + \frac{T_{AP}(\mathbf{x})}{\bar{V}^2} \right]^{-1} \end{aligned} \quad (4.8)$$

where $\sigma^2 = \sigma_\nu^2 + T_{AP}(\mathbf{x})$ is the power in the affected power and noise, and $T_{AP}(\mathbf{x})$ is defined in (4.5). We refer to $T_{AP}(\mathbf{x})/\bar{V}^2$ as the normalized total affected power (normalized TAP).

Moreover, we have a known relationship between the variance of RSS and K . Since $R_{dB} = 10 \log_{10} \|\tilde{V}\|^2$ and $|\tilde{V}|$ is Ricean, R_{dB} has the log-Ricean pdf. The variance of R_{dB} is calculated numerically as a function of K . Note that for constant K , the scale of σ^2 and \bar{V}^2 do not change $\text{Var}[R_{dB}]$. Combining the numerically calculated relationship between $\text{Var}[R_{dB}]$ and K , and (4.8), we plot in Figure 4.1 the functional dependence of $\text{Var}[R_{dB}]$ on normalized TAP.

As seen in Figure 4.1, the variance of RSS is linearly related to normalized TAP for normalized TAP less than 0.25. That is, when the total power affected by a person's motion is less than 25% of the total static power in the link, the variance is linear with normalized TAP. For through-wall imaging, the power affected by the motion inside of the building is typically low, because multipath which penetrate

two external walls to enter and exit the building are low in power compared to multipath which diffract around the building's exterior.

For high normalized TAP, the variance strictly increases, so motion can be detected using VRTI, but the nonlinearities make the linear model, and thus the proposed image estimator, less accurate. In this case, we note that moving objects are also likely to cause a reduction in the mean received power, because they typically cause some shadowing of the affected multipath. As a result, shadowing-based RTI may be better approach than variance-based RTI when most of the multipath power is affected, that is, when all links are LOS, but not in through-wall deployments.

In short, RSS variance has a linear relationship with total affected power, over the most important range of normalized TAP for purposes of variance-based RTI.

4.4.3 Total Affected Power and Motion

In this section, we argue that for sparse motion, the total affected power is approximately linear in \mathbf{x} . Assume that multipath component i travels through a subset of space \mathcal{S}_i . This subset \mathcal{S}_i might be some narrow volume around the line tracing its path from the transmitter to receiver, for example. We assume that a path i is affected due to object motion in voxel j centered at \mathbf{z}_j if $\mathbf{z}_j \in \mathcal{S}_i$, then path i is affected, *i.e.*,

$$\mathcal{A}(\mathbf{x}) = \{i : x(j) > 0 \cap \mathbf{z}_j \in \mathcal{S}_i, \text{ for some } j\}.$$

Note that $x(j)$ is non-negative as given in (4.1). Now consider two motion images, \mathbf{x}_1 and \mathbf{x}_2 . The affected multipath in the sum motion image, $\mathbf{x} = \mathbf{x}_1 + \mathbf{x}_2$, is given by

$$\begin{aligned} \mathcal{A}(\mathbf{x}) &= \{i : x_1(j) + x_2(j) > 0 \cap \mathbf{z}_j \in \mathcal{S}_i, \text{ for some } j\} \\ &= \mathcal{A}(\mathbf{x}_1) \cup \mathcal{A}(\mathbf{x}_2). \end{aligned} \tag{4.9}$$

Then the total affected power as defined in (4.5) due to the sum of the motion vectors is

$$T_{AP}(\mathbf{x}) = \sum_{i \in \mathcal{A}(\mathbf{x}_1) \cup \mathcal{A}(\mathbf{x}_2)} |V_i|^2 = \sum_{i \in \mathcal{A}(\mathbf{x}_1)} |V_i|^2 + \sum_{i \in \mathcal{A}(\mathbf{x}_2)} |V_i|^2 - \sum_{i \in \mathcal{A}(\mathbf{x}_1) \cap \mathcal{A}(\mathbf{x}_2)} |V_i|^2 \tag{4.10}$$

This intersection $\mathcal{A}(\mathbf{x}_1) \cap \mathcal{A}(\mathbf{x}_2)$ is the set of multipath affected by both motion images \mathbf{x}_1 and \mathbf{x}_2 .

Now, let \mathbf{x}_1 and \mathbf{x}_2 be sparse motion images with motion only in voxels j_1 and j_2 , respectively. Then

$$\mathcal{A}(\mathbf{x}_1) \cap \mathcal{A}(\mathbf{x}_2) = \{i : \mathbf{z}_{j_1} \in \mathcal{S}_i \cap \mathbf{z}_{j_2} \in \mathcal{S}_i\},$$

that is, multipath which cross through both voxels j_1 and j_2 . We argue that for close voxels, *i.e.*, $\|\mathbf{z}_{j_1} - \mathbf{z}_{j_2}\|$ small, there may be multipath which cross through both voxels. However, for voxels j_1 and j_2 far apart, there will be relatively few multipath components which cross through both voxels, compared to the multipath which cross through only one. In this latter case, (4.10) becomes,

$$T_{AP}(\mathbf{x}_1 + \mathbf{x}_2) \approx \sum_{i \in \mathcal{A}(\mathbf{x}_1)} |V_i|^2 + \sum_{i \in \mathcal{A}(\mathbf{x}_2)} |V_i|^2. \quad (4.11)$$

In general, when the non-zero motion voxels in \mathbf{x}_1 and \mathbf{x}_2 are relatively distant, the approximation in (4.11) is valid. This model, in combination with the linearity between $T_{AP}(\mathbf{x})$ and the RSS variance, justifies approximating \mathbf{s} as a linear transformation of \mathbf{x} as given in (4.4).

4.4.4 Elliptical Weight Model

If knowledge of an environment were available, one could estimate the variance weights w_j for each link. Perhaps calibration measurements or ray tracing techniques could aid in estimation of the linear transformation \mathbf{W} . For time-critical emergency operations, one cannot expect to obtain floor plans and interior arrangements of the building. With no site-specific information, we require a statistical model that describes the contribution of motion in each pixel to a link's variance.

One such statistical model has been described for link shadowing is the normalized elliptical model [15, 46]. Consider an ellipsoid with foci at the transmitter and receiver locations. The excess path length of multipath contained within this ellipsoid must be less than or equal to a constant. Excess path length is defined as the path length of the multipath minus the path length of the line-of-sight component. As described in previous sections, the variance of a link's RSS is highly related to the power contained in the multipath components affected by motion. With this reasoning, we make the assumption that motion occurring on voxels within an ellipsoid will contribute significantly to a link's RSS variance,

while motion in voxels outside will not. This is a binary quantization, but provides a simple, single-parameter spatial model. We note that measurements in [11, 18] also show elliptical-shaped areas in which motion causes high variance.

The variance weight for each voxel decreases as the distance between two nodes increases. As the link gets longer, the amount of power in the changing multipath components is decreased along with the link's RSS variance. Many models for distance weighting could be applied for images with varying qualities, but our empirical tests have indicated that dividing the variance weighting by the root of the link distance generates images that contain a balance of contrast and noise-reduction. The weighting is described mathematically as

$$[W]_{l,j} = \frac{1}{\sqrt{d_l}} \begin{cases} \psi & \text{if } d_{lj}(1) + d_{lj}(2) < d_l + \lambda \\ 0 & \text{otherwise} \end{cases} \quad (4.12)$$

where d_l is the distance between the two nodes, $d_{lj}(1)$ and $d_{lj}(2)$ are the distances from the center of voxel j to the two respective node locations on link l , ψ is a constant scaling factor used to normalize the image, and λ is a tunable parameter describing the excess path length included in the ellipsoid.

The normalized ellipse weight model is certainly an approximation, but experimental data has shown its effectiveness for VRTI, as will be shown in Section 4.6. Future work will use theoretical arguments and extensive measurements to refine the statistical models of RSS variance as a function of location.

4.4.5 Process Sampling, Buffering, and Variance Estimation

In this paper, we assume that the link signal strength process is sampled at a constant time period T_s , resulting in the discrete-time signal for link l :

$$R_l[k] = R_{dB_l}(kT_s). \quad (4.13)$$

where $R_{dB_l}(kT_s)$ is the RSS measurement in dB at time kT_s for link l . We also assume that the process remains wide-sense stationary for a short period of time. These assumptions allow the recent variance of the process to be estimated from a history buffer of the previous N_B samples for each link. The short-term unbiased sample variance \hat{s}_l for each link l is computed by

$$\hat{s}_l = \frac{1}{N_B - 1} \sum_{p=0}^{N_B-1} (R_l[k-p] - \bar{R}_l[k])^2 \quad (4.14)$$

where

$$\bar{R}_l[k] = \frac{1}{N_B} \sum_{p=0}^{N_B-1} R_l[k-p] \quad (4.15)$$

is the mean of the signal strength buffer. The sample variance vector for all links in the wireless network is

$$\hat{\mathbf{s}} = [\hat{s}_1, \hat{s}_2, \dots, \hat{s}_M]^T \quad (4.16)$$

4.4.6 Regularization and Image Estimation

The linear model (4.4) provides a mathematical framework relating movement in space to a link's RSS variance. The model is an ill-posed inverse problem that is highly sensitive to measurement and modeling noise. No unique solution to the least-squares formulation exists, and regularization must be applied to obtain a solution. In this paper, *Tikhonov* regularization is used, but other common forms of regularization as they apply to RTI are discussed and evaluated in [16].

In Tikhonov least-squares regularization, the optimization for image estimation is formulated as

$$\mathbf{x}_{Tik} = \arg \min_{\mathbf{x}} \frac{1}{2} \|\mathbf{W}\mathbf{x} - \hat{\mathbf{s}}\|^2 + \alpha \|\mathbf{Q}\mathbf{x}\|^2 \quad (4.17)$$

where \mathbf{Q} is the *Tikhonov matrix* that enforces a solution with certain desired properties, and α is a tunable regularization parameter. Taking the derivative of (4.17) and setting to zero results in the solution:

$$\mathbf{x}_{Tik} = (\mathbf{W}^T \mathbf{W} + \alpha \mathbf{Q}^T \mathbf{Q})^{-1} \mathbf{W}^T \hat{\mathbf{s}}. \quad (4.18)$$

Tikhonov regularization provides a simple framework for incorporating desired characteristics into the VRTI reconstruction. If smooth images are desired, a difference matrix approximating the derivative of the image can be used as the Tikhonov matrix. If the image is two dimensional, the regularization should include the difference operations in both the vertical and horizontal directions. Let \mathbf{D}_x be the difference operator for the horizontal direction, and \mathbf{D}_y be the difference operator for the vertical direction. Then the Tikhonov regularized least-squares solution is

$$\mathbf{x}_{Tik} = \Pi \hat{\mathbf{s}}. \quad (4.19)$$

$$\Pi = [\mathbf{W}^T \mathbf{W} + \alpha(\mathbf{D}_x^T \mathbf{D}_x + \mathbf{D}_y^T \mathbf{D}_y)]^{-1} \mathbf{W}^T$$

In summary, the variance of each link is estimated from a recent history of RSS samples and stored in vector $\hat{\mathbf{s}}$. The regularized image solution is simply a linear transformation Π of this vector $\hat{\mathbf{s}}$.

4.5 Kalman Filter Tracking

A radio tomography image in itself does not provide the location coordinates of moving objects. The Kalman filter provides a framework to track such coordinate estimates. Kalman filters are used extensively to estimate the hidden state of a system when measurements of that state are linear and have been corrupted by Gaussian noise. It takes into account the current and previous measurements to generate a more accurate estimate of the system's state than a single instantaneous measurement can. A Kalman filter also has the desirable characteristic that the estimate can be updated with each new measurement, without the need to perform batch measurement collection and processing.

In a location tracking system, such as the one described in this paper, the state to be estimated is made up of the physical coordinates of the object being tracked. The Kalman filter exploits the fact that an object moves through space at a limited speed, smoothing the effects of noise and preventing the tracking from “jumping.” In this sense, the filter can be viewed as a form of regularization.

In this work, the objects being tracked are assumed to move as a Brownian process, and measurement noise is assumed to be Gaussian. Although these assumptions are not entirely accurate, the Kalman filter is still effective for tracking the location of movement. The following variables are used in the tracking filter.

- v_m^2 : the variance of the object's motion process, indicating how fast the object is capable of moving. Larger values enable the filter to track faster moving objects, but also make the estimate noisier.
- v_n^2 : the variance of the measurement noise. Larger values will cause the filter to “trust” the statistical predictions over the instantaneous measurements.

With these assumptions and variables, the Kalman filter algorithm for tracking movements in an RTI system can be described by the following steps.

1. Initialize $\mathbf{c} = (0, 0)$ and $\mathbf{P} = \mathbf{I}_2$, where \mathbf{I}_2 is the 2x2 identity matrix.
2. Set $\bar{\mathbf{P}} = \mathbf{P} + v_m^2 \mathbf{I}_2$.
3. Set $\mathbf{G} = \bar{\mathbf{P}}(\bar{\mathbf{P}} + v_n^2 \mathbf{I}_2)^{-1}$.
4. Take measurement \mathbf{z} equal to the coordinates of the maximum of the VRTI image.
5. Set $\mathbf{c} = \mathbf{c} + \mathbf{G}(\mathbf{z} - \mathbf{c})$.
6. Set $\mathbf{P} = (\mathbf{I}_2 - \mathbf{G})\bar{\mathbf{P}}$.
7. Jump back to step 2 and repeat.

For information on the derivation of this algorithm, there are many textbooks on the topic of Kalman filtering [70], [71].

4.6 Experiment

4.6.1 Description and Layout

This section presents the results of a through-wall tracking experiment utilizing variance-based RTI. A 34-node peer-to-peer network was deployed in an area around a four-wall portion of a typical home. Three of the walls are external, and one is located on the interior of the home. The interior wall is made of brick and was an external wall prior to remodeling of the home. Objects like furniture, appliances, and window screens were not removed from the home to ensure that the tracking was functional in a natural environment.

The nodes were placed in a rectangular perimeter, as depicted in Figure 4.2. It was neither possible, nor necessary, to place the nodes in a uniform spacing due to building and property obstacles. Eight of the nodes were placed on the inside of the building, but on the other side of the brick interior wall. Each radio was placed on a stand to keep them on the same two-dimensional plane at approximately human torso level.

The nodes utilize the IEEE 802.15.4 protocol, and transmit in the 2.4GHz frequency band. To avoid network transmission collisions, a simple token passing protocol is used. Each node is assigned an ID number and programmed with a

known order of transmission. When a node transmits, each node that receives the transmission examines the sender identification number. The receiving nodes check to see if it is their turn to transmit, and if not, they wait for the next node to transmit. If the next node does not transmit, or the packet is corrupted, a timeout causes each receiver to move to the next node in the schedule so that the cycle is not halted. A base-station node that receives all broadcasts is used to gather signal strength information and save it to a laptop computer for real-time processing.

In all the experimental results in this section, the same set of image reconstruction parameters is used, as shown in Table 4.1.

Shadowing-based RTI [15] uses the difference in average signal strength to image the attenuation caused by objects in a wireless network. In through-wall imaging, however, the effect of dense walls prevent many of the links from experiencing significant path loss due to a single human obstructing the link. In many cases, multipath fading can cause the signal strength to increase when a human obstructs a link.

Variance can be used as an indicator of motion, regardless of the average path loss that occurs due to dense walls and stationary objects within the network. An example of how through-wall links are affected by obstruction is provided in Figure 4.3. When a stationary object obstructs the link in a through-wall environment, the change in mean RSS is unpredictable. For example, in Fig 4.3, one link appears unaffected by the obstruction, while another link's RSS average is raised by approximately 4 dB. When an object moves, the variance of the obstructed link's RSS provides a more reliable metric, as seen in the figure.

4.6.2 Image Results

To further demonstrate the advantage of using VRTI over shadowing-based RTI for through-wall motion imaging, two images are presented in Fig. 4.8 and Fig. 4.8. In both images, a human moves randomly, taking small steps around and through the space directly above the coordinate. This is necessary since VRTI images movement, not static changes in attenuation.

Inspection of the figures shows that VRTI is capable of imaging areas of motion behind walls, while conventional RTI fails to image the change in attenuation. These

results are typical of other location coordinates tested during the experiment.

Tracking multiple moving targets through dense walls is a challenging and open topic for future research. When multiple people move within a surveillance area, the accuracy of a VRTI image is dependent on the separation of the targets. Additionally, when multiple walls or walls constructed with dense materials surround the surveillance area, the amount of power that radiates into the area is reduced. Systems attempting to track movement in these difficult circumstances may require low radio frequencies and directional antennas to achieve usable results.

4.6.3 Path Tracking

In this section, we test our tracking system with experimental data. An experimenter moves at a typical walking pace on a pre-defined path at a constant speed. A metronome and uniformly placed markings on the floor help the experimenter to take constant-sized steps at a regular time interval. The experimenter's actual location is interpolated using the start and stop time, and the known marker positions.

The location of the experimenter is estimated using the Kalman filter described in Section 4.5 with imaging parameters presented in Table 4.1. Figs. 4.8, 4.8, 4.8 and 4.8 plot both the known and estimated location coordinates over time when using two different mobility parameters.

The effect of the tracking parameters is visually evident in the figures. When the mobility parameter is set high, the filter is able to track the human with less lag, but the variance of the estimate also increases. When the mobility parameter is set low, the tracking coordinate severely lags behind the moving object, but estimates a smoother path of motion.

To quantify the accuracy of the location coordinate estimation, the average error is defined as

$$\epsilon = \frac{1}{L} \sum_{k=1}^L \sqrt{(z_x[k] - p_x[k])^2 + (z_y[k] - p_y[k])^2} \quad (4.20)$$

where L is the total number of samples, $z_x[k]$ and $z_y[k]$ are the estimated x and y coordinates at sample time k , and $p_x[k]$ and $p_y[k]$ are the actual known coordinates. The average tracking error for $v_m^2 = .01$ and $v_n^2 = 5$ is 2.07 feet.

It should be noted that a Kalman filter can be designed to estimate the target's velocity, as well as position. This would enable the filter to follow a non-accelerating moving object without a lag. However, when a target changes direction or speed, some transient error would occur while the filter converges to the new speed and direction.

4.6.4 Spot Movement

When estimating the location of a moving object, some amount of tracking lag must occur due to the time it takes to collect measurements from the network and the processing delays. The lag is also dependent on the mobility parameter v_m used for tracking.

To study the tracking system without the effects of time delay, the estimated and known location of a moving human are compared at 20 different coordinates. At each location, the experimenter moves randomly, taking small steps around and through the space directly above the known coordinate. The VRTI tracking system estimates the location of movement and we average the estimates over a duration of ten seconds for each coordinate. The average estimated coordinate is plotted with the known location to generate the results presented in Figure 4.10.

To quantify the accuracy in this test, the error for each of the 20 known coordinates is averaged.

$$\zeta = \frac{1}{20} \sum_{p=1}^{20} \epsilon_p \quad (4.21)$$

where ϵ_p is the average error defined by (4.20) for each position p . The error for this test with $v_m^2 = .01$ and $v_n^2 = 5$ is 1.46 feet.

4.6.5 Effect of Imaging Parameters on Tracking Accuracy

The RTI parameters shown in Table 4.1 must be chosen appropriately, as they affect the accuracy of tracking. The elliptical width parameter λ , regularization parameter α , and buffer size N_B are especially important, as the other parameters for pixel size and scaling are mostly arbitrary.

The elliptical width parameter λ is important to minimize modeling error and maximize tracking performance. If the weighting ellipse is set too large, motion from objects within the ellipsoid will not contribute significantly to the variance of

the corresponding link, and contrast in the VRTI result will be lost. If the ellipse is set too narrow, motion outside the ellipsoid will contribute significantly to the pixels that are inside, resulting in images with many false bright spots. Figure 4.8 shows the average tracking error ϵ in feet for three buffer sizes over a range of elliptical width parameter values. In this experiment, the most accurate tracking was accomplished with λ set to approximately 0.1.

The amount of regularization applied to the imaging can significantly affect the accuracy of tracking. If regularization is set too low, sharp noise will corrupt the images and cause the tracking mechanism to jump to erroneous locations. If the images are over-regularized, the images become too flat and smooth, causing the tracking mechanism to drift in a large circle around the target position. Figure 4.8 shows the average tracking error ϵ in feet for three buffer sizes over a range of regularization parameter values. In this experiment, the most accurate tracking was accomplished with $\alpha = 100$.

The variance buffer size plays an important role in tracking accuracy. When N_B is very low, a very small amount of data is used for the variance calculation, and the VRTI images are highly susceptible to noise and modeling error. When the buffer sizes are too large, the VRTI images are blurred by the motion of the targets, and tracking lag increases. The most accurate tracking is achieved when there is a balance of the two extremes. Figure 4.8 shows the average tracking error ϵ in feet for three regularization values over a range variance buffer values. In this experiment, the most accurate tracking was accomplished with buffer size $N_B = 50$.

4.7 Future Research

Many areas of future research are possible to improve VRTI through-wall tracking technology. First, improvements to the multipath models will allow a system to track multiple individuals more accurately, and with less nodes. Many of the assumptions presented in this paper are accurate only for cases where motion images are sparse. More accurate statistical models of the multipath channel for device-free localization will be needed to track multiple people that move in close proximity.

Wireless protocol research is another important part of the improvement of VRTI. Large and scalable networks capable of tracking entire homes and buildings

need to be explored. This will require advanced wireless networking protocols that can measure the RSS of each link quickly when the number of nodes is high. Perhaps frequency hopping and grouping of nodes will allow a VRTI system to measure each link's RSS while maintaining a low delay in delivering the measurements to a base station.

Advancements on the physical layer modeling will allow VRTI systems to track movement more accurately, and with less nodes. In this paper, an ellipsoid model is used to relate RSS variance on a link to the locations of movements. This is certainly an approximation, and future work will require the refinement of the variance weighting model, thus leading to more accurate motion images and coordinate tracking. Other regularization and image estimation techniques may also improve through-wall tracking.

Radio devices could be designed specifically for VRTI tracking applications. The affect of overall node transmission power on imaging performance is an important area to be investigated. Directional and dual-polarized antenna designs would most likely improve images in a through-wall VRTI system. Radio devices capable of sticking to an exterior wall and directionally transmitting power into the structure would be extremely useful in emergency deployment and multi-story VRTI.

Finally, localization of nodes plays a significant role in tracking of motion with VRTI networks. In an emergency, rescue or enforcement teams will not have time to survey a location. With automatic node self-localization techniques, the nodes could be thrown or randomly placed around an area without measurement, thus saving valuable time.

4.8 Conclusion

Locating interior movement from the outside of a building is extremely valuable because it enables police, military forces, and rescue teams to make life-saving decisions. Variance-based radio tomography is a powerful new method for through-wall imaging that can be used to track the coordinates of moving objects. The cost of VRTI hardware is very low in comparison to existing through-wall imaging systems, and a single network is capable of tracking large areas. These features may enable many new applications that are otherwise impractical.

This paper discusses how RSS variance relates to the power contained in multipath components affected by moving objects. The variance of RSS is related to the location of movement relative to node locations, and this paper provides a formulation to estimate a motion image based on variance measurements. The Kalman filter is applied as a mechanism for tracking movement coordinates from image data. A 34-node VRTI experiment is shown to be capable of tracking a moving object through typical home exterior walls with an approximately two foot average error. An object moving in place can be located with approximately 1.5ft average error.

The experiments presented in this paper demonstrate the theoretical and practical capabilities of VRTI for tracking motion behind walls. Many avenues for future research are presented which may improve image accuracy and enable larger and faster VRTI networks. These future research areas include wireless protocols, antenna design, radio channel modeling, localization, and image reconstruction.

Table 4.1. VRTI image reconstruction parameters

Parameter	Value	Description
Δ_p	1.5	Pixel width (ft)
λ	.1	Width parameter of weighting ellipse (ft)
α	100	Regularization parameter
ψ	60	Variance weighting scale $(dB)^2$
N_B	50	Length of RSS buffer

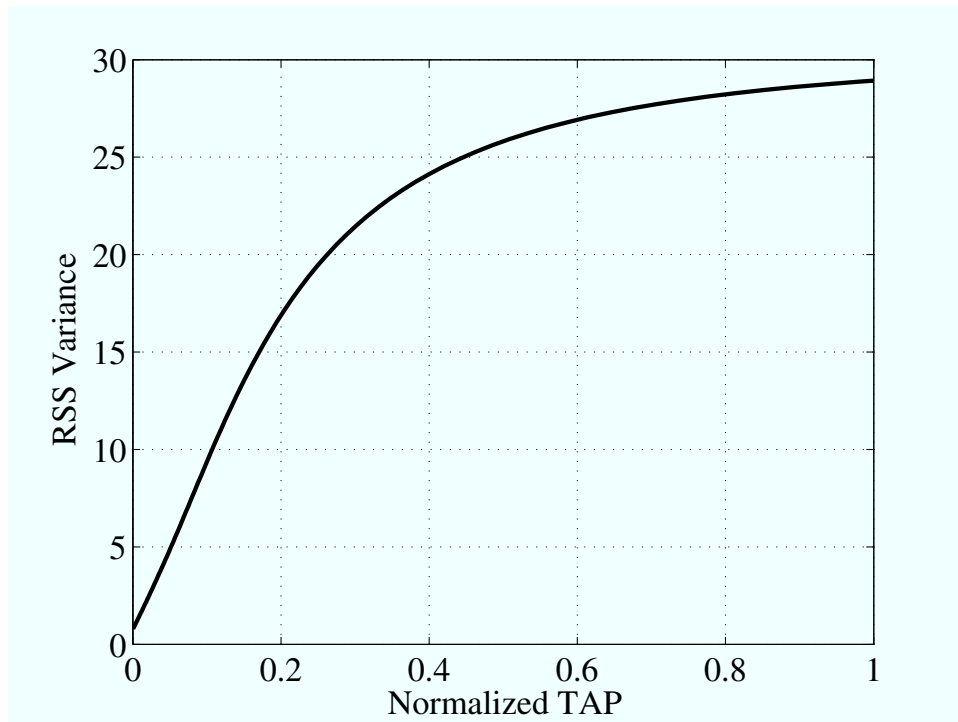


Figure 4.1. The variance of RSS vs. normalized TAP, $T_{AP}(\mathbf{x})/\bar{V}^2$, for $\sigma_\nu^2/\bar{V}^2 = 0.01$.

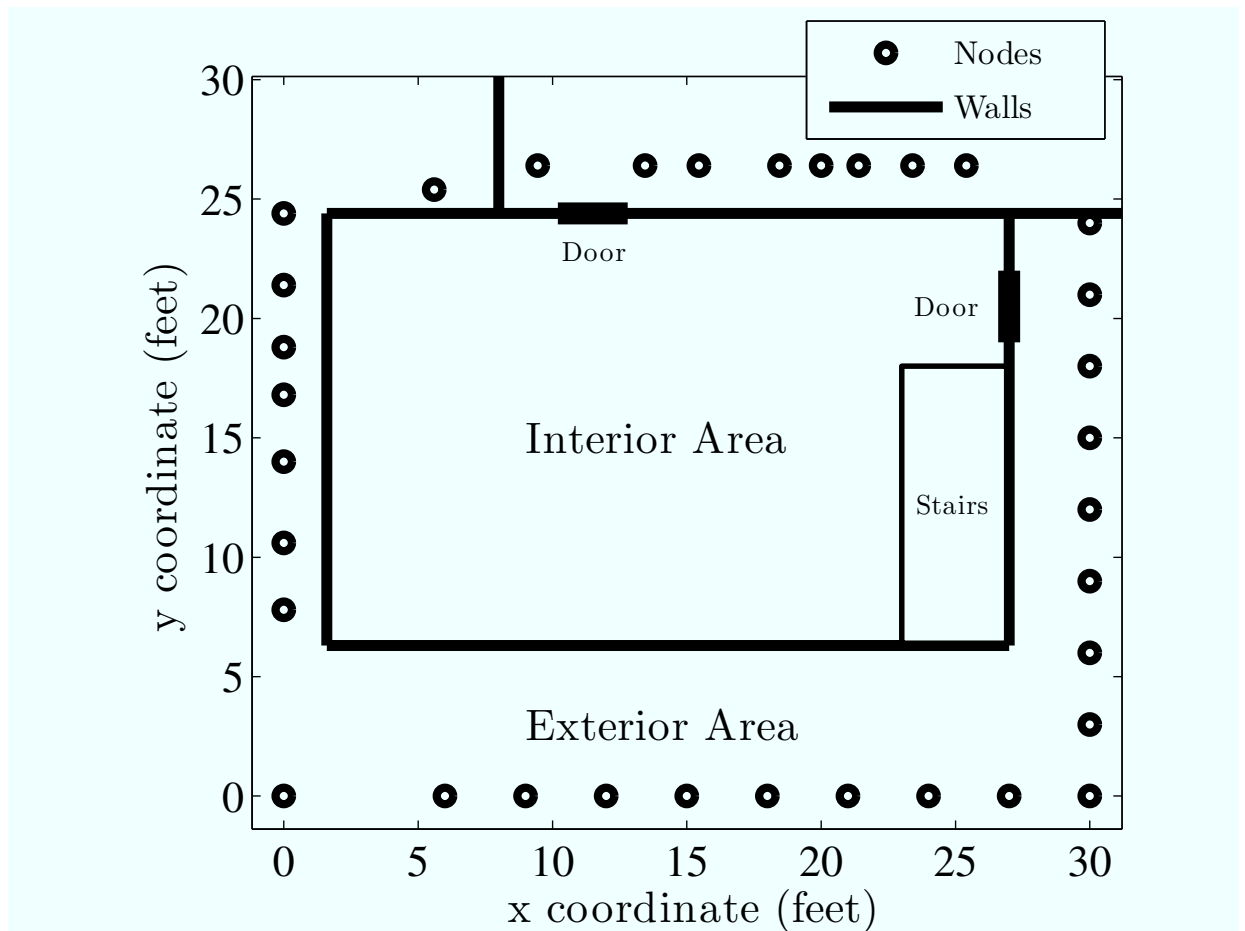


Figure 4.2. The layout of a 34-node variance-based RTI through-wall tracking experiment.

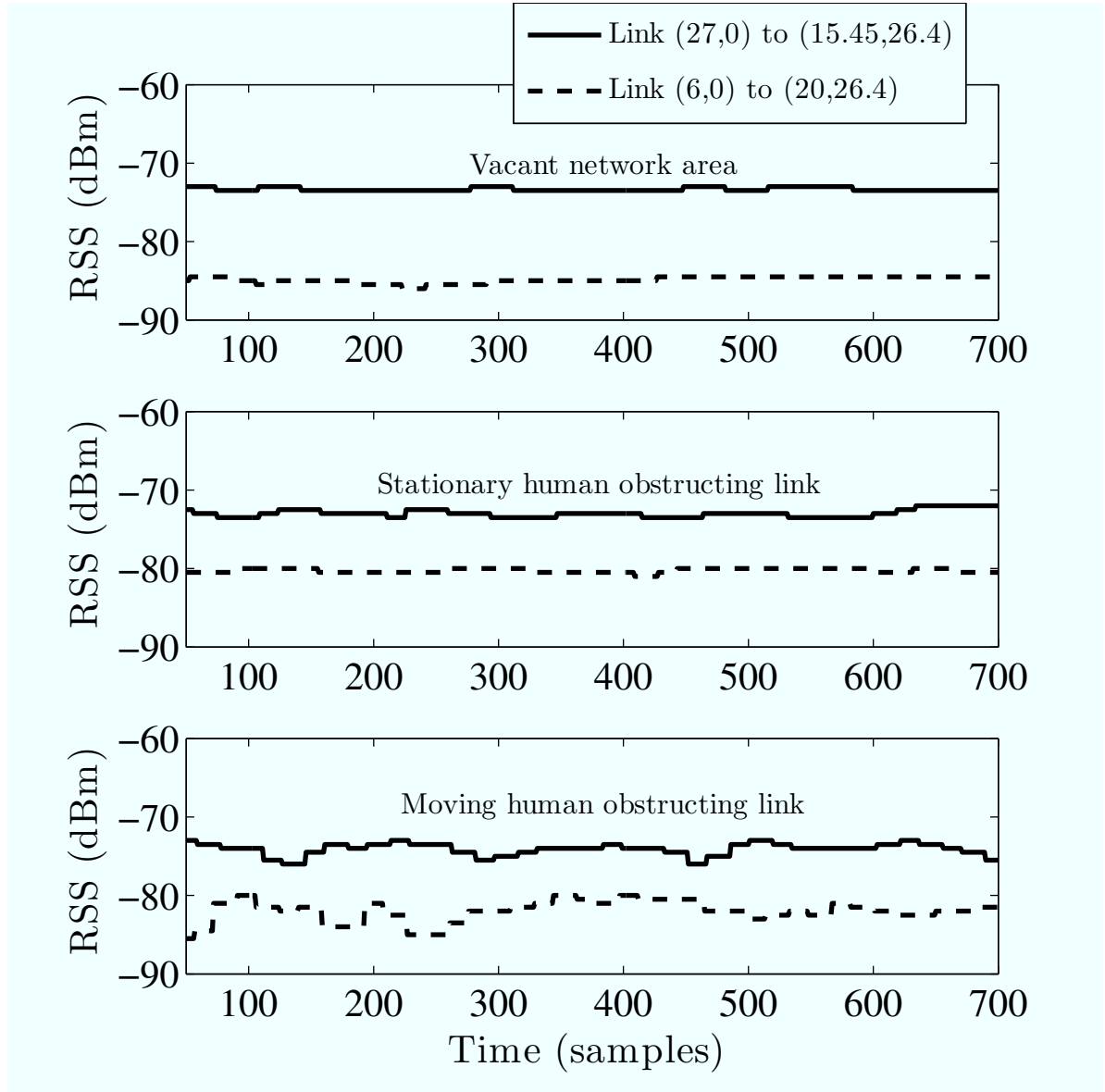


Figure 4.3. RSS measurements for two links in a through-wall wireless network. Comparison of these signals illustrates the advantage of using variance over mean for through-wall imaging of human motion.

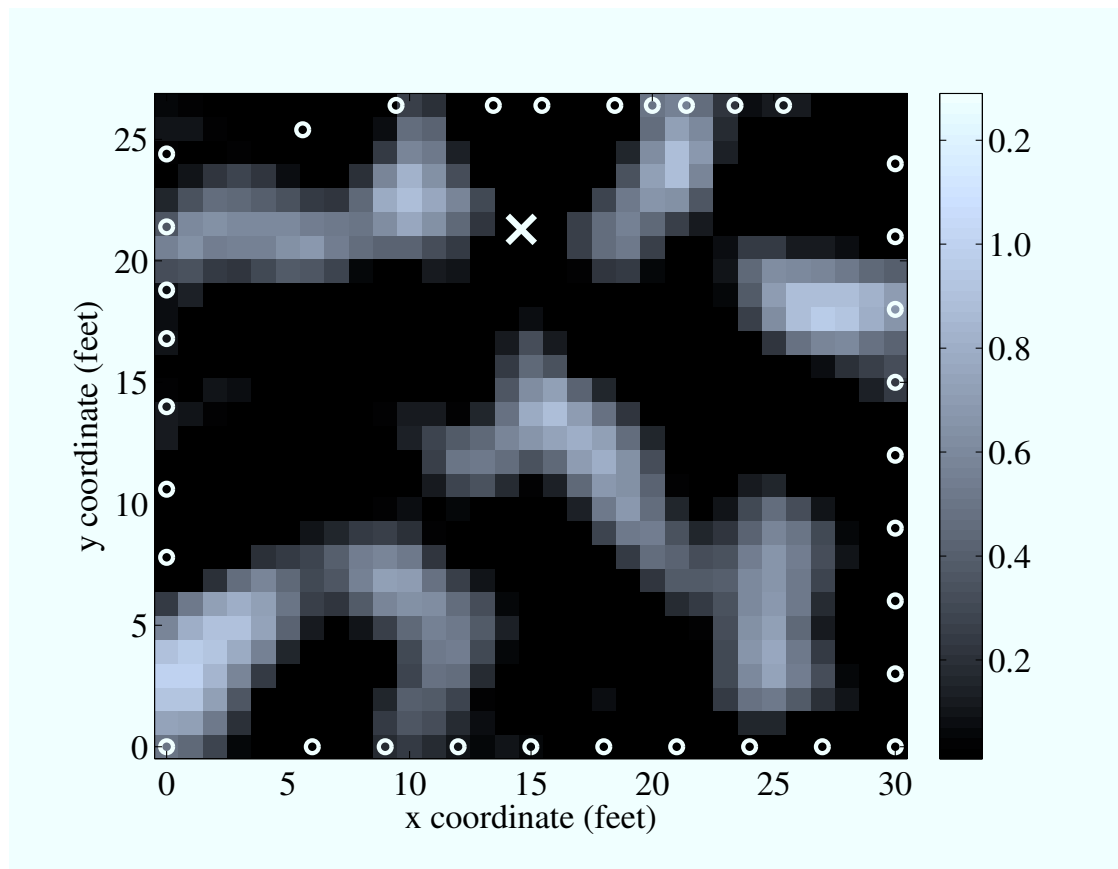


Figure 4.4. Shadowing-based RTI results for through-wall imaging. The experimenter is moving at coordinate (14.6,21.3).

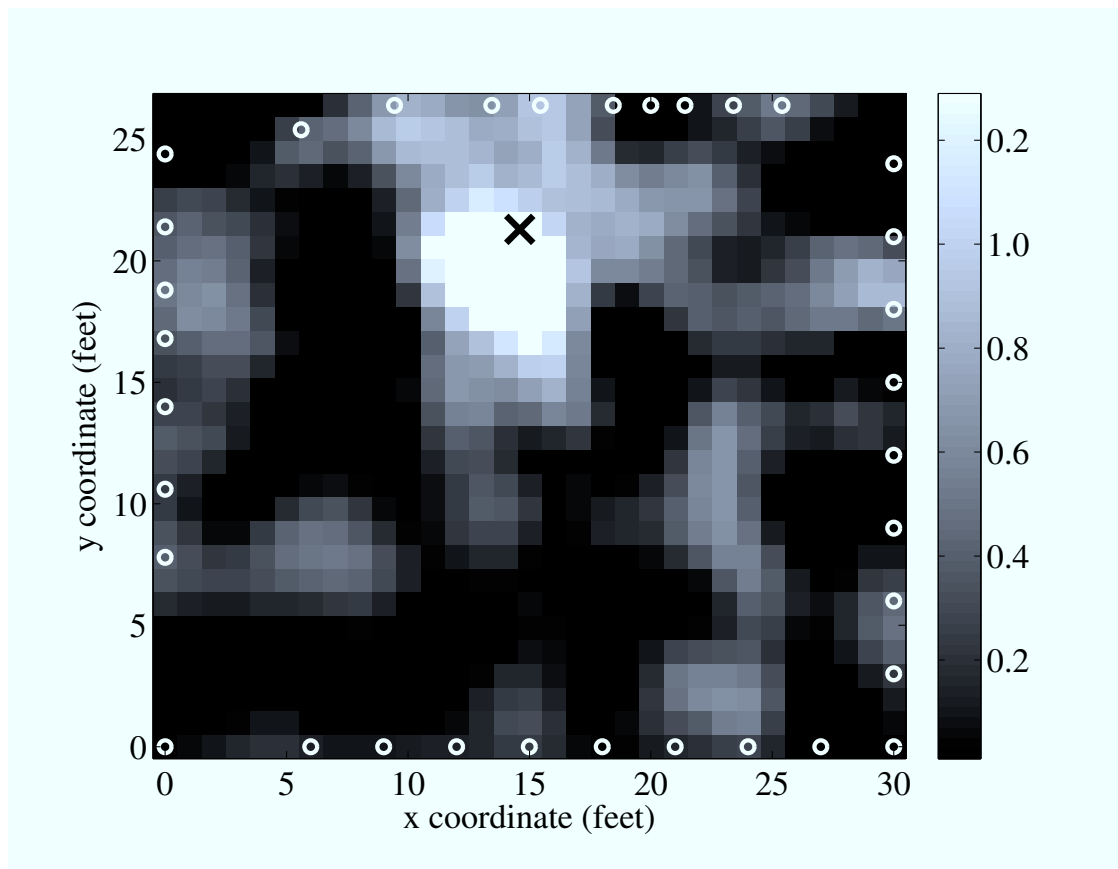


Figure 4.5. Variance-based RTI results for through-wall imaging. The experimenter is moving at coordinate (14.6,21.3).

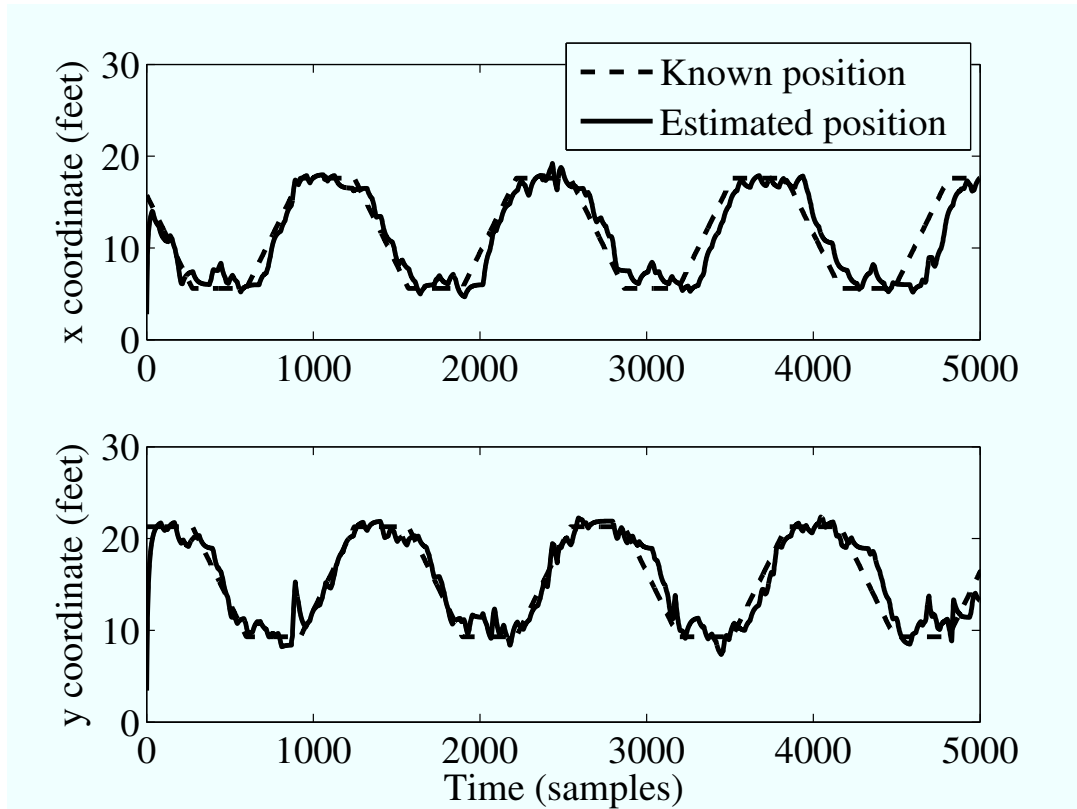


Figure 4.6. The location of human movement moving along a known rectangular path is estimated using constant $v_n^2 = 5$. Here, the mobility v_m is set empirically to track objects moving at a few feet per second.

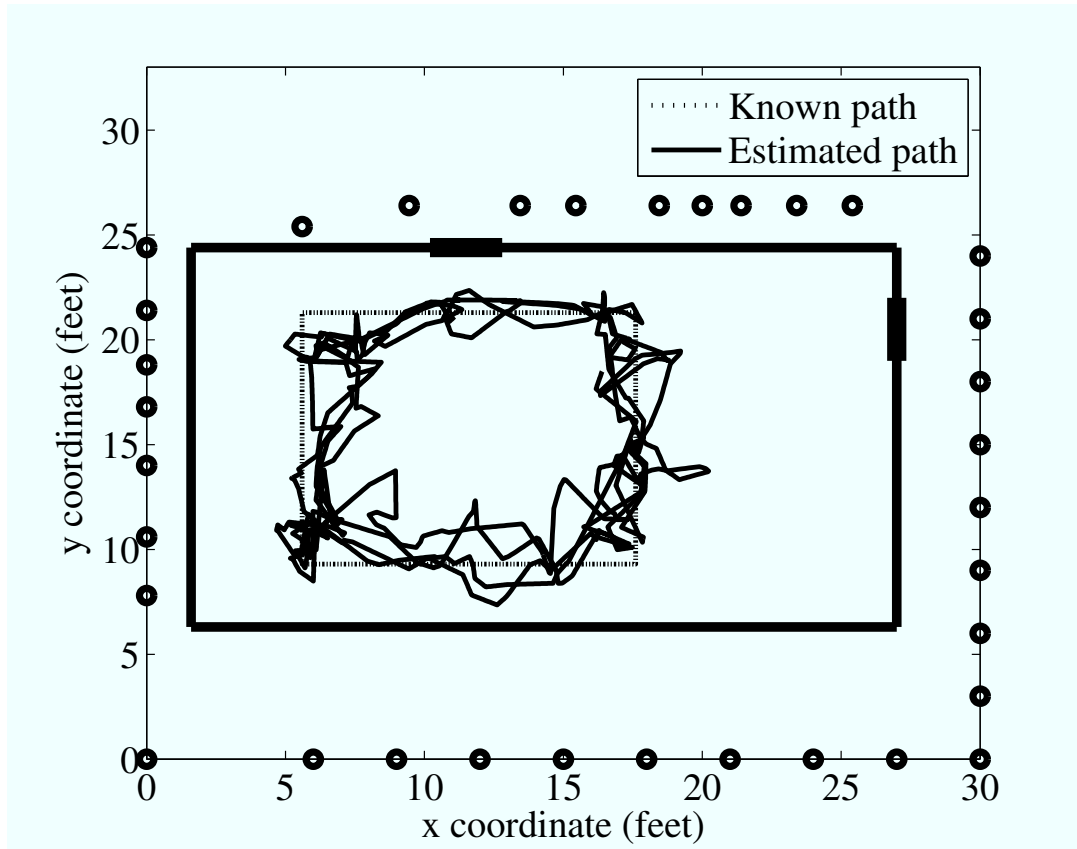


Figure 4.7. The location of human movement moving along a known rectangular path is estimated using constant $v_n^2 = 5$. Here, the mobility v_m is set empirically to track objects moving at a few feet per second.

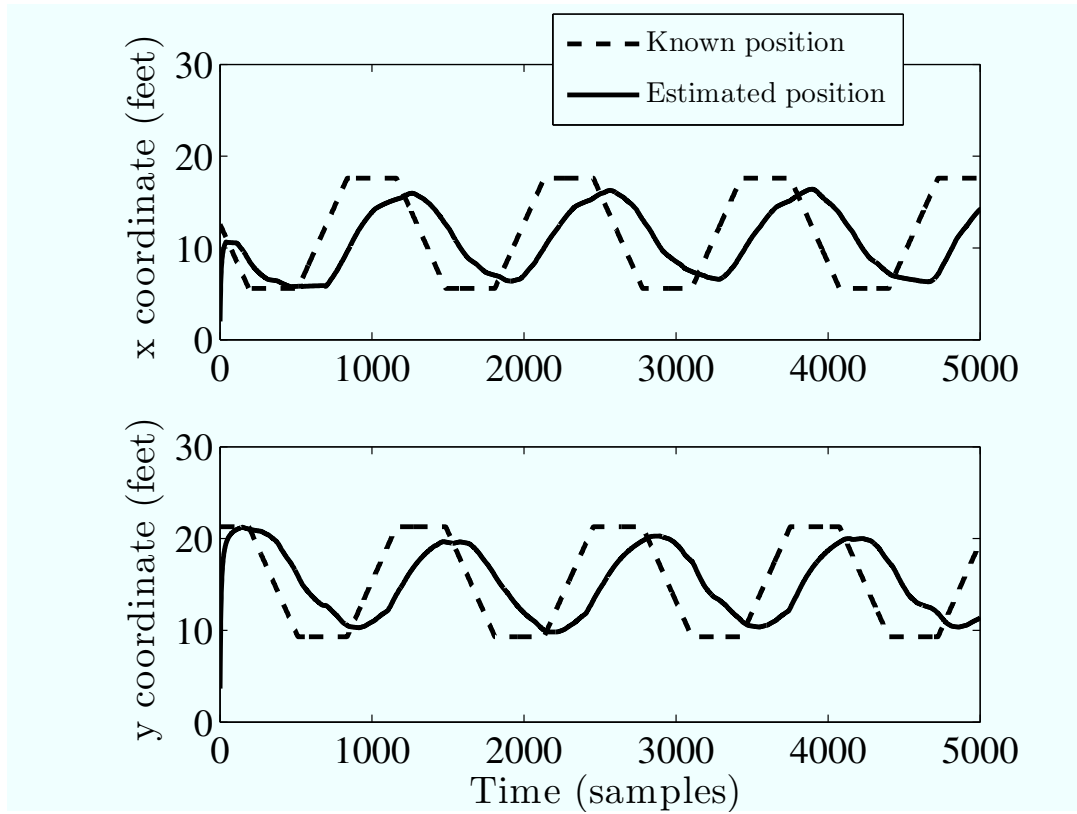


Figure 4.8. The location of human movement moving along a known rectangular path is estimated using constant $v_n^2 = 5$. Here, the mobility v_m is set too low, causing the tracking filter to lag excessively.

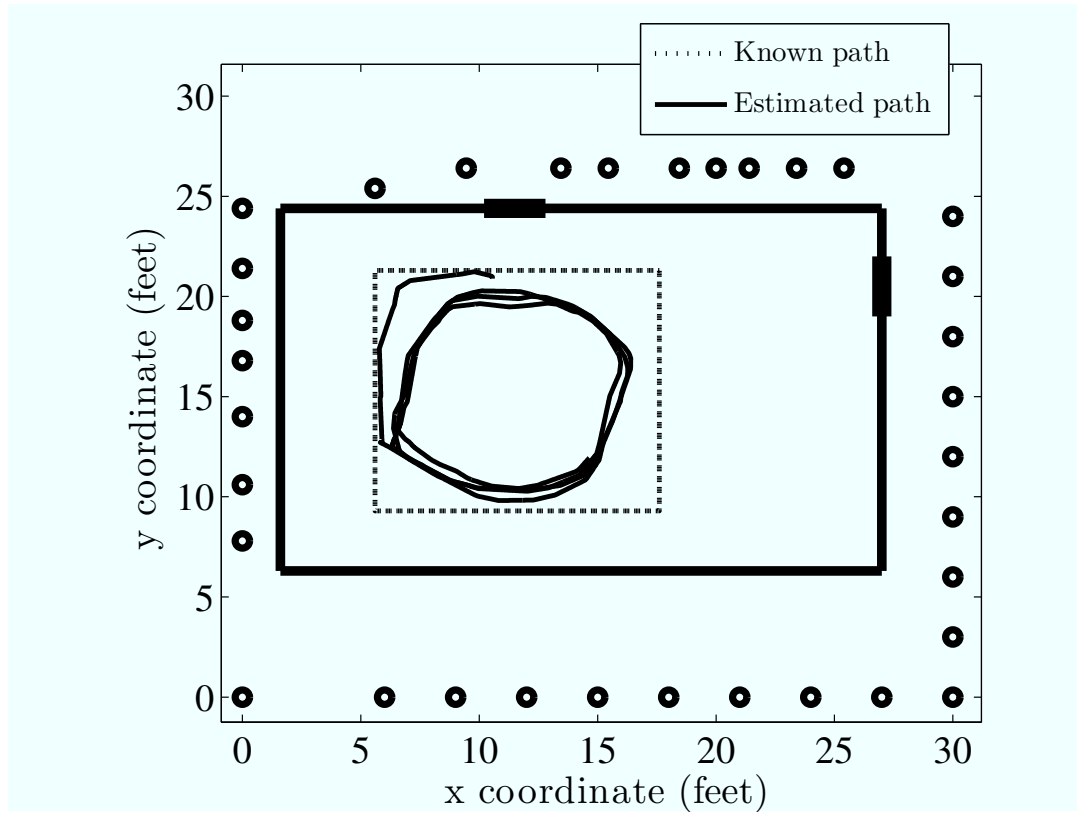


Figure 4.9. The location of human movement moving along a known rectangular path is estimated using constant $v_n^2 = 5$. Here, the mobility v_m is set too low, causing the tracking filter to lag excessively.

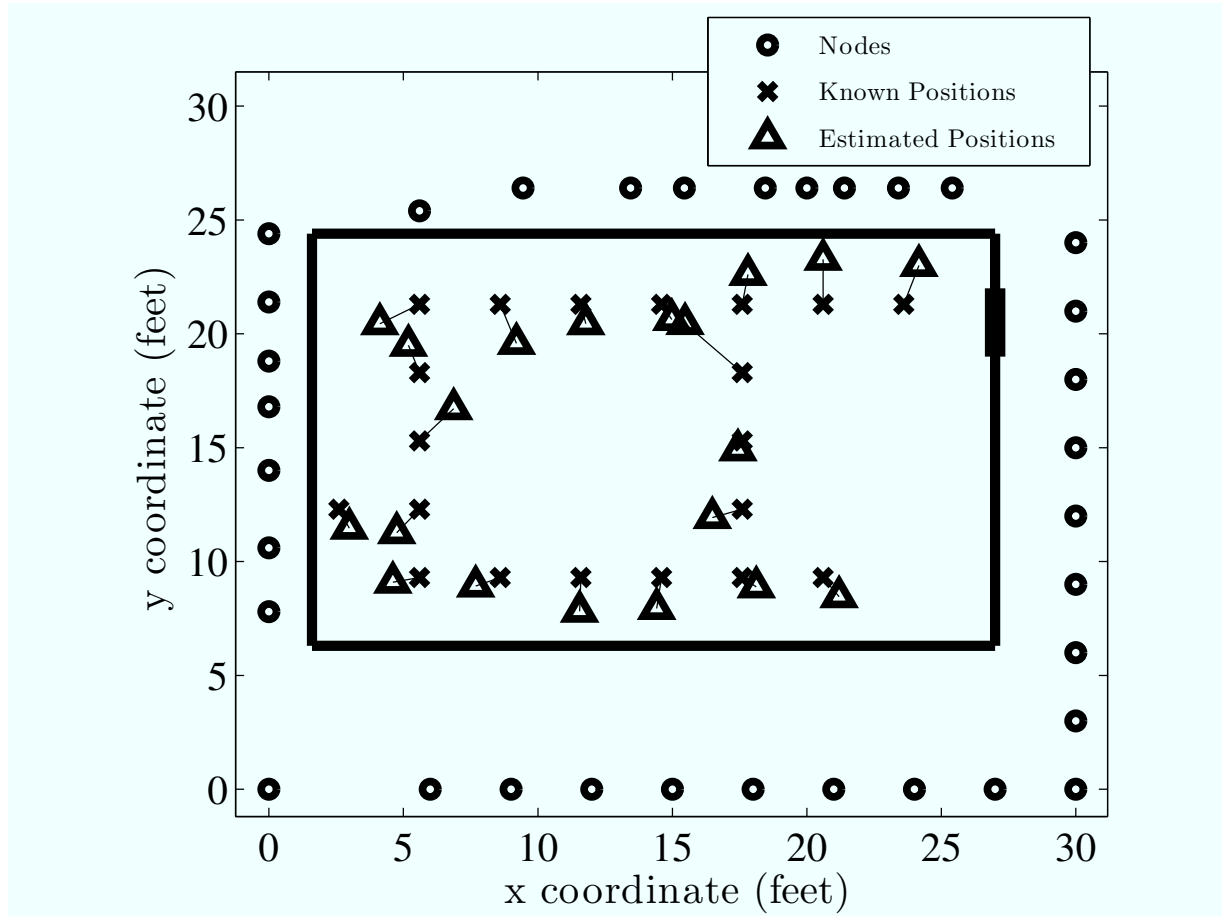


Figure 4.10. The ten-second average locations of human movement over 20 known positions is estimated using VRTI and Kalman filter tracking with parameters $v_m^2 = .01$ and $v_n^2 = 5$. The average error for this experiment $\zeta = 1.46$ feet.

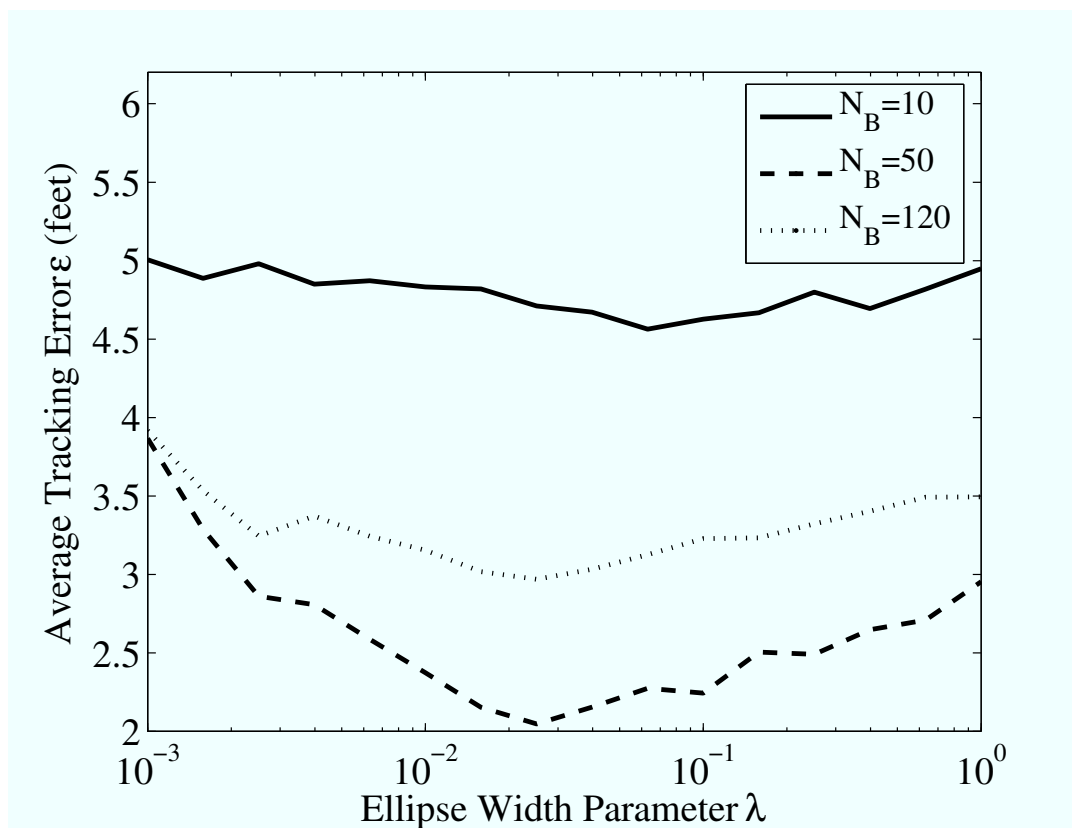


Figure 4.11. Effect of ellipse width λ on average tracking error ϵ . Other parameters are equal to those shown in Table 4.1.

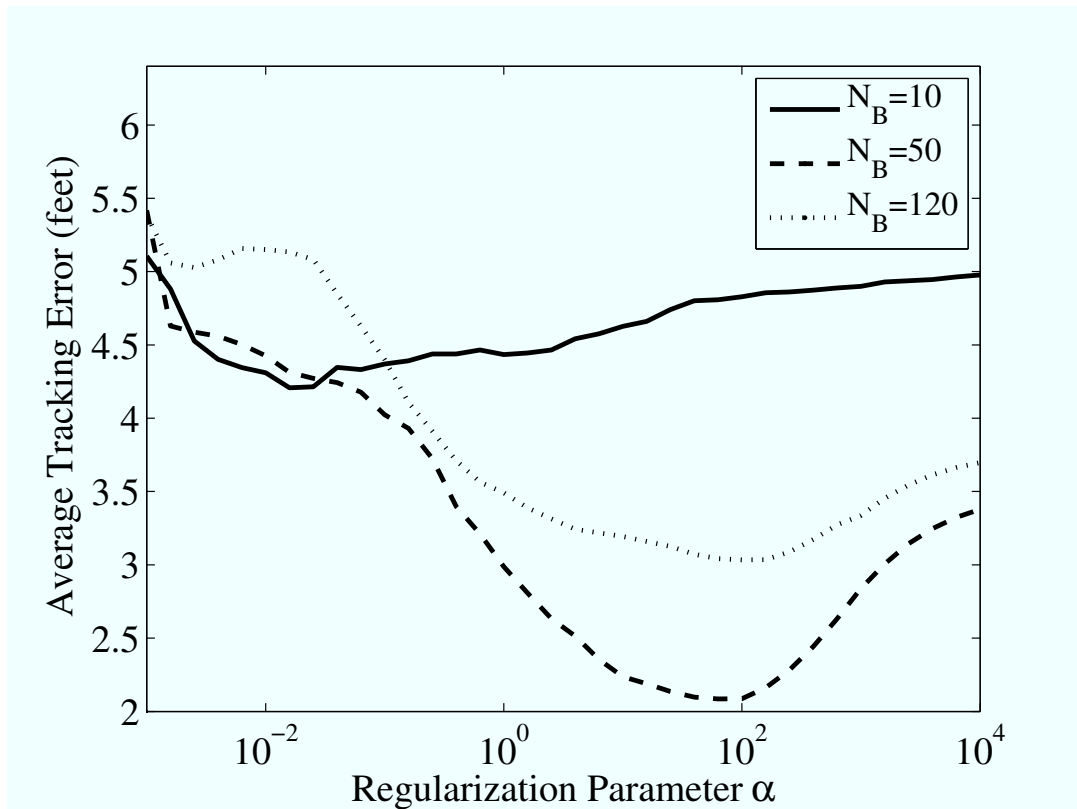


Figure 4.12. Effect of regularization parameter α on average tracking error ϵ . Other parameters are equal to those shown in Table 4.1.

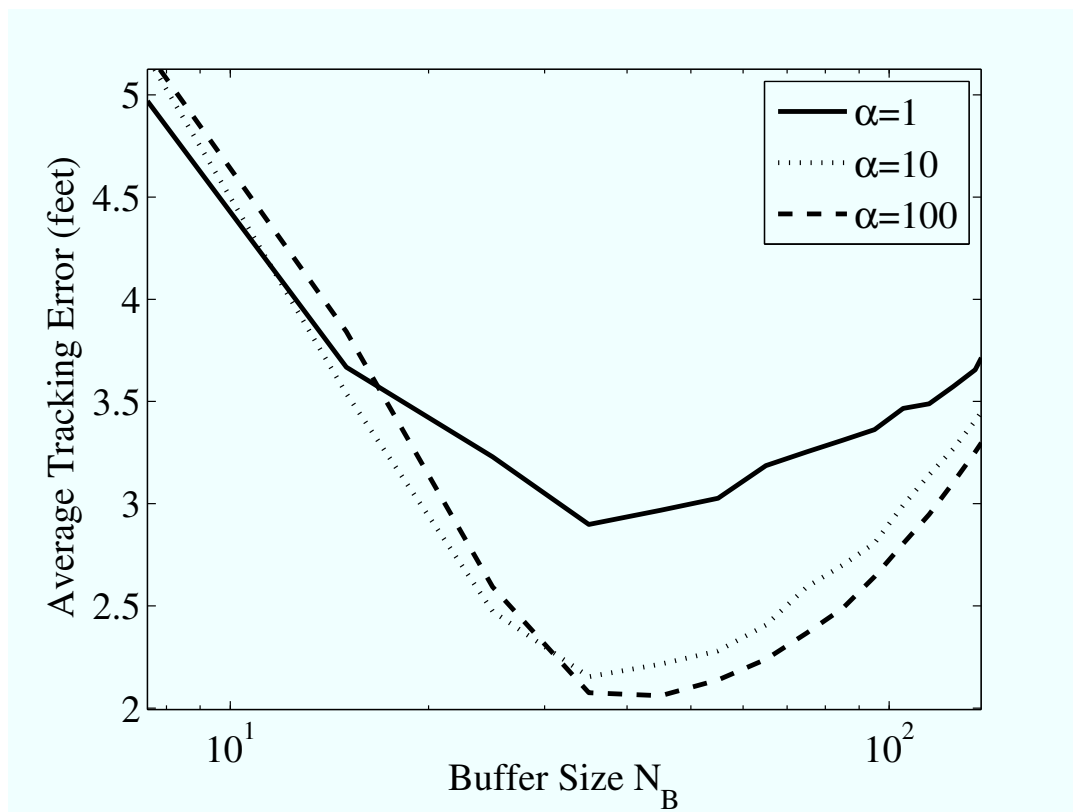


Figure 4.13. Effect of buffer size N_B on average tracking error ϵ . Other parameters are equal to those shown in Table 4.1.

CHAPTER 5

A STATISTICAL INVERSION METHOD AND MODEL FOR DEVICE-FREE LOCALIZATION IN RF SENSOR NETWORKS

5.1 Abstract

Device-free localization is the estimation of the position of a person or object that does not carry any electronic device or tag. This paper introduces measurement-based statistical models that can be used to estimate the locations of people using signal strength measurements in wireless networks. We demonstrate, using extensive experimental data, that changes in signal strength measurements due to human motion can be modeled by the skew-Laplace distribution. The parameters of the distribution are dependent on the position of person and on the amount of fading that a particular link experiences. Using the skew-Laplace likelihood model, we apply a particle filter to experimentally estimate the location of moving and stationary people through walls, with accuracies of approximately one meter.

5.2 Introduction

Knowing the location of people is extremely valuable and useful. Global positioning systems (GPS), radio frequency identification (RFID) and real-time location systems (RTLS) have proven their value for locating targets with an attached device. Device-free localization (DFL) is the practice of locating people¹ or objects when no tag or device is attached to the entity being located. DFL technologies are therefore useful in applications like security, where the people being tracked can not be expected to cooperate with the system. In this paper, we investigate a

¹In this paper, we use the word “people” generally to refer to either people or objects that are to be located and tracked.

statistical inversion method for DFL in narrowband RF sensor networks, and show its effectiveness in tracking objects located behind walls.

Various sensor technologies can be used for the purposes of DFL [8], as discussed in Section 5.6. In this paper, we are particularly interested in DFL systems which use received signal strength (RSS) measurements (RSS-DFL) because RSS can be measured with a variety of widely-deployed and inexpensive wireless devices. RSS-DFL can locate motion through building walls [17], in dark or smoke-filled environments, and are not as invasive of privacy as video camera surveillance.

RSS-DFL systems have, to this point, significant limitations. Imaging-based RSS-DFL systems first estimate attenuation or motion image and then estimate the person's coordinate from that image [17], and information can be lost in the two-step process. In particular, variance-based radio tomographic imaging (VRTI) cannot be used to locate a stationary (or very slow-moving) person. Fingerprint-based RSS-DFL systems require extensive calibration measurements [13, 21]. To date, direct coordinate estimation in RSS-DFL is ad hoc and does not consider the statistics of the RSS measurements [11, 18].

To provide a means to address these significant limitations, in this paper, we present a new statistical inversion method for RSS-DFL in wireless networks. The new model allows for direct estimation of a target's position, without the need to use radio tomographic images as an intermediate information layer.

This statistical inversion method is enabled by a new RSS model presented in this paper for temporal fading on static links. Significant statistical models exist for small-scale fading, or for the frequency-dependence of fading, this model represents an advance on two levels. First, the model presented is a function of the current position of a person – whether or not the person is now close to the link. Second, the model presented is a function of the *fade level*, that is, a quantification of the narrowband fading experienced on the static link prior to the person's appearance in the environment. Fade level is a measurable quantity in RSS-DFL. The new model takes advantage of the uniqueness of each link in the RF sensor network, as quantified by the fade level, rather than assuming each link behaves identically when people are located near a link. We show that links experience drastically different behavior dependent on its fade level.

Our model is empirical, based on extensive measurements presented in this paper conducted in two very different environments in which DFL systems are expected to operate. We find that the temporal variation of RSS is well-modeled with the skew-Laplace distribution. Our measurements quantify the relation between the parameters of the skew-Laplace distribution to a person's location and fade level.

Finally, we demonstrate the application of the skew-Laplace model in the statistical inversion method in a real-world system. We demonstrate that the method is able to locate even motionless people through external building walls, which had not been demonstrated in previous work. We show that moving people can be tracked with about 1 meter error in our experiment.

The statistical approach allows us to address some key limitations of previous RSS-DFL systems. Since the new method does not rely on manual site-specific measurements, it can be deployed at multiple sites without the need for offline training. The training, in essence, has already been performed in the modeling of the statistics. Furthermore, the new method does not require a specific network location geometry or regularity in the environment.

The statistical inversion process we propose is illustrated in Fig. 5.1. First, raw measurements are received at a base station processing unit. These measurements are combined with knowledge about the node locations to quantify the fade level F on each link, as well as the mean P_m of each link. This calibration information is used to determine a statistical likelihood model based on the skew-Laplace distribution, as discussed in a later section. The likelihood model provides the basis for particle filtering, a non-linear and non-Gaussian filter for recursive estimation, which is used to infer device-free location results.

5.3 Statistical Modeling

5.3.1 Overview

In general, a statistical likelihood model represents the noisy translation from a state space to a measurement space (see Fig 5.2). Given a particular state, a certain distribution of measurements will result. This can be thought of as a forward process, and the likelihood distribution $P(Y|X)$ defines it, where X is the state to be estimated, and Y is received or measured data. The inverse problem,

therefore, involves taking measured data and estimating the distribution of the state. The posterior distribution $P(X|Y)$ defines it, and it is found by applying Bayes' theorem

$$P(X|Y) = \frac{P(Y|X)P(X)}{P(Y)}. \quad (5.1)$$

In our case, the state-space X is the coordinates of device-free entities within a wireless network, and the measurements Y are RSS values of each link in the network. We take the RSS measurements and infer the position of the targets by inverting the statistical model through the posterior distribution.

The likelihood function $P(Y|X)$, and the *a priori* knowledge of the state described in $P(X)$, describes the statistical model that can be used to invert the problem. We are therefore interested in knowing how the position of targets affects the resulting RSS measurements, and how those statistics change for different positions of the target. We expect a target standing on the line-of-sight (LOS) of a link to cause significant changes to the RSS measurements, while a target at a distant position away from the LOS will not. The statistics for each "link-target geometry" are modeled in the likelihood functions.

The *a priori* information $P(X)$ can be used to incorporate known information about the targets. Since targets must move with finite velocity, this information allows an inversion algorithm to more accurately estimate positions over time. If the location of the targets movement is constrained by walls or other obstacles, the probability that the target will occupy those areas can be set to zero.

5.3.2 Measurement Collection

To form a likelihood model, an experimental RF sensor network was deployed to capture measurements. The network nodes consisted of 34 TelosB nodes from Crossbow, each utilizing the IEEE 802.15.4 protocol in the 2.4GHz frequency band. The same token passing protocol as described in [15] was used to prevent wireless packet collisions while maintaining low data collection latency.

The experimental network was deployed in two areas, one throughout the aisles of a bookstore, and one around the outer perimeter of a home. Both cases were rich in multipath, and no furniture or obstructions were removed from the areas in which the networks were deployed. In the bookstore deployment, nodes were placed on

shelves and stands at approximately human waist level. Some links crossed through multiple aisles, and some were in direct LOS.

In the outer home deployment, the network was deployed in an area around a four-wall portion of a typical home. Three of the walls are external, and one is located on the interior of the home. The interior wall is made of brick and was an external wall prior to remodeling of the home. Objects like furniture, appliances, and window screens were not removed from the home to ensure that the tracking was functional in a natural environment.

The nodes were placed in a rectangular perimeter, as depicted in Fig. 5.3. It was neither possible, nor necessary, to place the nodes in a uniform spacing due to building and property obstacles. Eight of the nodes were placed on the inside of the building, but on the other side of the brick interior wall.

To avoid network transmission collisions, a simple token passing protocol is used. Each node is assigned an ID number and programmed with a known order of transmission. When a node transmits, each node that receives the transmission examines the sender identification number. The receiving nodes check to see if it is their turn to transmit, and if not, they wait for the next node to transmit. If the next node does not transmit, or the packet is corrupted, a timeout causes each receiver to move to the next node in the schedule so that the cycle is not halted. A base-station node that receives all broadcasts is used to gather signal strength information and pass it to a laptop computer for processing.

RSS data were gathered as humans walked near and through the networks. The location of each person was carefully tracked by placing markers on the ground. To keep each target moving at a constant velocity, an audible metronome was played over a speaker, allowing each person to step to the next marking at the correct time. Using this technique, millions of RSS measurements were gathered, along with their corresponding target positions.

Since our likelihood models are based on changes in signal strength, a calibration process was used for each deployment. During calibration, RSS measurements for each link were taken while the network area was vacant of people. Each link's RSS measurements were averaged and used to determine the change in RSS for modeling.

5.3.3 Fading Information

People moving near a wireless link will cause changes in RSS due to diffraction, shadowing, and fading. This temporal variation is different from small-scale or frequency selective fading that occurs due to relative motion between the transmitter and receiver in multipath environments. Instead, a subset of multipath components are affected by the presence of the person near the wireless link [17, 31].

When the channel is predominantly LOS, such as in an open outdoor area, then a human crossing the LOS will generally cause a drop in signal strength due to signal shadowing. This phenomenon has been applied to image the attenuation of humans within a wireless network [15].

When an environment is rich in multipath and heavily obstructed, the presence of a human on the LOS of a link causes unpredictable changes in RSS. Sometimes the power may drop, sometimes it may not change at all, and sometimes it will rise. To take advantage of these fluctuations, variance-based radio tomographic imaging (VRTI) was introduced [17], which enabled tracking of movement behind walls. The key weakness of VRTI, however, is that targets must remain moving in order to be tracked. Stationary targets or those that move very slowly will not be imaged.

We point out here that the amount of fading on a link plays an important role in the resulting temporal variation statistics. Links that experience deep fades due to the natural multipath environment are more likely to experience a high variance of RSS when a person enters the vicinity, and will usually increase in power. On the other hand, links that constructively interfere vary much less, and usually decrease in power when disrupted. This phenomenon was simulated in [72], and is further confirmed by our measurements. We call these constructively interfering situations “antifades” and quantify them in Section 5.3.4.

To further illustrate this phenomenon, an example of how RSS varies over time for two links of equivalent distance is shown in Fig. 5.4. Since the path length and environment are the same, one can observe that in relative terms, the fading level is 20 dB different. We can consider link 1 to be in an antifade and link 2 to be in a deep fade. As a human walks through the LOS path of the two links, the RSS changes. In the case where the link is in an antifade, very little variance is experienced when the person is not directly between the nodes. When the person crosses, the RSS

drops significantly since the link was already experiencing constructive multipath interference. Any disruption to the phases or amplitudes of the multipath would therefore bring the power down. In the deeply-faded link, the opposite is true; any disruption to the link tends to bring the power up. In this example the RSS generally increases while the human walks through the LOS, as seen in the figure.

5.3.4 Quantification of Fade Level

We now quantify the amount of fading occurring on a static link by defining a "fade level." In a wireless channel, the ensemble mean $P(d)$ (dBm) measured by the receiver is dependent on the distance d from the transmitter [73].

$$P(d) = P_T - \Pi_0 - 10 n_p \log_{10} \frac{d}{\Delta_0} \quad (5.2)$$

where P_T is the transmitted power in dBm, n_p is the path loss parameter, and Π_0 is the loss measured at a short reference distance Δ_0 from the transmitter.

In multipath environments, fading will cause a significant deviation from the prediction in the path loss equation. We quantify the fade level F (dBm) as the difference between the path loss prediction and the actual measured received power P_m in dBm.

$$F = P_m - P(d) \quad (5.3)$$

Assuming the locations of each node are known or estimated in a wireless network, it is simple to calculate the fade level for each link. First, the power for each link is measured and averaged over an arbitrary time period to obtain P_m . Next, the path loss model is given the known distance of the link to determine $P(d)$, based on a known path loss parameter and reference powers. The path loss parameter can also be estimated without prior knowledge by performing a fit using all measurements from the network.

5.3.5 Measurement and Modeling Results

No current model exists for the statistics of temporal variation on a wireless link as a function of the static fade level. To obtain such a model, we bin each RSS measurement according to its known fade level found during calibration. We then examine histograms for each bin of fade level. Additionally, we separate RSS measurements for when a person is located on the direct LOS path.

The distribution of RSS measurements when a person is on the LOS for low fade levels is found to have a heavier tail in the positive direction, while the distribution for high fade levels has a negative skew. Histograms of the data are shown in Fig. 5.7 and Fig. 5.7. For fading levels of -15dBm and less, the decay on the positive side of the skew-Laplace is much slower when a person is standing on the LOS path. On the other hand, when the fade level is greater than 10dBm, we see that tail on the negative side of the distribution is longer. When the target is not on the LOS path of the link, the variance of the distribution is significantly less. The data visualized by these histograms are in accordance with our heuristic argument that links already in a deep fade should rise in power when disturbed, and vice versa.

With the understanding that the skew of the RSS distribution is dependent on the static fade level, a nonsymmetric probability density function with both positive and negative support is desired. The skew-Laplace distribution fits our measurements surprisingly well, as seen in the quantile-quantile plots of Fig. 5.7 and Fig. 5.7. It is controlled by three parameters, and is defined as

$$f(x; a, b, \psi) = \frac{ab}{a+b} \begin{cases} e^{-a(\psi-x)} & \text{if } x \leq \psi \\ e^{-b(x-\psi)} & \text{if } x > \psi \end{cases} \quad (5.4)$$

where a and b represent one-sided decays of the distribution for values less than or greater to the mode ψ . For the purposes of DFL, the values for each parameter of the skew-Laplace distribution is dependent on the fading level of the static link and the link-target geometry.

The RSS distributions shown in Fig. 5.7 and Fig. 5.7 represent the two extreme fading cases. When a link is neither in a deep fade nor an antifade, the parameters of the distribution will fall between those of the extremes. In other words, the parameters of the likelihood model are dependent on the value of fade level. These parameters are approximately linear with the fade level, and we use the least-squares criteria to determine the line of best fit. The linear fit equations are presented in Table 5.1.

The mode parameter ψ for varying fade levels is shown in Fig. 5.7. We see that when the target is off the LOS path, the peak parameter is near zero for all values

of the fade level. When the target is located on the LOS path, a piecewise-linear function can be used to approximate the parameter for a given fade level.

The decay parameters for varying fade levels are shown in Fig. 5.7 and Fig. 5.7. All parameters can be approximated with a piecewise-linear function of the fade level. We see that as the fade level increases, the decay parameters increase as well for both the on and off LOS cases. In other words, links that experience a deep fade have higher variance than those that experience an antifade.

To summarize the model, the distribution of RSS measurements is dependent on the existence of the target on the LOS path, and on the static fade level of the link. The values for each of the different cases are presented in Table 5.1. The fade level, as discussed previously, can be computed by deploying a network before any targets have entered an area, or by processing measurements over time.

5.4 Particle Filtering

5.4.1 Overview

There are many frameworks for estimating a posterior distribution using likelihood models. Kalman filtering, in its multiple forms, is by far the most common of these algorithms. For our application, the *particle filter* is an attractive form of posterior estimation, and a simple and brief outline of particle filtering is provided here. The derivation, theory, and variants of the particle filter will not be covered, as this information is widely available in the literature [74–77].

There are a number of reasons why particle filtering is attractive for DFL in RF sensor networks. First, particle filters do not make any assumptions on linearity of the measurement process or the dynamics of the state being estimated. Since our likelihood models are dependent on the existence of a target on the LOS path of each link, this is an important flexibility. Furthermore, nonlinear models for target movement can be incorporated directly into the particle framework.

Secondly, unlike the Kalman filter, the particle filter does not require the likelihood distributions to be Gaussian. This is extremely important for applying our likelihood functions, as they are well-modeled as skew-Laplace. Assuming Gaussian distributions would be suboptimal, and may introduce significant tracking error.

Finally, the particle filter is attractive for real-time processing since incoming

measurements can be used to update the posterior estimation without storing a history of previous measurements. As new measurements arrive, the algorithm recursively predicts and updates its estimation in a manner similar to that of the Kalman filter.

The use of a particle filter for DFL is not without disadvantages. The primary weakness of particle filters is the computational complexity required to run the algorithm. The particle filter naturally relies on a high number of particles to achieve good accuracy, which comes at the expense of computational resources. There are many forms of the particle filter, including the auxiliary particle filter [75] and the unscented particle filter [76], which aim to increase efficiency.

5.4.2 Particle Filter Algorithm

In this work, each particle represents a particular hypothesized location coordinate of a target. Let \mathbf{x}_k be the true location of the target at time k , and let the set $\{\tilde{\mathbf{x}}_k^i\}$ be the set of particles that represent hypotheses of target position. Let $\{w_k^i\}$ be the weights of each particle at time k , let \mathbf{y}_k be the current difference in RSS measurements for each link from the calibration data, and let $\hat{\mathbf{x}}$ be the target location estimate. We use the following simple sampling-importance-resampling (SIR) [74] particle filter to perform our experiments.

1. **Measure:** Receive new measurement vector \mathbf{y}_k from the network. Each element of the measurement vector represents an RSS measurement from each link in the network. This measured value is differenced with calibration data to determine the change in RSS.
2. **Weight update:** For each particle $i = 1, \dots, N_p$, use the measurement vector \mathbf{y}_k to determine the updated weights.
 - Determine $p(\mathbf{y}_k | \tilde{\mathbf{x}}_k^i)$ using the skew-Laplace likelihood model with parameters found in Table 5.1. Fade levels are determined during calibration, as described previously.
 - Update weights with $w_k^i = w_{k-1}^i p(\mathbf{y}_k | \tilde{\mathbf{x}}_k^i)$.
3. **Normalize the weights:** $w_k^i = w_k^i / \sum_j w_k^j$.

4. **Resample:** Particles with heavy weights are reproduced, particles with very low weights are eliminated. A simple algorithm for performing this task is found in [74].
5. **Move the particles:** Apply a Markov transition kernel to each particle. In our experiments we use the Metropolis-Hastings algorithm with a standard normal randomization [78].
6. **Estimate:** Average the particles to obtain the mean of the posterior distribution as the current state estimate.

In this algorithm, we assume that the particle filter proposal distribution $q(\mathbf{x}_k|\mathbf{x}_{k-1}, \mathbf{y}_k)$ is equal to the Markov transition $p(\tilde{\mathbf{x}}_k|\mathbf{x}_{k-1})$, which leads to the very simple weight update step. While this assumption makes for easy implementation, the efficiency of the particle filter is drastically reduced, since the current measurement is not used to propose new particle positions. The development and application of more efficient DFL particle filter designs is a topic for future research.

5.5 Experimental Results

5.5.1 Description and Layout

This section presents the results of a through-wall tracking experiment utilizing the skew-Laplace likelihood models and particle filter. We use the same experiment data as in [17], which is the same outer perimeter deployment discussed in Section 5.3.2.

In all experiments presented here, a calibration of RSS was taken while the surveillance area was vacant. The calibration stage lasted for approximately 30 seconds, and all RSS values were averaged for each link over this period. Each incoming measurement is then compared with the calibration data to determine the change in RSS, as discussed in the modeling. The calibration measurement is also used to determine the fade level of each link. A flowchart of the entire process is provided in Fig. 5.1.

5.5.2 Stationary Targets

A key benefit of the proposed models and algorithms is the ability to locate stationary objects behind walls. VRTI tracking systems [17] are unable to locate

stationary objects, since the algorithms rely on the variance caused by target motion. Here, the particle filter is able to locate stationary targets as long as calibration data is available.

The convergence of the particle filter around a target is illustrated in Fig. 5.7 and Fig. 5.7. After five iterations of the filter, particles along a particular narrow area survive, while other areas are eliminated. This is because a particular link is reporting a statistically significant change in RSS, and the particle filter narrows its search to areas near that particular LOS. In this case, after ten iterations, the particle filter has completely converged around the target's position.

To determine the accuracy of the statistical method for tracking stationary objects through-walls, 20 trials were performed. At each trial, a human target stood completely motionless at a different known location on the interior of the surveillance area. The known and estimated positions are shown in Fig. 5.14. The average error over the 20 trials was 0.83 meters.

5.5.3 Moving Targets

To test the accuracy of our model for tracking moving targets, a human target moves at a typical walking pace on a predefined path at a constant speed. A metronome and uniformly placed markings on the floor help the person to take constant-sized steps at a regular time interval. The target's actual location is interpolated using the start and stop time, and the known marker positions. The results of the tracking are presented in Fig. 5.15, and the average error for this test was 1.02 meters.

The particle filter is less effective for the moving targets than for the stationary targets in our experiments. This is because the particle filter has not been designed to take into account the true dynamics of a moving target. Since targets tend to move in spurts of constant velocity, for example, this information can be incorporated for more accurate tracking.

Another weakness of the particle filter for tracking moving targets is known as "particle impoverishment." Since the particles eventually converge around a small area, if the target "escapes" the cloud of current particles, it becomes very difficult for the filter to track. In other words, the target is located at a position where no

hypotheses are being made. Thus, developing a particle filter design that takes into account current RSS measurements to propose new particles is an important topic for future research.

5.6 Related Work

Various sensor technologies can be used for the purposes of DFL [8]. The most common form of a DFL sensor is the optical camera. Infrared and thermal cameras are also increasingly common in military and security applications. While these technologies are certainly valuable, visible light cameras depend on an external source of light. Furthermore, optical, thermal, and infrared sensors are hindered by opaque or insulating obstructions.

There is an advantage to using radio frequency sensors to infer people's locations instead of optical, thermal, and infrared sensors. RF waves have the ability to penetrate obstructions like walls, trees, and smoke. Thus, DFL systems that use RF sensors (RF-DFL) are capable of locating people through walls, in poor-sight outdoor environments, or in a smoke-filled buildings. These capabilities have obvious value for military organizations, police forces, and firefighter and rescue operations. Furthermore, RF-DFL systems often do not have the ability to identify or get detailed information about the people's actions. In some applications this may be a limitation, but in others the additional preservation of privacy compared to camera surveillance may be desirable.

The most common and widely used form of RF-DFL is ultra-wideband (UWB) radar [38, 39]. UWB systems work by producing a very fast pulse of RF energy and recording the amplitudes, time delays, and phases of the reflections caused by objects and people in the vicinity. Some UWB systems are monostatic, meaning the transmitter and receiver are incorporated into a single device. Others are multistatic, where a single pulse transmission may be received by multiple devices deployed throughout an area.

Recently, researchers have begun to study and develop DFL systems that use the received signal strength (RSS-DFL) of links in narrowband RF sensor networks. The advantage to this approach lies in the fact that RF sensors capable of measuring signal strengths are ubiquitous and inexpensive. The cost of each node is orders

of magnitude lower than a UWB device, so deploying a network with tens or hundreds of nodes is financially feasible in many applications. Furthermore, RSS measurements can be obtained from off-the-shelf devices like wireless networking routers, wireless sensor modules, and cell phones.

One approach to RSS-DFL in wireless networks is to use *RSS fingerprinting*, or *radio maps* [13]. In this approach, the system is trained by a person standing at many predefined positions, and RSS measurements are recorded while the person stands at each location. When the system is in use, RSS measurements are compared with the known training data, and the closest matching position is selected from a list. The accuracy can be further refined by combining multiple best-matching positions and using an appropriate interpolation [21].

The strength of the RSS fingerprinting approach is that the variations in RSS caused by the target in the multipath environment are an advantage. Each target position will lead to very different vector of RSS measurements, making it easier to detect the location. The weakness of such a system is the need for manual training and maintenance. Measurements must be taken offline, and changes to the environment such as doors opening or moved furniture will corrupt the training. Furthermore, the training becomes exponentially difficult for localization of multiple targets.

Zhang et. al. present an algorithm which directly estimates a human's position from RSS measurements [11]. In this work, when a link measures RSS variation above a threshold, it is assumed that the target is located within a rectangle centered at the midpoint of the line between the transmitter and receiver. A "best-cover algorithm" then estimates the person's position, which is input into a tracking filter. This work was extended in [18] to use a clustering algorithm for multiobject tracking.

One approach to DFL is to estimate an image of the change in environment. This image can then be used to infer the motion and activity within the environment, either by a human operator, or by an image processing algorithm. Image estimation from measurements along different spatial filters through a medium is generally referred to as tomographic image reconstruction. For RF sensors, this is termed radio tomographic imaging (RTI) [15, 17, 19, 45]. In [15], the attenuation in dB

caused by each voxel in the environment is imaged using measurements of RSS for each link in a dense wireless network. This technique can be referred to as shadowing-based RTI, since the measurements effectively measure shadowing loss, and the image estimates are shown to accurately display the location one or two people in the deployment area [15]. The linear model for shadowing loss is based on correlated shadowing models [45, 46].

Another modality of RTI is termed variance-based RTI, in which the windowed variance of RSS on each link is used as the measurement, and the estimated image represents a quantification of the motion within each voxel. Experimental tests reported in [17] show that variance-based RTI can image the motion going on inside a house, when sensors are placed only outside of its external walls. In the case of imaging motion through building walls, we can have the problem that the multipath which travel around the building can be stronger than the power in paths which traveled through the building. Analytical results in [17] suggest that the change in variance can be detected even when the power in the affected multipath is 10 dB less than the multipath which do not go through the building.

5.7 Conclusion

Previous work in the field of RSS based DFL has proven that it is possible to locate humans using only RSS measurements, even through walls. In particular, radio tomographic imaging provides a method for DFL that does not require exhaustive training information, but previous work in this area has been unable to locate stationary or slowly moving targets in highly obstructed areas. This paper provides a statistical model and inversion method that is capable of locating stationary as well as moving targets.

The amount of fading on a static link is an important factor in determining the signal strength distributions when a target enters an area. If the link is already in a deep fade, the disturbance a target causes to the multipath will tend to bring the signal strength up. Links in deep fades also exhibit more variance, since even slight changes to multipath components can bring the link out of the fade. Links that experience antifades, however, exhibit the opposite behavior. Changes to the environment due to target presence tend to bring signal power down, and variances

remain much lower.

The skew-Laplace distribution is a reasonable representation of how RSS measurements change when a target is present. The mode and decay parameters of the distribution are dependent on the fade level of the link, as well as the target's position. When a target is on the LOS path of the link, RSS fluctuations are significantly larger than when the target is off-LOS. Each parameter, for both the LOS and off-LOS cases, is linear with the fade level.

Since the likelihood models are non-Gaussian and nonlinear, the particle filter framework is an attractive way to estimate target positions using RSS measurements. Experiments using a particle filter and the skew-Laplace likelihood models demonstrate the method's effectiveness in locating stationary and moving targets behind walls. Previous work in through-wall DFL in wireless networks was unable to locate stationary objects at all.

There are many opportunities for future work on statistical models for DFL in wireless networks. First, the skew-Laplace and LOS models presented in this paper are only one way of approaching the problem. Other methods certainly exist, some of which may provide a better statistical divergence for varying target positions. A model that has higher contrast for the on-LOS distributions vs. the off-LOS distributions will lead to more accurate DFL tracking.

Next, the basic particle filter needs to be further refined for more efficient and accurate tracking. A mechanism for proposing new particles based on current measurements will allow the filter to track with much fewer particles, thus saving computational resources. Furthermore, improvements to the particle filter's motion modeling will result in more accurate tracking.

Finally, a model that explicitly accounts for multiple targets needs to be investigated. As many people enter the area near a wireless link, interactions of the multipath components become more complex. The RSS measurement statistics of such a scenario need to be modeled, quantified, and then applied in an estimation framework like the particle filter. Multiple target tracking is a necessity for many practical DFL applications.

Table 5.1. Linear parameter fitting for the skew-Laplace likelihood model

	ψ	a	b
LOS ($F \leq -6$)	$-3.85 - .631F$	$.350 + .004F$	$.607 + .028F$
LOS ($F > -6$)	0.0	$.350 + .004F$	$.607 + .028F$
Off LOS	0.0	$.726 + .019F$	$.902 + .040F$

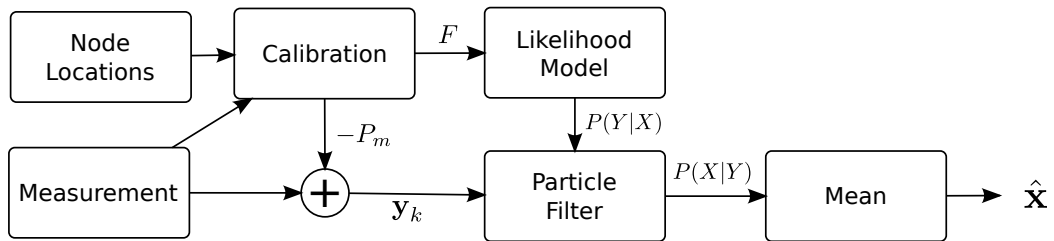


Figure 5.1. A flowchart describing the statistical inversion process for device-free localization in wireless networks.

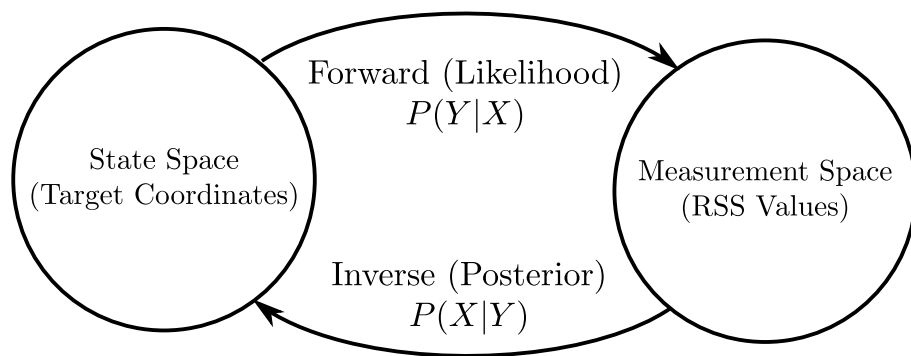


Figure 5.2. An illustration showing the role of likelihood and posterior distributions for statistical inversion.

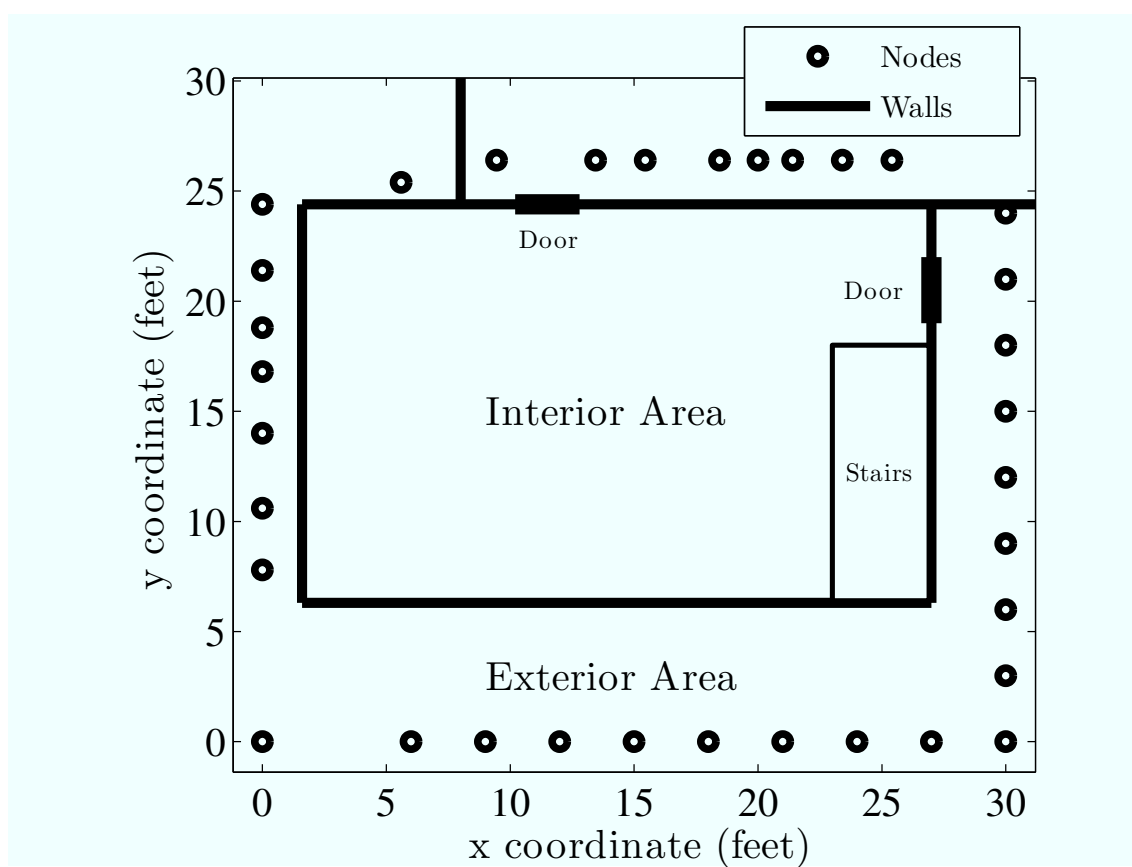


Figure 5.3. The layout of a 34-node through-wall wireless network deployment.

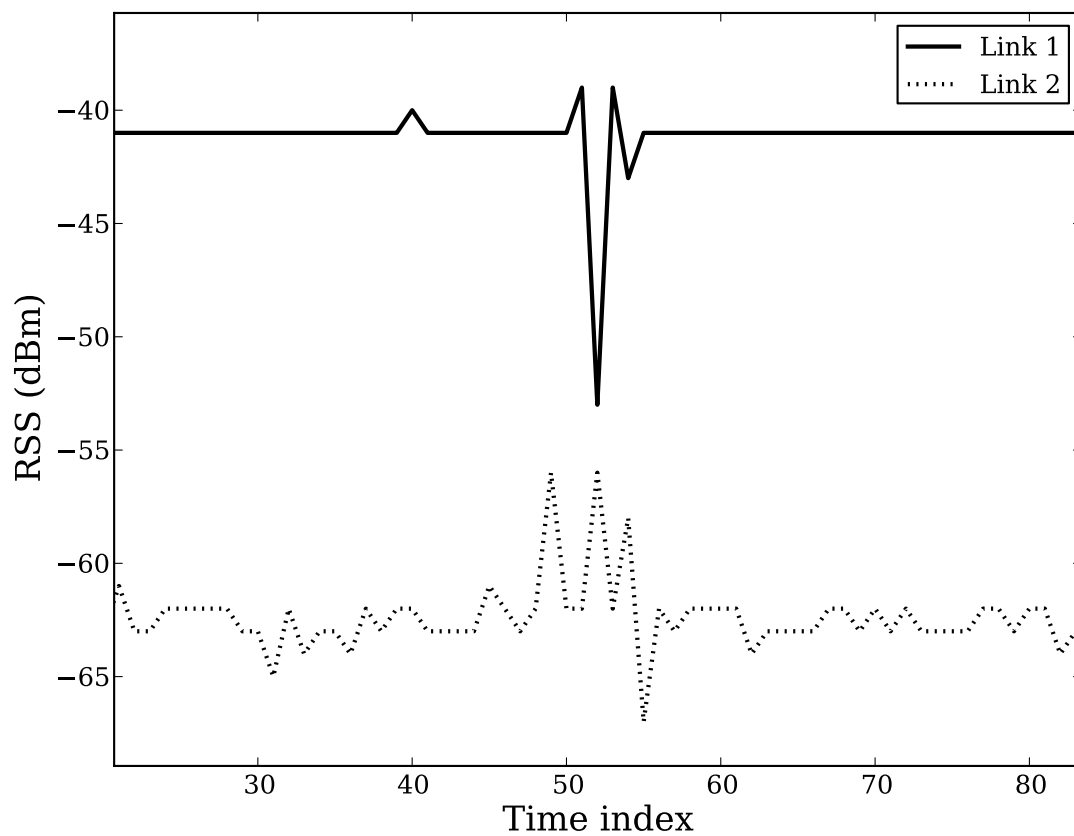


Figure 5.4. An example of how the RSS statistics for two links of equivalent distance and geometry are drastically affected by the fade level. Here, a human crosses through the LOS at $t = 52$. Link 1 is in an "antifade" while Link 2 is in a deep fade.

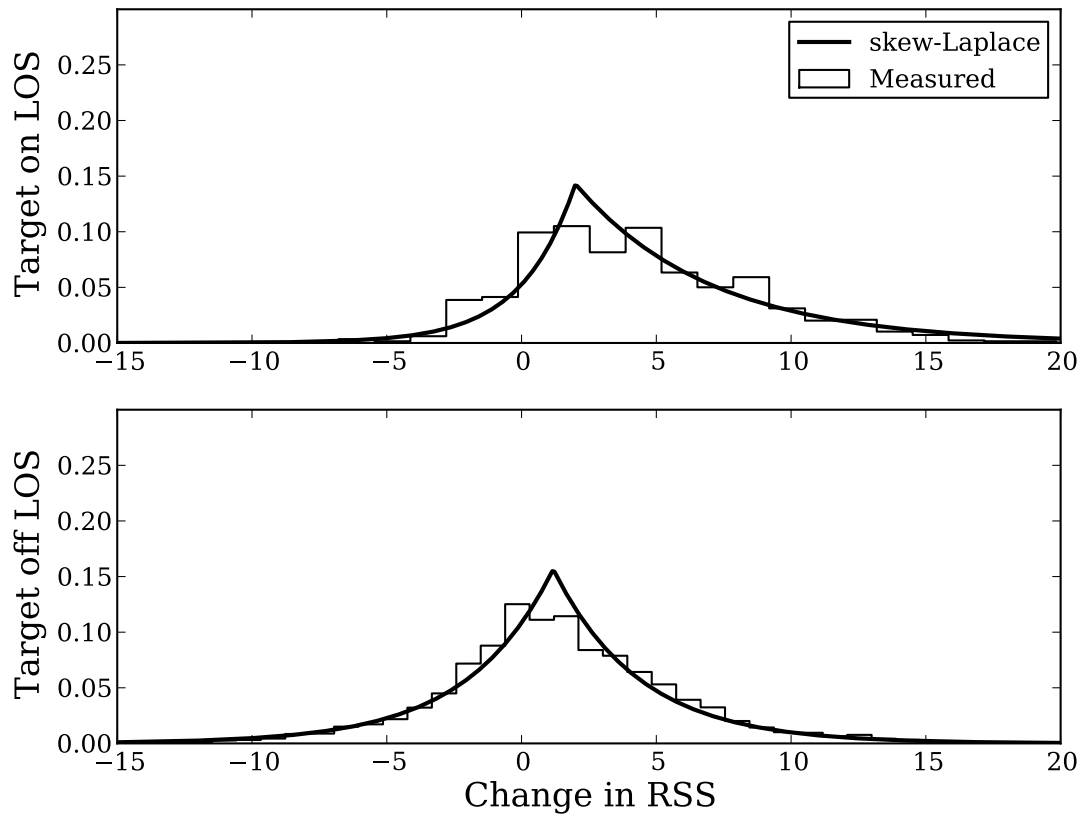


Figure 5.5. RSS measurement distributions for on/off LOS target positions. The histograms are for links experiencing deep fades less than -15dBm.

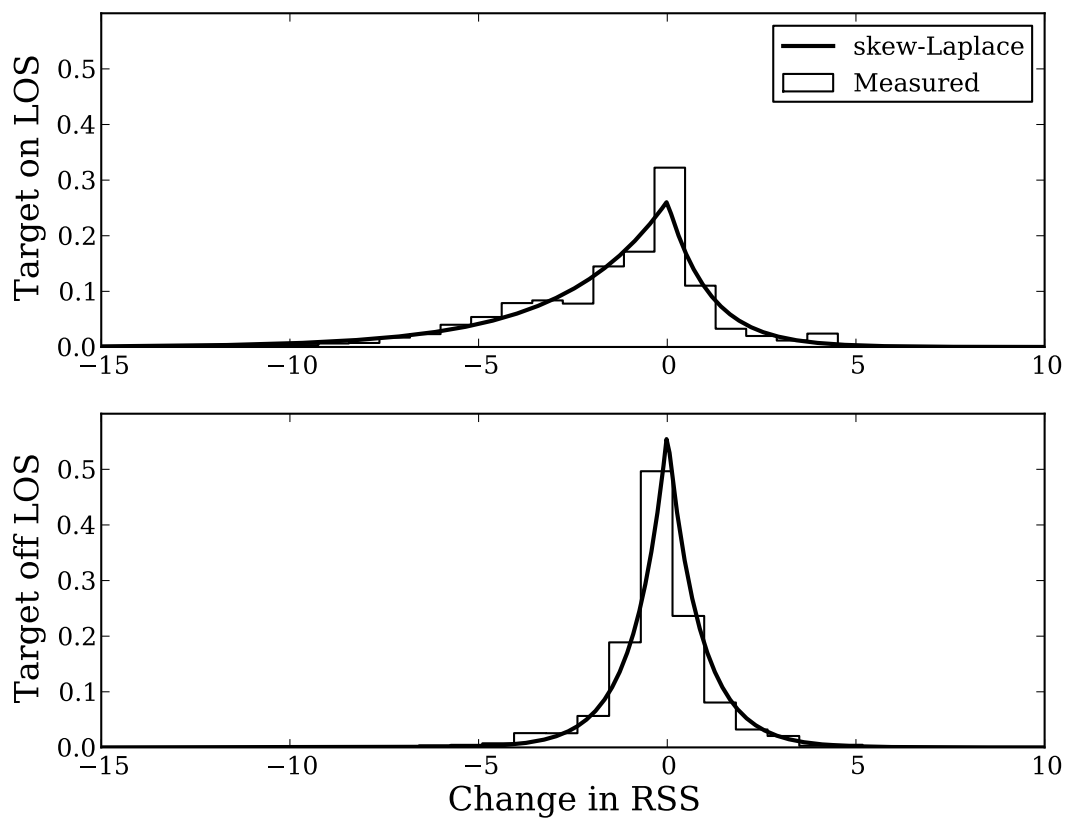


Figure 5.6. RSS measurement distributions for on/off LOS target positions. The histograms are for links experiencing antifades greater than 10dBm.

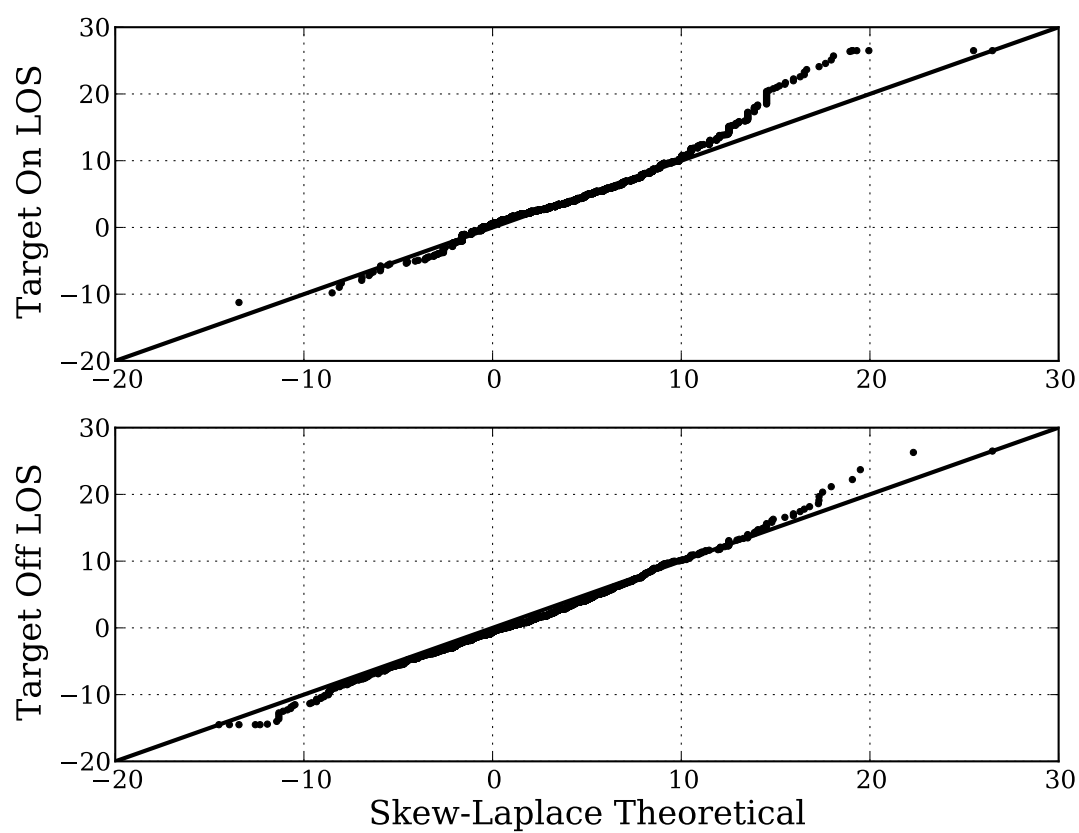


Figure 5.7. Quantile-Quantile plots for deep fades.

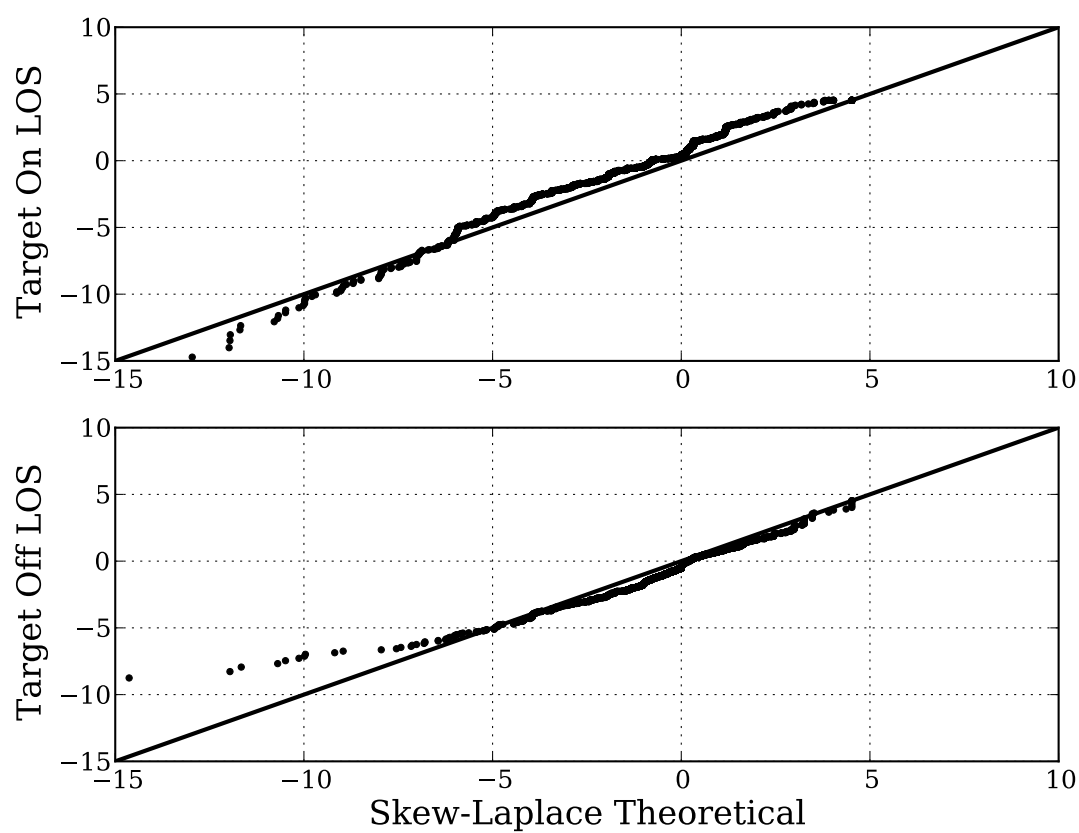


Figure 5.8. Quantile-Quantile plots for antifades.

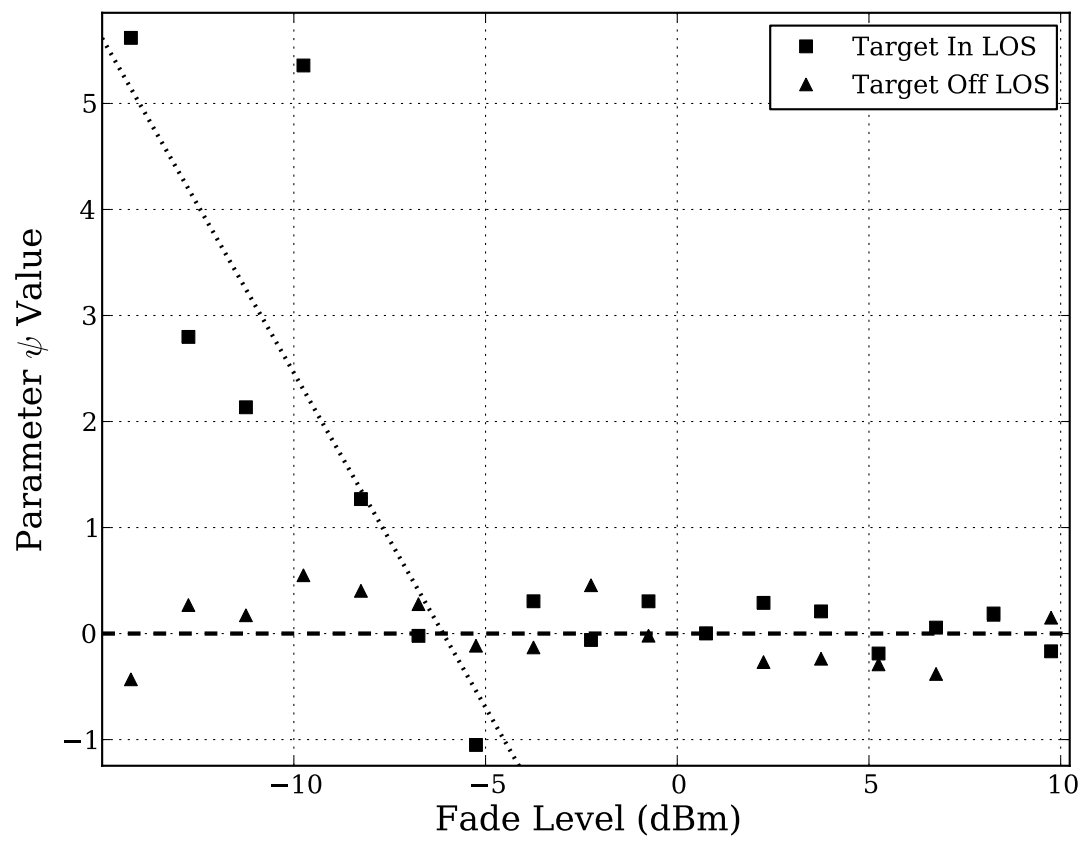


Figure 5.9. Mode parameter fitting over a range of fade levels in dBm.

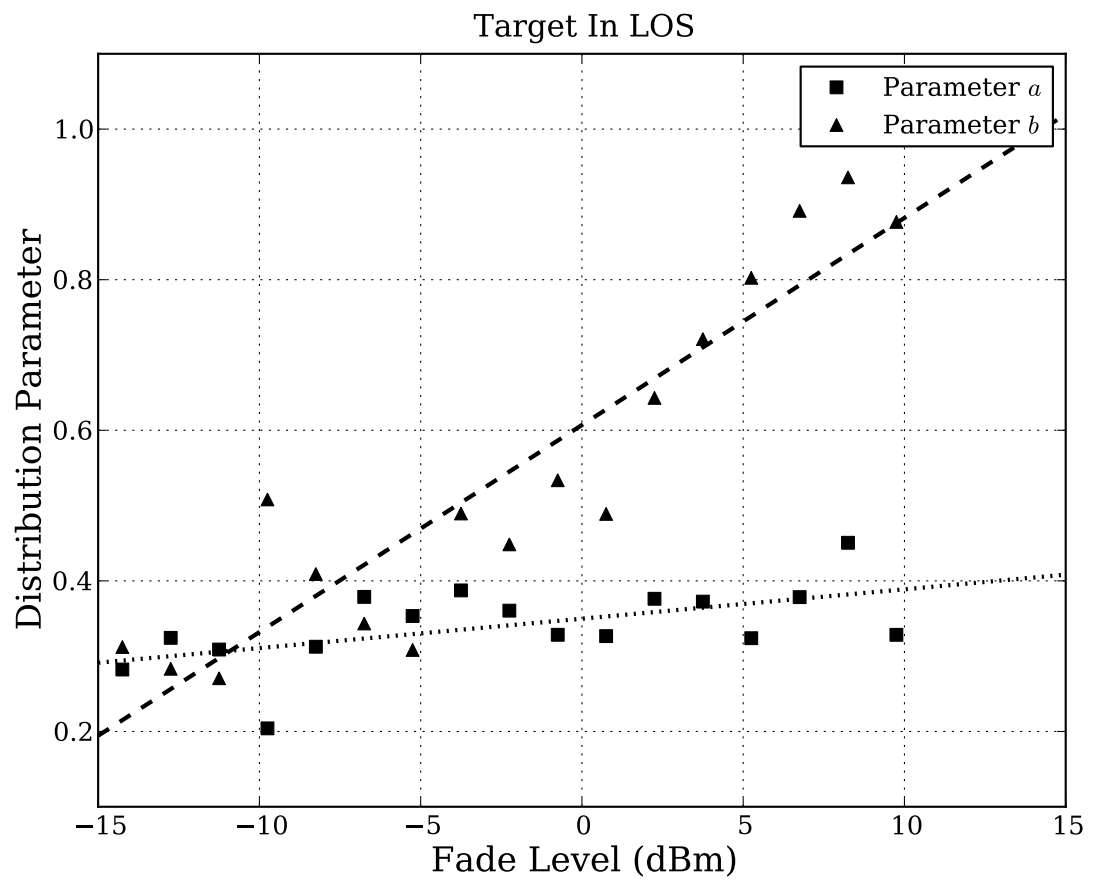


Figure 5.10. Decay parameters when the target is located on the LOS path.

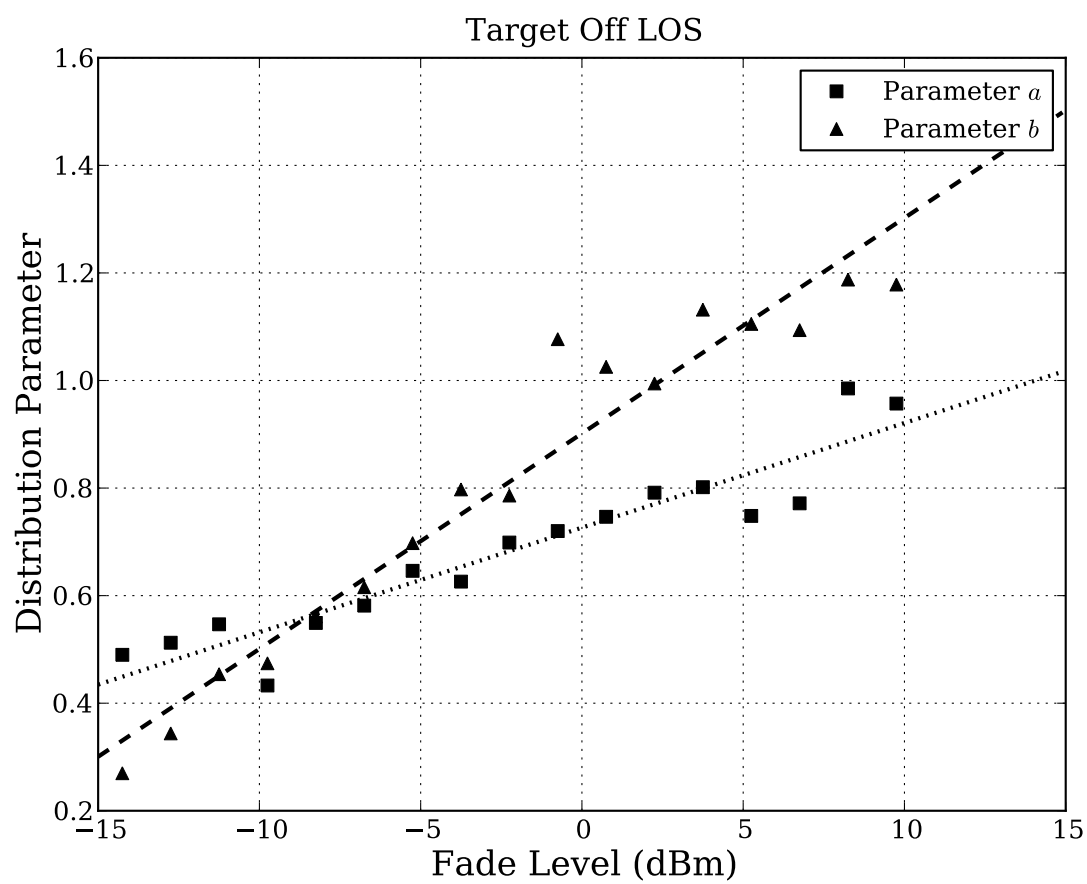


Figure 5.11. Decay parameters when the target is off the LOS path.

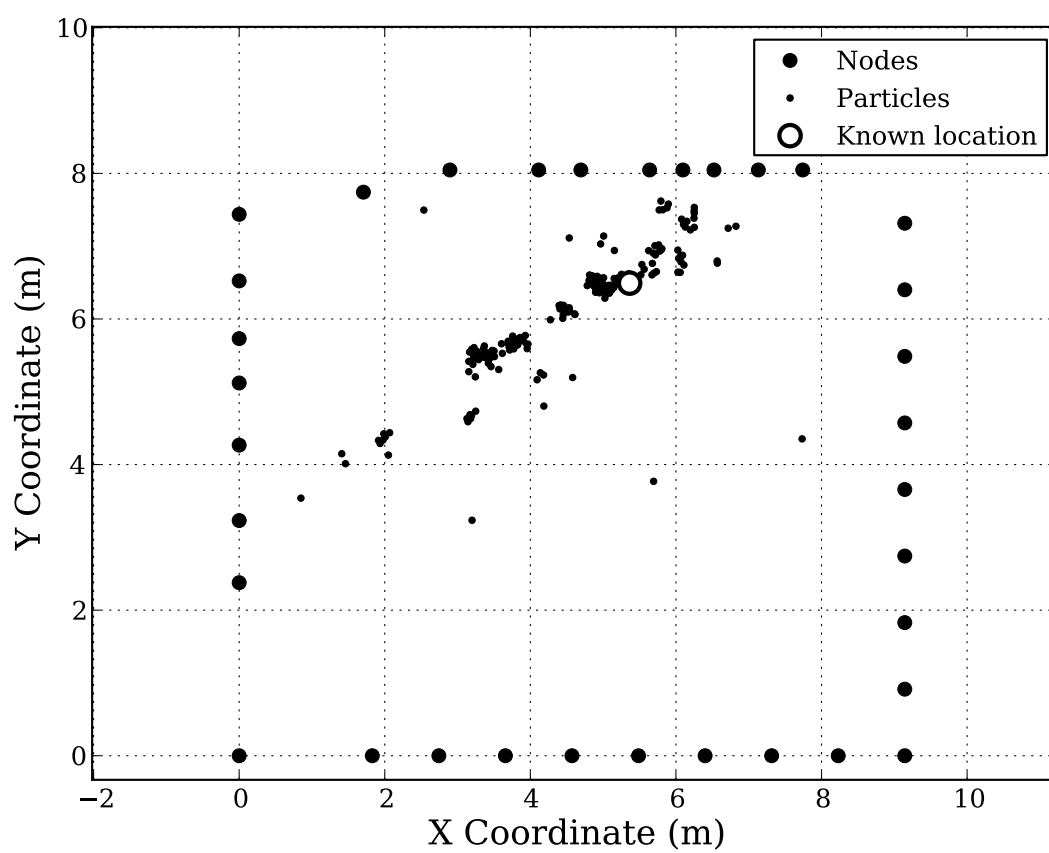


Figure 5.12. The convergence of the particle filter after 5 iterations. The filter has determined that the target is located along a particular LOS path.

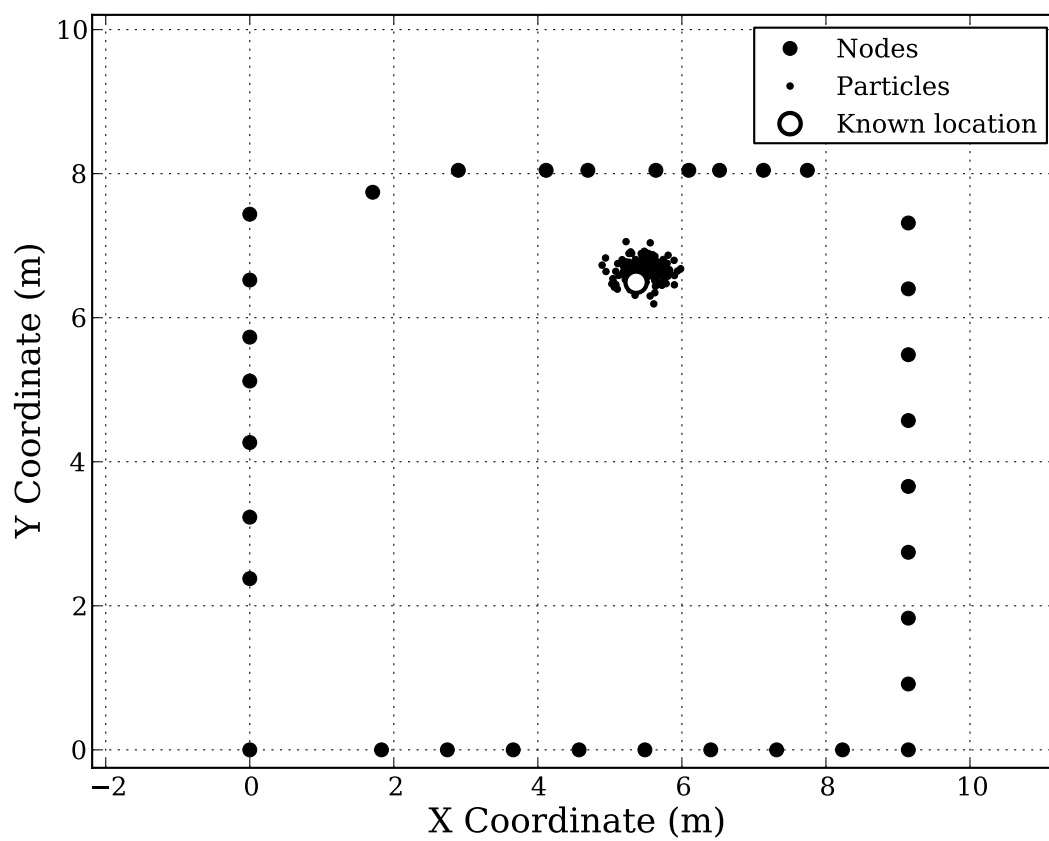


Figure 5.13. The convergence of the particle filter after 10 iterations. The filter has completely converged around the location of the target.

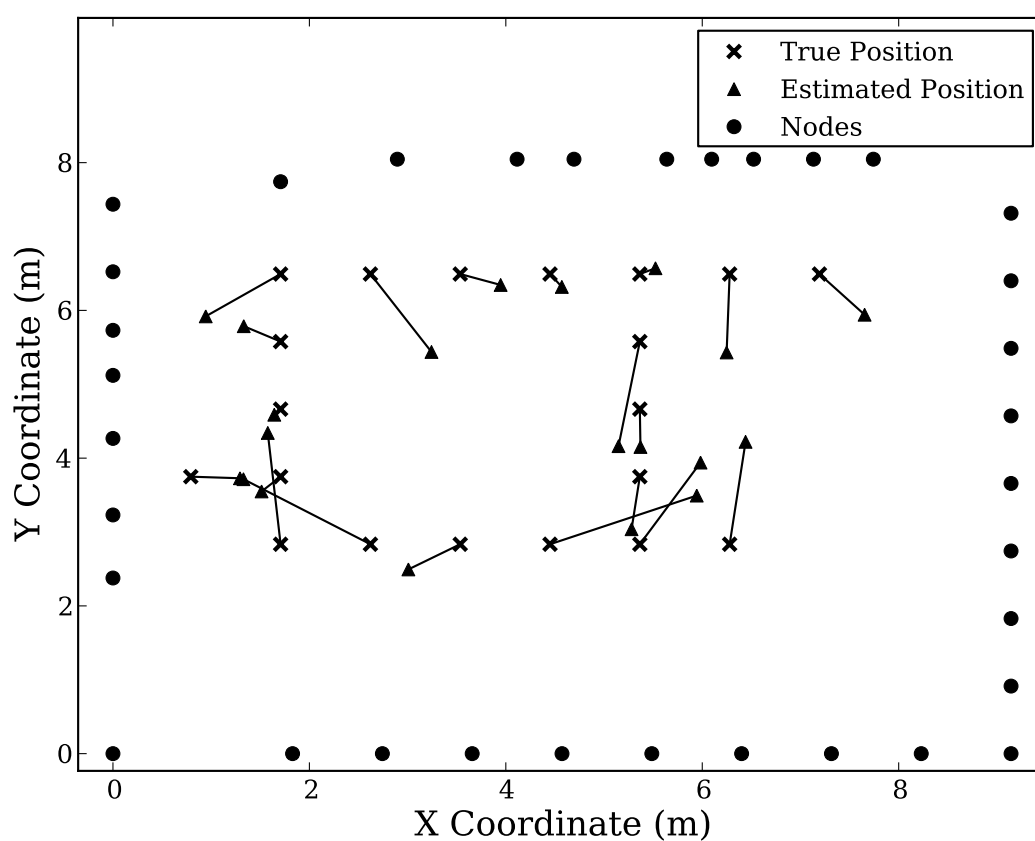


Figure 5.14. Estimated positions of a stationary target at different positions. The estimated position was taken after 50 iterations of a particle filter with 200 particles. The average error for this experiment was .83 meters.

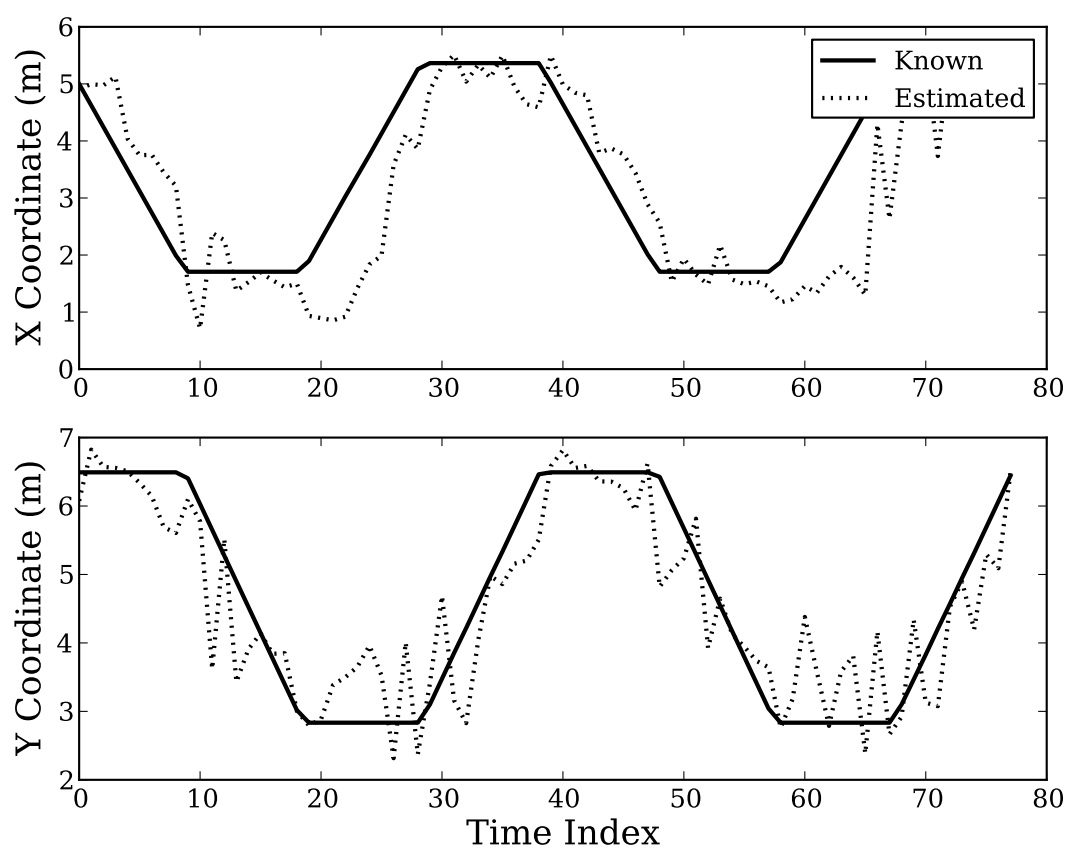


Figure 5.15. Estimated positions of a human walking along a known path. Here, the particle filter uses 200 particles and tracks with an average error of 1.02 meters.

CHAPTER 6

CONCLUSION

This dissertation is concluded with a summary of key research findings. Opportunities for future work are also discussed.

6.1 Key Findings

When humans and other moving objects enter the vicinity of a wireless link, the signals are reflected, absorbed, diffracted, and scattered by the mass of the body. This leads to changes in measured signal strength at the receiver. In outdoor areas, or in other predominantly LOS environments, a human standing along the LOS of a link usually shadows the signal.

Experiments in LOS environments show that the shadowing attenuation of a human body can be imaged using only signal strength measurements in a wireless network. The key assumption used in the imaging is that the signal travels in a direct line from transmitter to receiver, and the location of each node in the network is known. This technique, called radio tomographic imaging, can be used to locate humans or other changes to the attenuation of the environment. Noise in such a system can be modeled accurately using a mixture Gaussian distribution, and lower bounds on the error of the tomographic image can provide an idea of image accuracy for different network geometries.

In rich multipath and heavily obstructed areas, the shadowing model of RTI begins to break down. Humans moving near the wireless links still affect the measured RSS at the receivers, but in a much less predictable manner. A human standing directly on the LOS path of a link may cause the RSS to lower, to not change significantly, or to rise. The attempt to image based on shadowing effects of the signals fails in these cases.

Even if a mapping of how a signal propagates through a multipath environment were available, estimating the attenuation using only signal strength is not possible.

If a person only affects a subset of the total multipath, and no phase information is available at the receiver, there is no way to predict whether the change in multipath will cause constructive or destructive interference. Therefore, the RTI model which proposes the estimation of attenuation due to shadowing only, is not viable. The model must be changed to estimate more abstract values, such as presence and motion.

Variance-based radio tomographic imaging is a method that can compensate for the unpredictable changes in RSS in a heavy multipath environment. In this technique, it is not assumed that the signal will be shadowed by the presence of a human on the LOS path. Instead, we assume that when a human moves near the LOS of a link, the RSS will experience more variance than if the human moves at a far distance from the LOS path. By examining the variances of each link in the network, an image of where motion is occurring can be estimated.

Variance-based radio tomographic imaging is capable of imaging movement in rich multipath environments, even through walls. An experiment of 34 nodes deployed around the exterior walls of a home showed the VRTI system was capable of locating a moving human with an average error of less than one meter. This could provide a powerful method for locating people through walls in rescue, military, and other emergencies, where entry to a building is not possible. The key limitation of variance-based methods is that the people being tracked must be in motion. If someone moves very slowly, or remains motionless, their location is not revealed in the image.

To further understand the statistics of RSS in DFL networks, a detailed model was developed based on extensive measurements in networks deployed in real-world environments. A key finding during this study was that the static fade level of a link plays a significant role in determining the statistics of temporal variation. When a link experiences a deep fade, people entering the area will usually increase the signal strength measured at the receiver. On the other hand, when a link is constructively interfering, humans interfering with the signals will usually bring the RSS down in power. Additionally, RSS variance of a link is higher when it experiences a deep fade. The statistical distributions of temporal variations therefore have long and asymmetric tails, depending on the fade level of the static link. Links in deep fades

have distributions with longer positive tails, while links in anti-fades have longer negative tails.

It's important to note that links in deep fades are not necessarily of less value than those in antifades. Links in deep fades are more sensitive to small changes in the environment, which is why more variance is experienced. The important metric in evaluating the ability of a link to localize a target is the divergence of the LOS vs non-LOS distributions. When the divergence of these two distributions is high, the ability to distinguish the location of a target is enhanced. Divergence may provide an important metric for comparing the performance of the skew-Laplace LOS model with other possibilities that will arise in future work.

To fit these shapes, the skew-Laplace distribution is useful for two reasons. First, it can be skewed in either the positive or negative direction, depending on the parameters. This allows for fitting the RSS measurements in deep fades and in anti-fades. Quantile-quantile plots show that the fit is very accurate. Secondly, the parameters of the skew-Laplace distribution fit RSS measurements in real-environments with a piecewise linear function of the fade level. If the fade level of a link is known, then the parameters of the distribution can be determined easily, providing an accurate accurate statistical model of how signal strength should change when a person stands on the LOS of a link.

The skew-Laplace likelihood model can be applied in statistical inversion algorithms to locate people with RSS measurements. Particle filters are attractive for this purpose for a few reasons. First, particle filtering does not require that the likelihood functions are Gaussian. Assuming Gaussian distribution in this case is erroneous, and would introduce significant modeling error. Second, particle filters can easily handle nonlinear measurement processes and state-transition processes. In this case, measurement statistics are non-linear since they change depending on if a person is located on the LOS of the link or not.

An experiment using the skew-Laplace model and a basic particle filter algorithm shows that a person can be located and tracked behind walls with an average error of approximately one meter. The advantage here is that stationary or slowly-moving people can be located, thus addressing the key limitation of variance-based tomography. The key cost of using particle filters is computational, and future work will

require the development of more efficient particle filters for RSS-DFL.

6.2 Comparison of Tracking Methods

Each tracking method presented in this dissertation holds some key advantages and disadvantages. The shadowing-based RTI model is appealing in predominantly LOS environments where multipath is low. This may be the case for outdoor areas, or indoor areas with large and obstruction-free zones. The model is easy to implement, can be run on modest computing hardware, and can accurately locate both stationary and moving objects. Furthermore, multiple objects can be imaged easily, since the non-linearities of introducing multiple people in an area does not overwhelm the LOS shadowing models.

VRTI tracking is very simple to implement and can be run in real-time on modest computer hardware. All models are linear, and estimation of the VRTI results are calculated in closed form via Tikhonov regularization. The Kalman filter is also extremely efficient at tracking the peak of the image stream, and since variance can be calculated on the fly, no calibration is needed. The no-calibration feature is a key feature of VRTI systems, as they can be deployed quickly in emergency situations with no baseline measurements.

The skew-Laplace particle filter tracking claims the key advantage of being able to locate people in heavily obstructed areas when they are not moving. However, this is done at the expense of requiring calibration data. This calibration data could possibly be automatically determined for emergency deployments, but there will always be the penalty of a more complicated algorithm when compared to purely variance-based methods for the purposes of calibration.

Our experiments show an average error for locating a person walking within walls of 2.07 feet using VRTI with Kalman filter tracking, and an average error of 3.3 feet for the skew-Laplace particle filter. The comparison, however, is not particularly meaningful since the parameters of VRTI and the Kalman filter are not directly comparable with those of the particle filter. It's sufficient to say that tracking performance of both the VRTI and statistical methods are on the same order, with one being preferable to another depending on the computational resources available, and the circumstances of deployment.

6.3 Future Work

The field of RSS-based device-free localization is very ripe for future research. Opportunities to improve this technology exist in hardware, protocol design, physical layer signaling, applied mathematics, and statistical inversion. This section will describe some ideas that are currently ready for investigation.

Hardware design will play a key role in the improvement of RSS-DFL networks. The effect of directional and polarized antennas needs to be investigated, especially in through-wall deployments where it is critical to radiate as much energy into the surveillance area as possible. Radios with higher resolution RSS indicators may also lead to significant improvements in tracking, as current studies typically use hardware with approximate quantizations of one dBm.

Future hardware may be able to incorporate phase information into DFL algorithms without a drastic increase in node cost. It is important to note that radio tomography is by nature a non-linear problem; the propagation of the waves, and thus the measurement process, is dependent on the values being estimated. Having phase information available may allow future models and algorithms to estimate the scattering caused by the device-free objects themselves, and thus lead to more accurate tracking. This will be especially important for tracking a higher number of people, since the measurements become highly coupled in these cases.

Physical layer studies need to be performed to determine the effect of frequency, bandwidth, and spectral shape in RSS-DFL systems. Lower frequencies are known to penetrate obstructions easier, but RSS measurements at longer wavelengths may be less affected by human movement. What frequencies are best for locating people in the various DFL applications? Can the use of multiple frequencies improve performance? How does modulation and spectral shape improve or degrade performance? These are all questions that need to be further investigated in future research.

Along with future investigation of physical layer signals for DFL, incorporation of environmental aspects of a region may provide a significant improvement to the technology. If the electromagnetic properties of walls is known beforehand, for example, this information could be used to refine the models and improve localization accuracy. One should take into account the fact that wood or drywall

materials may cause the system to behave completely differently than reinforced concrete or brick. Perhaps integrating the model with floor plans and materials could allow one to adapt the model without too much of a user burden. The more prior information that can be incorporated, the better DFL performance can be achieved.

Automatic localization during calibration is another important aspect in the design of rapidly deployable DFL networks. In emergency situations, responders will not have time to manually determine the location of each node of the tracking network. To address this limitation, the system would first need to undergo a localization phase during calibration. The responders would randomly deploy the nodes around the area of interest, and upon completion of node localization, they would begin estimating location of device-free entities. This could be accomplished with GPS in outdoor environments if the accuracy is high enough, or possibly by various sensor localization methods, including RSS-based techniques.

As DFL networks are deployed over large areas, the technology will require new methods for quickly measuring RSS and transferring them to a processing station. As more nodes are deployed over large distances, the latency of capturing data will become more of an issue. This problem creates a need for protocols that are capable of learning where packet collisions occur in the network, and scheduling each node transmission accordingly. The optimal scheduling will allow nodes that are out of range from each other to efficiently transmit without causing a collision at neighboring nodes.

In addition to spatial reuse protocols, frequency reuse is an important area for future research. How can frequency hopping allow for nodes to gather RSS measurements quickly without causing interference at neighboring cells? By using multiple frequencies, can more information be delivered to the base station for processing in the same amount of time? These and other questions need to be investigated in future research.

While some research on different regularization methods have been discussed in this dissertation, there are many more that need to be investigated. The images in RTI represent changed attenuation, and images in VRTI represent motion. Both are quantities that should be constrained by non-negativity in the mathematical regu-

larization models. Incorporating this information will very likely lead to improved image accuracy and tracking.

The work in this dissertation has shown that non-linear regularization methods like total variation are very appealing for RTI. The resultant images are high contrast, and have sharp edges at the boundaries of the object being imaged. The downside is that these non-linear methods require a numerical optimization routine, which increases the computational complexity of the estimation significantly. In RTI and DFL applications, however, the current solution is often very close to that of the previous solution. Incorporating this information into iterative image estimation and filtering methods may allow for high image quality when using otherwise computationally complex regularization techniques. Furthermore, past measurements can be used to more accurately estimate current images in a recursive fashion.

The RTI and DFL models presented in this paper generally assume that changes in signal strength happen most on the LOS of a wireless link. In real environments, this is not always true. Radio signals may diffract around metal objects or other dense obstructions, deviating the main path of propagation from a straight node-to-node line. One way to address this issue would be to incorporate known information about the environment into the model.

In many applications, however, incorporation of environment knowledge may not be efficient or possible. Instead, an adaptive transfer matrix model might increase performance. As measurements and estimations are made, the model could correct itself recursively by comparing current result characteristics with known desired characteristics. Many techniques found in the adaptive filter and blind equalization literature could be applied for the purposes of identifying the channel. With the estimated propagation information, the model can be updated for more accurate tracking and imaging.

Adjusting for changes to the propagation model might lead to more accurate results, and it also might lead to tracking objects in channels that are known to be changing. If one assumes that nodes are no longer statically deployed, but are attached to other humans throughout an area, then the channel will change significantly as the nodes move. An adaptive channel measurement system could

account for these changes and incorporate them into the estimation framework, thus allowing the device-free objects to be tracked by those carrying devices. This form of tracking would enable a number of compelling applications in security and rescue.

Particle filtering is an attractive form of estimation for RSS-DFL due to its nonlinear and non-Gaussian framework. However, the basic particle filter described in this dissertation is computationally expensive and inefficient. Particle filters that take into account current measurements to propose new particles is therefore an important aspect of advancing RSS-DFL technology. This will enable the tracking to be performed in real-time on small computers; a desirable characteristic in many applications.

Finally, for many applications, tracking multiple targets is essential. Future research must investigate statistical models for RSS measurements when multiple targets are present within the network surveillance area. How do the current skew-Laplace likelihood models change when multiple targets are standing on the same LOS path? How do the current models change when one person stands on the LOS path, and many others are off-LOS? Models that relate the coupled positions of multiple targets is a significant challenge, and yet they are extremely important in carrying the field of RSS-based device-free localization into the future.

The study of device-free localization using signal strength measurements in wireless networks is still in its infancy. For some applications, the technology is now ready for commercialization and delivery to real products and systems that will deliver valuable benefits to end users. Other applications will require further advancement before commercialization is possible.

As the simpler forms of RSS-DFL systems are successfully implemented in real-world systems, new needs and challenges will reveal themselves. These challenges will provide engineers with a stream of new research problems as the cycle of industry demands and research solutions continues. The field of RSS-DFL will, without a doubt, provide a basis for many innovative products and systems that will make our lives safer and richer.

REFERENCES

- [1] S. Oh, P. Chen, M. Manzo, and S. Sastry, "Instrumenting wireless sensor networks for real-time surveillance," in *Proc. of the International Conference on Robotics and Automation*, May 2006.
- [2] K. Nummiaro, E. Killer-Meier, and L. Van Gool, "Object tracking with an adaptive color-based particle filter," *Lecture Notes in Computer Science*, vol. 2449, pp. 353–360, 2002.
- [3] J. M. Lloyd, *Thermal Imaging Systems*. Plenum Press, 1975.
- [4] "Thermal matrix." <http://www.thermalmatrixusa.net>.
- [5] S. Young and M. Scanlon, "Detection and localization with an acoustic array on a small robotic platform in urban environments," tech. rep., Army Research Lab, 2003.
- [6] N. Priyantha, A. Chakraborty, and H. Balakrishnan, "The cricket location-support system," in *Proceedings of the 6th Annual Conference on Mobile Computing and Networking*, 2000.
- [7] M. Hazas and A. Ward, "A novel broadband ultrasonic location system," *Lecture Notes in Computer Science*, vol. 2498, pp. 264–280, 2002.
- [8] N. Patwari and J. Wilson, "Rf sensor networks for device-free localization and tracking," *Proceedings of the IEEE*, 2010.
- [9] R. R. Rogers and W. O. J. Brown, "Radar observations of a major industrial fire," *Bulletin of the Amer. Meteorological Soc.*, vol. 78, pp. 803–814, May 1997.
- [10] K. Woyach, D. Puccinelli, and M. Haenggi, "Sensorless sensing in wireless networks: Implementation and measurements," in *Second International Workshop on Wireless Network Measurement*, 2006.
- [11] D. Zhang, J. Ma, Q. Chen, and L. Ni, "An RF-based system for tracking transceiver-free objects," in *IEEE International Conference on Pervasive Computing and Communications*, 2007.
- [12] M. Nakatsuka, H. Iwatani, and J. Katto, "A study on passive crowd density estimation using wireless sensors," in *The 4th Intl. Conf. on Mobile Computing and Ubiquitous Networking (ICMU 2008)*, June 2008.
- [13] M. Youssef, M. Mah, and A. Agrawala, "Challenges: Device-free passive localization for wireless environments," in *MobiCom*, ACM, 2007.

- [14] M. Moussa and M. Youssef, "Smart services for smart environments: Device-free passive detection in real environments," in *IEEE PerCom-09*, pp. 1–6, 2009.
- [15] J. Wilson and N. Patwari, "Radio tomographic imaging with wireless networks," *IEEE Transactions on Mobile Computing*, vol. 9, pp. 621–632, January 2010.
- [16] J. Wilson and N. Patwari, "Regularization methods for radio tomographic imaging," in *2009 Virginia Tech Symposium on Wireless Personal Communications*, June 2009.
- [17] J. Wilson and N. Patwari, "See through walls: Motion tracking using variance-based radio tomography networks," *IEEE Journal on Selected Areas in Communications*, 2010. (Accepted for publication).
- [18] D. Zhang and L. Ni, "Dynamic clustering for tracking multiple transceiver-free objects," in *IEEE International Conference on Pervasive Computing and Communications*, pp. 1–8, 2009.
- [19] M. A. Kanso and M. G. Rabbat, "Compressed RF tomography for wireless sensor networks: Centralized and decentralized approaches," in *Distributed Computing in Sensor Systems (DCOSS)*, 2009.
- [20] P. W. Lee, W. K. Seah, H. Tan, and Z. Yao, "Wireless sensing without sensors – an experimental approach," in *PIMRC-09*, Sept. 2009.
- [21] M. Seifeldin and M. Youssef, "Nuzzer: A large-scale device-free passive localization system for wireless environments," tech. rep., 2009.
- [22] F. Viani, L. Lizzi, P. Rocca, M. Benedetti, M. Donelli, and A. Massa, "Object tracking through RSSI measurements in wireless sensor networks," *IEEE Electronics Letters*, vol. 44, no. 10, pp. 653–654, 2008.
- [23] P. Bahl and V. N. Padmanabhan, "RADAR: an in-building RF-based user location and tracking system," in *IEEE INFOCOM 2000*, vol. 2, pp. 775–784, 2000.
- [24] N. Patwari, A. O. Hero III, M. Perkins, N. Correal, and R. J. O'Dea, "Relative location estimation in wireless sensor networks," *IEEE Trans. Signal Process.*, vol. 51, pp. 2137–2148, Aug. 2003.
- [25] H. Hashemi, "The indoor radio propagation channel," *Proc. IEEE*, vol. 81, pp. 943–968, July 1993.
- [26] C. Chang and A. Sahai, "Object tracking in a 2D UWB sensor network," in *38th Asilomar Conference on Signals, Systems and Computers*, vol. 1, pp. 1252–1256, Nov. 2004.
- [27] A. Lin and H. Ling, "Three-dimensional tracking of humans using very low-complexity radar," *Electronics Letters*, vol. 42, pp. 1062–1063, 31 2006.

- [28] F. Sivrikaya and B. Yener, "Time synchronization in sensor networks: a survey," *IEEE Network*, vol. 18, pp. 45–50, July-Aug. 2004.
- [29] M. Maroti, B. Kusy, G. Balogh, P. Volgyesi, K. Molnar, A. Nadas, S. Dora, and A. Ledeczi, "Radio interferometric positioning," Nov. 2005.
- [30] Q. Yao, H. Gao, B. Liu, and F. Wang, "MODEL: moving object detection and localization in wireless networks based on small-scale fading," in *ACM SenSys'08*, pp. 451–452, 2008.
- [31] N. Patwari and J. Wilson, "People-sensing spatial characteristics of RF sensor networks," tech. rep., University of Utah SPAN Lab, October 2009. ArXiv:0911.1972v1.
- [32] M. Skolnik, *Introduction to Radar Systems*. McGraw Hill Book Co., 1980.
- [33] A. C. Kak and M. Slaney, *Principles of Computerized Tomographic Imaging*. The Institute of Electrical and Electronics Engineers, Inc., 1988.
- [34] A. Hunt, C. Tillery, and N. Wild, "Through-the-wall surveillance technologies," *Corrections Today*, vol. 63, July 2001.
- [35] D. Estrin, R. Govindan, and J. Heidemann, "Embedding the Internet," *Communications of the ACM*, vol. 43, pp. 38–41, May 2000.
- [36] "Time Domain Corporation." <http://www.timedomain.com>.
- [37] "Cambridge consultants." <http://www.cambridgeconsultants.com>.
- [38] "Camero Tech." <http://camero-tech.com>.
- [39] A. R. Hunt, "Image formation through walls using a distributed radar sensor network," in *SPIE Conference on Sensors, and Command, Control, Communications, and Intelligence (C3I) Technologies for Homeland Security and Homeland Defense IV*, vol. 5778, pp. 169–174, May 2005.
- [40] S. L. Coetzee, C. J. Baker, and H. Griffiths, "Narrow band high resolution radar imaging," in *IEEE Conf. on Radar*, pp. 24–27, April 2006.
- [41] H. Griffiths and C. Baker, "Radar imaging for combating terrorism," *NATO Advanced Study Institute*, <http://www.nato-us.org/imaging2006/lecturers.html> (Springer, 2006).
- [42] M. C. Wicks, B. Himed, L. J. E. Bracken, H. Bascom, and J. Clancy, "Ultra narrow band adaptive tomographic radar," in *1st IEEE Intl. Workshop Computational Advances in Multi-Sensor Adaptive Processing*, Dec. 2005.
- [43] M. C. Wicks, "RF tomography with application to ground penetrating radar," in *41st Asilomar Conference on Signals, Systems and Computers*, pp. 2017–2022, Nov. 2007.
- [44] A. M. Haimovich, R. S. Blum, and L. J. C. Jr., "MIMO radar with widely separated antennas," *IEEE Signal Processing Magazine*, pp. 116–129, January 2008.

- [45] N. Patwari and P. Agrawal, "Effects of correlated shadowing: Connectivity, localization, and RF tomography," in *IEEE/ACM Int'l Conference on Information Processing in Sensor Networks (IPSN'08)*, April 2008.
- [46] P. Agrawal and N. Patwari, "Correlated link shadow fading in multi-hop wireless networks," *IEEE Transactions on Wireless Communications*, vol. 8, 2009.
- [47] R. J. Bultitude, "Measurement, characterization, and modeling of indoor 800/900 mhz radio channels for digital communications," *IEEE Communications Magazine*, vol. 25, June 1987.
- [48] R. Ganesh and K. Pahlavan, "Effects of traffic and local movements on multipath characteristics of an indoor radio channel," *IEE Electronics Letters*, vol. 26, no. 12, pp. 810–812, 1990.
- [49] J. Roberts and J. Abeyasinghe, "A two-state Rician model for predicting indoor wireless communication performance," in *Communications, 1995. ICC '95 Seattle, 'Gateway to Globalization', 1995 IEEE International Conference on*, vol. 1, pp. 40–43 vol.1, 1995.
- [50] A. P. Dempster, N. M. Laird, and D. B. Rubin, "Maximum likelihood from incomplete data via the EM algorithm," *Journal of the Royal Statistical Society*, vol. Series B (Methodological) 39, no. 1, pp. 1–38, 1977.
- [51] H. L. Van Trees, *Detection, Estimation, and Modulation Theory*. John Wiley and Sons, 1968.
- [52] A. Swami and B. M. Sadler, "On some detection and estimation problems in heavy-tailed noise," *Signal Process.*, vol. 82, no. 12, pp. 1829–1846, 2002.
- [53] B. Ripley and W. InterScience, *Spatial Statistics*. Wiley New York, 1981.
- [54] C. R. Vogel, *Computational Methods for Inverse Problems*. SIAM, 2002.
- [55] G. Demoment, "Image reconstruction and restoration: Overview of common estimation structures and problems," *IEEE Transactions on Acoustics Speech and Signal Processing*, vol. 37, December 1989.
- [56] J. Wilson and N. Patwari, "Radio tomographic imaging with wireless networks," tech. rep., University of Utah, Sensing and Processing Across Networks Lab, 2008.
- [57] J. Nocedal and S. Wright, *Numerical Optimization*. Springer, 1999.
- [58] A. Dey and G. Abowd, "Towards a better understanding of context and context-awareness," in *CHI 2000 Workshop on the What, Who, Where, When, and How of Context-Awareness*, pp. 304–307, 2000.
- [59] R. Want, A. Hopper, and V. Gibbons, "The active badge location system," *ACM Transactions on Information Systems*, vol. 10, no. 1, pp. 91–102, 1992.

- [60] T. Pratt, S. Nguyen, and B. Walkenhorst, "Dual-polarized architectures for sensing with wireless communications signals," in *IEEE Military Communications Conference, 2008. MILCOM 2008*, pp. 1–6, 2008.
- [61] F. Aryanfar and K. Sarabandi, "Through wall imaging at microwave frequencies using space-time focusing," in *IEEE Antennas and Propagation Society International Symposium (APS'04)*, vol. 3, pp. 3063–3066, June 2004.
- [62] A. Lin and H. Ling, "Through-wall measurements of a Doppler and direction-of-arrival (DDOA) radar for tracking indoor movers," in *IEEE Antennas and Propagation Society International Symposium (APS'05)*, vol. 3B, pp. 322–325, July 2005.
- [63] M. Lin, Z. Zhongzhao, and T. Xuezhi, "A novel through-wall imaging method using ultra wideband pulse system," in *IEEE Intl. Conf. Intelligent Information Hiding and Multimedia Signal Processing*, pp. 147–150, June 2006.
- [64] L.-P. Song, C. Yu, and Q. H. Liu, "Through-wall imaging (TWI) by radar: 2-D tomographic results and analyses," *IEEE Transactions on Geoscience and Remote Sensing*, vol. 43, pp. 2793–2798, Dec. 2005.
- [65] A. Vertiy, S. Gavrilov, V. Stepanyuk, and I. Voynovskyy, "Through-wall and wall microwave tomography imaging," in *IEEE Antennas and Propagation Society International Symposium (APS'04)*, vol. 3, pp. 3087–3090, June 2004.
- [66] E. Fishler, A. Haimovich, R. Blum, L. Ciminio, D. Chizhik, and R. Valenzuela, "Spatial diversity in radars - models and detection performance," *IEEE Trans. Signal Processing*, vol. 54, pp. 823–838, Mar. 2006.
- [67] G. D. Durgin, T. S. Rappaport, and D. A. de Wolf, "New analytical models and probability density functions for fading in wireless communications," *IEEE Trans. Communications*, vol. 50, pp. 1005–1015, June 2002.
- [68] D. Tse and P. Viswanath, *Fundamentals of Wireless Communication*. Cambridge Press, 2005.
- [69] S. Haykin and M. Moher, *Modern Wireless Communications*. Pearson Prentice Hall, 2005.
- [70] P. S. Maybeck, *Stochastic Models, Estimation, and Control*. Academic Press, 1979.
- [71] G. Welch and G. Bishop, "An introduction to the kalman filter," *University of North Carolina at Chapel Hill, Chapel Hill, NC*, 1995.
- [72] P. Hande, J. Smith, and D. Reed, "An analysis of fading mechanisms for fixed antennas," in *IEEE Vehicular Technology Conference*, 2000.
- [73] T. S. Rappaport, *Wireless Communications Principles and Practice*. Prentice Hall, 2002.
- [74] B. Ristic, S. Arulampalam, and N. Gordon, *Beyond the Kalman Filter: Particle Filters for Tracking Applications*. Artech House, 2004.

- [75] M. K. Pitt and N. Shepard, “Filtering via simulation: Auxiliary particle filters,” *Journal of the American Statistical Association*, pp. 590–599, 1999.
- [76] R. van der Merwe, A. Doucet, N. de Freitas, and E. Wan, “The unscented particle filter,” tech. rep., Cambridge University Engineering Department, 2000.
- [77] S. Sarkka, A. Vehtari, and J. Lampinen, “Rao-blackwellized particle filter for multiple target tracking,” *Information Fusion*, vol. 8, no. 1, pp. 2–15, 2007.
- [78] C. Robert and G. Casella, *Monte Carlo Statistical Methods*. Springer, 2004.